

**Control for Robot-assisted Image-guided Beating-Heart Surgery**

by

Meaghan Bowthorpe

A thesis submitted in partial fulfillment of the requirements for the degree of

Doctor of Philosophy

in

Biomedical Engineering

Department of Electrical and Computer Engineering

University of Alberta

©Meaghan Bowthorpe, 2015

# *Abstract*

Cardiovascular disease causes the greatest number of deaths worldwide each year according to the World Health Organization [1]. Hence, many patients require cardiovascular surgery each year. Short of stopping the motion of the heart at the beginning of a cardiac procedure, the surgeon would require superhuman ability to both follow the heart's beating motion and perform surgical maneuvers on the exterior surface of the heart. Performing a surgical procedure within the interior of a beating heart would be even more difficult due to the opaque blood pool that makes it difficult to visualize the heart tissue. Currently, to overcome the aforementioned obstacles, surgeons operate on either a mechanically stabilized or arrested heart, where a heart-lung machine ventilates the lungs and circulates the blood. A mechanical heart stabilizer can only minimize motion in a localized area on the exterior surface of the heart; it cannot completely stop the motion. Arresting the heart can lead to long-term cognitive loss [2], an increase in the risk of stroke [3], and complications when the heart is restarted.

Alternatively, a robot-held surgical tool can be controlled to follow the motion of a point of interest (POI) on the heart, allowing the heart to beat freely throughout the procedure. This would reduce the risks currently involved in mechanically stabilized and arrested heart surgery. In this scenario, the surgeon's hand motion is superimposed on the synchronizing movement of the robot. In this way, with a stabilized view of the heart, the point of interest on the heart appears stationary to the surgeon with respect to the surgical tool's tip. Allowing the heart to beat freely during the procedure means that the surgeon will be able to immediately evaluate the success of reconstructive operations and make adjustments as required. In contrast, using the current practice of arresting the heart at the outset of surgery, the outcome of the procedure is not known until after restarting the heart, and the surgeon would have to once again connect the patient to a heart-lung machine should additional operations be required.

This thesis presents the development of an experimental robot-assisted beating-heart surgical setup for procedures performed on either the exterior surface or interior of the heart. As the system must be able to visualize through the heart's blood pool in order for procedures to be performed inside the heart, ultrasound-guidance is considered. The challenge with using ultrasound images to locate the point of interest on the heart is that the position data is slowly sampled and delayed due to the time required to acquire and process each image. Therefore, in order for the surgical robot to provide good tracking, the motion of the point of interest on the heart measured from the ultrasound images must be upsampled and predicted ahead to the current time. This thesis presents different upsampling and prediction methods as well as different control structures for this purpose. The image processing required to locate the surgical tool and the point of interest on the heart tissue in ultrasound images is also discussed. The controllers have been validated experimentally and user trials were performed to determine whether such a system would, in fact, help surgeons.

# Preface

A summary of the literature is presented in Chapter 2. A more in depth discussion of the challenges involved in developing such a system is presented in Chapter 3. Portions of Chapters 2 and 3 were published in: “Meaghan Bowthorpe and Mahdi Tavakoli. Advances towards beating heart surgery. In Frederick T. Hawthorne, editor, *Minimally Invasive Surgery: Evolution of Operative Techniques, Safety & Effectiveness and Long-term Clinical Outcomes*. Nova Science Publishers, 2014.” Portions of Chapter 3 have been published in “Meaghan Bowthorpe, Mahdi Tavakoli. Physiological Organ Motion Prediction and Compensation Based on Multi-rate, Delayed, and Unregistered Measurements in Robot-assisted Surgery and Therapy. *IEEE ASME Mechatronics*, Accepted September 2015. In press.”

In Chapter 4, a controller based on a Smith predictor is developed to compensate for the delay in acquiring and processing ultrasound image data. Portions of this chapter have been published in “Meaghan Bowthorpe, Mahdi Tavakoli, Harald Becher, and Robert Howe. Smith predictor-based robot control for ultrasound-guided teleoperated beating-heart surgery. *IEEE Journal of Biomedical and Health Informatics*, vol. 18, no. 1, pp.157-166, 2014.” and “Meaghan Bowthorpe, Mahdi Tavakoli, Harald Becher, and Robert Howe. Smith Predictor Based Control in Teleoperated Image-guided Beating-Heart Surgery. *IEEE International Conference on Robotics and Automation*, Karlsruhe, Germany, pp. 5825-5830, 2013.” Dr. Becher provided guidance with respect to the medical applications of this work. Dr. Tavakoli and Dr. Howe were the supervisory authors and aided with the conceptual development and manuscript composition. I was responsible for collecting the data, implementing the controller, and writing the manuscript.

The Smith predictor design is improved in Chapter 5 and a more thorough description of the experimental setup is included. Portions of this chapter have been published in “Meaghan Bowthorpe, Vincent Castonguay-Siu, and Mahdi Tavakoli. Development of a Robotic System to Enable Beating-heart Surgery, *Journal of the Robotics Society of Japan*, invited paper, vol. 32, no. 4, pp. 339-346, 2014.” Vincent Castonguay-Sui designed the mechanical cam used to generate the heart’s simulated motion in the experimental setup. Dr. Tavakoli was the supervisory author. I implemented the rest of the experimental setup, collected and analysed the data, and wrote the manuscript.

Next, the motion data collection methods are examined more closely in Chapter 6. Portions of this chapter have been published in “Meaghan Bowthorpe and Mahdi Tavakoli. Physiological Organ Motion Prediction and Compensation Based on Multi-rate, Delayed, and Unregistered Measurements in Robot-assisted Surgery and Therapy. *IEEE ASME Mechatronics*, Accepted September 2015. In press.” Dr. Tavakoli was the supervisory author. I developed the experimental setup, collected and analysed the data, and wrote the manuscript.

The experimental setup is now tested under ultrasound-guidance in Chapter 7. Ethics approval was required for this study entitled “Measuring User Performance in Controlling a Robot Through a User Interface” (#Pro00055825) as participants were asked to interact with the experimental setup to test how effective it was. Portions of this chapter have been submitted to the Journal of Medical Robotics Research as “Meaghan Bowthorpe and Mahdi Tavakoli. Ultrasound-based Image Guidance and Motion Compensating Control for Robot-assisted Beating-heart Surgery.” Dr. Tavakoli is the supervisory author. I developed the experimental setup and the image processing code, supervised the user study, collected the data and analyzed the results, and wrote the manuscript.

Generalized predictive control is presented in Chapter 8. Portions of this chapter have been published in “Meaghan Bowthorpe, Abril Álvarez García, and Mahdi Tavakoli. GPC-based Teleoperation for Delay Compensation and Disturbance Rejection in Image-guided Beating-heart Surgery, *IEEE International Conference on Robotics and Automation*, pp. 4875-4880, 2014.” Abril Álvarez García built the electronic analog controller required by the voice coil motor and implemented the code to run the Micron Tracker, which measures the position of the surgical tool and simulated heart. Dr. Tavakoli was the supervisory author. I developed the rest of the experimental setup, collected and analysed the data, and wrote the manuscript.

Generalized predictive control is further improved in Chapter 9. The experimental setup is tested under ultrasound-guidance and a user study determines the effectiveness of the system. Ethics approval for this study entitled “Measuring User Performance in Controlling a Robot Through a User Interface” (#Pro00055825) was required as participants were asked to interact with the experimental setup. Portions of this chapter have been submitted to *IEEE Robotics and Automation Letters* as “Meaghan Bowthorpe

and Mahdi Tavakoli. Generalized Predictive Control of a Surgical Robot for Beating-heart Surgery under Delay and Slowly-sampled Ultrasound Image Data.” I reconfigured the existing experimental setup and software to run these experiments. I also supervised the user study, analysed the data and wrote the manuscript. Dr. Tavakoli was the supervisory author.

## *Acknowledgements*

I would like to begin by expressing my sincere gratitude to my supervisor, Dr. Mahdi Tavakoli for his informative discussions, support, and enthusiasm. His tireless guidance has made this research project and dissertation possible.

I would also like to thank Dr. Becher, who provided advice on the clinical aspects of this thesis. He also provided ultrasound data that allowed me to create realistic experiments. I would also like to acknowledge Allen He and Peter Wood who helped me collect the ultrasound data.

I would also like to acknowledge Dr. Robert Howe, who supervised me for six months during a research visit to his lab. His guidance helped to give me a different perspective on this topic. I would also like to thank the members of the Harvard Biorobotics Lab who helped me with the experimental setup and provided fruitful discussions.

I would also like to thank Abril Álvarez García, Vincent Castonguay-Sui, Samuel Alves de Moura, and Lucia Gan for their help in improving the experimental setup. I would also like to thank the members of the Telerobotic and Biorobotics Lab for their helpful discussions and friendship.

I would also like to thank my family and friends who have supported and encouraged me while I completed this research project.

I would like to acknowledge the financial support provided by an NSERC CGS-M, a Provost Doctoral Entrance Award, an Alberta Innovates Tech Futures Award, a Walter H Johns Graduate Fellowship, a Michael Smith Foreign Study Supplement, and Queen Elizabeth II Graduate Student Scholarships.

Finally, I would like to extend a special thank you to my supervisory committee, Dr. Harald Becher and Dr. Tongwen Chen, and to my examination committee, Dr. Cenk Çavuşoğlu, and Dr. Roger Zemp.

# Contents

<b>Abstract</b>	<b>ii</b>
<b>Preface</b>	<b>iv</b>
<b>Acknowledgements</b>	<b>vii</b>
<b>Contents</b>	<b>viii</b>
<b>List of Figures</b>	<b>xi</b>
<b>List of Tables</b>	<b>xiv</b>
<b>Abbreviations</b>	<b>xv</b>
<b>Symbols</b>	<b>xvi</b>
<b>1 Thesis Synopsis and Organization</b>	<b>1</b>
1.1 Thesis Organization . . . . .	2
<b>2 Introduction</b>	<b>5</b>
2.1 Surgical System Configurations . . . . .	6
2.1.1 Hand-held Surgical Tools . . . . .	8
2.1.2 Teleoperated Surgical Tools . . . . .	9
2.1.3 Catheter-based Surgical Tools . . . . .	10
2.2 Heart Motion Measurement Methods . . . . .	11
2.2.1 Image-based Motion Tracking Methods . . . . .	12
2.2.1.1 Camera-based Methods . . . . .	12
2.2.1.2 Medical Scanner-based Methods . . . . .	13
2.2.2 Non-image-based Motion Tracking Methods . . . . .	14
2.3 Concluding Remarks . . . . .	15

<b>3</b>	<b>Problem Formulation</b>	<b>17</b>
3.1	Image Guidance . . . . .	18
3.1.1	Pericardiocentesis . . . . .	18
3.1.2	Mitral Valve Annuloplasty . . . . .	18
3.1.3	Heart Motion Measurement from Images . . . . .	20
3.2	Control Methods . . . . .	21
3.2.1	Prediction-based Controllers . . . . .	23
3.2.2	Predictive Feedback Controllers . . . . .	24
<b>4</b>	<b>Smith Predictor-based Delay Compensation</b>	<b>26</b>
4.1	Problem Formulation . . . . .	27
4.2	Preliminaries: Smith Predictor . . . . .	29
4.3	Proposed Smith Predictor Based Design . . . . .	31
4.3.1	Controller Design in the Absence of Delay . . . . .	31
4.3.2	Smith Predictor Design . . . . .	33
4.3.3	POI Motion Upsampling . . . . .	34
4.3.4	POI Motion Prediction . . . . .	35
4.4	Simulation Results . . . . .	38
4.5	Experimental Results . . . . .	41
4.6	Concluding Remarks . . . . .	47
<b>5</b>	<b>Development of a Robot-assisted Beating-heart Surgical Testbed with Smith Predictor-based Delay Compensation</b>	<b>48</b>
5.1	Experimental Testbed Design . . . . .	49
5.1.1	Surgical Robot Structure . . . . .	50
5.1.2	Simulated Heart Structure . . . . .	52
5.2	Feedback Control of Surgical Tool . . . . .	53
5.2.1	POI Motion Upsampling . . . . .	54
5.2.2	POI Motion Prediction . . . . .	55
5.2.3	Predictive Feedback Control . . . . .	56
5.3	Experimental Results . . . . .	59
5.4	Concluding Remarks . . . . .	62
<b>6</b>	<b>A Comparison of Proportional and Smith Predictor-based Control for Registered and Unregistered Measurements</b>	<b>63</b>
6.1	Sources of Physiological Motion . . . . .	65
6.2	Robot-assisted Compensation for Physiological Motion . . . . .	66
6.3	Control Systems . . . . .	68
6.3.1	POI Motion Upsampling . . . . .	69
6.3.2	POI Motion Prediction . . . . .	73
6.3.3	Robot Predictive Feedback Control . . . . .	74
6.3.3.1	Approach 1 . . . . .	75

6.3.3.2	Approach 2 . . . . .	76
6.4	Experimental Results . . . . .	79
6.4.1	Approach 1 . . . . .	82
6.4.2	Approach 2 . . . . .	82
6.5	Functional Task . . . . .	88
6.6	Discussion . . . . .	91
6.7	Concluding Remarks . . . . .	92
<b>7</b>	<b>Ultrasound-based Image Guidance and Motion Compensating Control</b>	<b>93</b>
7.1	System Development . . . . .	94
7.1.1	Ultrasound Imaging . . . . .	95
7.1.2	POI Motion Upsampling . . . . .	99
7.1.3	POI Motion Prediction . . . . .	100
7.1.4	Predictive Feedback Control of the Surgical Robot . . . . .	103
7.2	Experimental Setup . . . . .	104
7.3	Surgical Task . . . . .	104
7.4	Concluding Remarks . . . . .	111
<b>8</b>	<b>Generalized Predictive Control for Delay Compensation and Disturbance Rejection</b>	<b>113</b>
8.1	Generalized Predictive Control-based Motion Compensation . . . . .	114
8.1.1	Surgical Robot Control Algorithm . . . . .	118
8.2	Experimental Results . . . . .	119
8.3	Concluding Remarks . . . . .	125
<b>9</b>	<b>Ultrasound-guided Generalized Predictive Control</b>	<b>126</b>
9.1	Surgical Robot Control System . . . . .	127
9.2	Generalized Prediction Control . . . . .	128
9.3	Surgical Robot Control Algorithm . . . . .	131
9.3.1	POI Motion Measurement . . . . .	132
9.3.2	POI Motion Upsampling . . . . .	134
9.3.3	POI Motion Prediction . . . . .	135
9.4	Experimental Results . . . . .	137
9.5	Surgical Task . . . . .	138
9.6	Concluding Remarks . . . . .	144
<b>10</b>	<b>Conclusions and Future Work</b>	<b>145</b>
10.1	Future Work . . . . .	148

# List of Figures

2.1	Two block diagrams of a robot-assisted beating-heart surgical system. . .	8
2.2	A prototype of a hand-held tool for robot-assisted beating-heart surgery. .	9
3.1	A diagram of pericardiocentesis. . . . .	19
3.2	A diagram of a mitral valve that does not close. . . . .	19
3.3	A diagram of the robot's and ultrasound image's frames of reference . . .	21
3.4	Motion tracking in the absence of delay compensation. . . . .	22
4.1	A diagram of the robot-assisted surgical setup. . . . .	28
4.2	The development of the Smith predictor. . . . .	30
4.3	The development of the proposed Smith predictor. . . . .	32
4.4	The simulation results. . . . .	39
4.5	The simulation results for the Smith predictor. . . . .	40
4.6	The experimental setup. . . . .	42
4.7	A 3D ultrasound image of the surgical tool and simulated heart tissue. . .	43
4.8	Motion compensation without a Smith predictor. . . . .	44
4.9	EKF heart motion estimation. . . . .	44
4.10	The error for different upsampling and estimation methods. . . . .	45
5.1	A close up view of the surgical tool. . . . .	50
5.2	The electro-mechanical characteristics of the analog controller. . . . .	51
5.3	The analog control loop circuit diagram. . . . .	52
5.4	A mechanical cam. . . . .	53
5.5	The mechanical oscillator. . . . .	53
5.6	An ultrasound image of the heart and a simulated surgical tool (needle). .	54
5.7	The motion and frequency spectrum of a heartbeat. . . . .	56
5.8	The development of a Smith predictor. . . . .	57
5.9	The final model of the Smith predictor. . . . .	58
5.10	The result when the Smith predictor is not present. . . . .	59
5.11	Zero-order-hold upsampling. . . . .	60
5.12	The result using a zero-order-hold. . . . .	60
5.13	Cubic interpolation upsampling. . . . .	61
5.14	The result using cubic interpolation. . . . .	61

6.1	Configuration of the ultrasound and robot frames of reference. . . . .	67
6.2	A simple feedback controller for teleoperated motion compensation. . . . .	75
6.3	Configuration of Smith predictor method I. . . . .	77
6.4	Configuration of Smith predictor method II. . . . .	78
6.5	The experimental setup. . . . .	80
6.6	The simulated heart motion. . . . .	81
6.7	Position error of proportional control when the image to robot frame transformation is known. . . . .	83
6.8	Position error of Smith predictor method I when the image to robot frame transformation is unknown. . . . .	85
6.9	Position error of Smith predictor method II when the image to robot frame transformation is unknown. . . . .	86
6.10	Position error of Smith predictor method II when the image to robot frame transformation is known. . . . .	87
6.11	The functional task without motion compensation. . . . .	89
6.12	The functional task with motion compensation. . . . .	89
6.13	The functional task with Smith predictor method II. . . . .	90
7.1	A flow chart of the image processing. . . . .	96
7.2	A Hough transform. . . . .	97
7.3	The image processing to find the surgical tool shaft and the POI. . . . .	98
7.4	A feedback controller for teleoperated motion compensation. . . . .	103
7.5	The experimental setup. . . . .	105
7.6	A successfully deployed staple. . . . .	105
7.7	An example of using too much force when deploying the staple. . . . .	106
7.8	The rate of successful deployment of the staple for each participant. . . . .	107
7.9	The rate of the use of excessive force for each participant. . . . .	107
7.10	The result when motion compensation is provided. . . . .	109
7.11	The result when motion compensation is not provided. . . . .	110
8.1	A GPC feedback control system. . . . .	115
8.2	A diagram of GPC method I. . . . .	119
8.3	A diagram of GPC method II. . . . .	119
8.4	The surgical tool. . . . .	121
8.5	The experimental setup. . . . .	122
8.6	The experimental result without the surgeon's motion. . . . .	122
8.7	The experimental result with a square wave as the surgeon's motion. . . . .	122
8.8	The result of a proportional controller. . . . .	123
8.9	The surgical tool following the heart's estimated motion. . . . .	124
8.10	The surgical tool following the heart's estimated motion and the surgeon's motion. . . . .	124
9.1	A model of the GPC controller. . . . .	131

*List of Figures*

---

9.2	A flow chart of the image processing. . . . .	133
9.3	The image processing to find the surgical tool shaft and the POI. . . . .	134
9.4	The experimental setup. . . . .	139
9.5	The deployment of a staple. . . . .	139
9.6	The rate of successful deployment of the staple for each participant. . . . .	141
9.7	The rate of the use of excessive force for each participant. . . . .	141
9.8	The result when motion compensation is provided. . . . .	142
9.9	The result when no motion compensation is provided. . . . .	143

# List of Tables

3.1	A summary of the literature. . . . .	25
4.1	The command following errors. . . . .	40
4.2	A summary of the simulation results. . . . .	41
4.3	A summary of the experimental results. . . . .	44
5.1	A summary of the experimental results. . . . .	62
6.1	The possible upsampling and prediction methods for each approach. . . . .	79
6.2	A summary of the experimental results. . . . .	87
7.1	A summary of the experimental results. . . . .	111
8.1	A summary of the experimental results. . . . .	124
9.1	A summary of the experimental results. . . . .	144

# Abbreviations

CABG	Coronary Artery Bypass Graft
CI	Cubic Interpolation
DOF	Degrees of Freedom
EKF	Extended Kalman Filter
GPC	Generalized Predictive Control
PID	Proportional Integral Derivative Control
PI	Proportional Integral Control
POI	Point of Interest
ROI	Region of Interest
SP	Smith Predictor
ZOH	Zero Order Hold

# Symbols

$\bar{C}$	A controller in a time delayed system
$C$	A controller in a system without a time delay
$D_{RH}$	Distance between the robot and the heart tissue in the frequency domain
$d_{RH}$	Distance between the robot and the heart tissue in the time domain
$e$	Command following error ( $p_S - d_{RH}$ )
$G$	The plant, i.e. the robot
$\bar{H}$	A transfer function of a time delayed system
$H$	A transfer function of a system without a time-delay
$\hat{P}_H$	Estimated position of the heart in the frequency domain
$\hat{p}_H$	Estimated position of the heart in the time domain
$P_H$	Position of the heart in the frequency domain
$p_H$	Position of the heart in the time domain
$P_O$	Position of the organ in the frequency domain
$P_R$	Robot position
$P_S$	Position of the surgeon in the frequency domain
$p_S$	Position of the surgeon in the time domain
$R$	Input signal to a control system
${}^R_I T$	Image to robot frame transformation
$Y$	Output signal of a control system
$X$	Continuous-time signal
$\hat{X}$	Predicted $X''$ from $\bar{X}''$ (a discrete-time signal)

## *Symbols*

---

$X'$	Slowly-sampled discrete signal
$X''$	Fast-sampled discrete signal
$\bar{X}'$	Delayed and slowly-sampled discrete signal
$\bar{X}''$	Delayed and fast-sampled discrete signal
${}^I X$	A point in the image frame
${}^R X$	A point in the robot frame

# Chapter 1

## Thesis Synopsis and Organization

This thesis proposes different control algorithms to control a surgical robot to compensate for the motion of a point of interest (POI) that is moving due to physiological motion. Performing a surgical procedure on a beating heart or organ affected by respiratory motion is extremely difficult. However, a robot-held surgical tool can be controlled to follow the motion of a POI, allowing the heart to beat freely (or organ to move freely) throughout the procedure. In this scenario, the surgeon's hand motion is superimposed on this synchronizing movement of the robot. In this way, with a stabilized view of the heart, the heart appears stationary to the surgeon. Allowing the heart to beat freely during the procedure means that the surgeon will be able to immediately evaluate the success of reconstructive operations and make adjustments as required. In contrast, using the current practice of arresting the heart at the outset of surgery, the outcome of the procedure is not known until after restarting the heart, and the surgeon would have to once again connect the patient to a heart-lung machine should additional operations be required.

## 1.1 Thesis Organization

This thesis begins with an overview of the different designs proposed for a robot-assisted surgical system that will enable beating-heart surgery. As many different surgical procedures are performed on the heart, a variety of designs have been presented in the literature. Chapter 2 categorizes the different designs and the procedures for which they are intended.

Following the summary of designs, a more in-depth discussion of the challenges involved in developing such a system based on ultrasound image guidance and teleoperation is included in Chapter 3. These challenges include overcoming the time delays created by the image acquisition and processing, following the heart's fast motions, and upsampling the slowly-sampled position data collected from ultrasound images. If the time delays are not compensated for, the system may become unstable and the surgical tool may collide with the heart tissue. If the slowly-sampled data is not upsampled, the surgical robot's motion will not be smooth, making it more difficult for the surgeon to operate.

In Chapter 4, a controller based on a Smith predictor is developed to compensate for the delay in acquiring and processing ultrasound image data. As the heart motion data collected from ultrasound images is acquired at a slow rate, two upsampling methods are presented: zero-order-hold and cubic interpolation. To reduce the tracking error, an estimate of the heart's current motion is included in the controller's setpoint. Three estimation methods are presented: using the heart's motion from the previous beat, using an extended Kalman filter, and temporally aligning the motion of the past heart beat based on the current heart rate as estimated by the extended Kalman filter. This research was performed at the Harvard Biorobotics Lab in collaboration with Dr. Howe. For this reason, ultrasound imaging was included in this chapter.

The Smith predictor design is improved in Chapter 5. Here, the estimated heart motion is added inside the feedback loop to cancel the disturbance caused by the beating heart; whereas, in the previous chapter it was added to the setpoint. An experimental testbed

was created to test the motion compensating control algorithms. This experimental testbed is described in detail in this chapter. As ultrasound imaging was not available for these experiments, a Micron Tracker simulated the ultrasound scanner.

Next, the motion data collection methods for beating-heart surgery and radiation therapy are examined more closely in Chapter 6. In the operating room, it may be difficult to continually track the ultrasound probe's position as the tracker's view may be occluded by the surgical staff or it may be too computationally expensive to continually calculate the transform between the imaging frame and the surgical robot's frame if the ultrasound probe is not held stationary. In this chapter, the two previous Smith predictor configurations are compared with PID control. If the image to robot transformation is available, simple PID control can be used with extended Kalman filter-based or cubic interpolation-based upsampling and extended Kalman filter-based or last cycle-based prediction. If the transformation is not available, a Smith predictor can be used with cubic interpolation-based upsampling and extended Kalman filter-based or last cycle-based prediction. A Micron Tracker simulated an ultrasound scanner for these experiments.

The experimental setup is now tested under ultrasound-guidance in Chapter 7. The image processing required to locate the surgical tool tip and the point of interest on the heart tissue is described. All of the previous experiments in this thesis included predetermined motion for the surgeon. Here, the surgeon's motion is determined by the user. In this chapter, a study is performed where participants are asked to deploy a staple into phantom heart tissue with and without motion compensation to determine whether motion compensation is in fact helpful. To deploy the staple successfully, the surgical tool tip must come into contact with the POI. As a proportional controller is shown to perform better than a Smith predictor in the previous chapter, proportional control is used in this chapter.

PID controllers and Smith predictors only correct for the current error in the feedback loop. However, if the model of the surgical tool and the future setpoints are known, a set

of optimal control signals that minimize future errors in addition to the current error can be calculated. Generalized predictive control takes advantage of this knowledge of the future motion and calculates the optimal control value over a future time horizon. This controller is presented in Chapter 8. Two configurations of this controller are presented. The first considers the heart's motion as a disturbance and makes the distance between the surgical tool tip and the point of interest follow the surgeon's motion. The second estimates the heart's motion and makes the surgical tool tip follow the combination of the heart's and surgeon's motion.

The generalized predictive control scheme is improved in Chapter 9. The sampling rate is increased from 20 Hz to 100 Hz and the motion of the point of interest on the heart is measured from ultrasound images. A user study similar to that of Chapter 7 is performed. However, the participants were told to deploy the staple in the lower half of the POI's motion. This no longer allowed the user to simply wait for the POI to come to the surgical tool and deploy the staple successfully without motion compensation as was previously possible.

Finally, conclusions and future work are presented in Chapter 10.

## Chapter 2

# Introduction

Cardiovascular disease is one of the leading causes of death worldwide [1]. Any advancements that make the surgical procedure safer for patients and shorten the recovery time have the potential to greatly benefit society. The advent of minimally invasive surgery has reduced the amount of trauma a patient undergoes when a surgical procedure is performed. However, current intervention practices for heart surgery have serious side effects. Currently, surgeons have two options when operating on a heart. The first is to mechanically stabilize the heart using a mechanical stabilizer that either applies pressure or suction to stabilize a small localized area on the surface of the heart. This device can only be used on areas of the surface of the heart. Also, this method cannot keep the localized area completely still; there will inevitably be some residual motion [5]. The second is to arrest the heart and connect the patient to a heart-lung bypass machine, which circulates the blood and ventilates the lungs. After the procedure, the heart is massaged and restarted. However, complications such as irregular heartbeats

---

Portions of this chapter have been published in “Meaghan Bowthorpe and Mahdi Tavakoli. Advances towards beating heart surgery. In Frederick T. Hawthorne, editor, *Minimally Invasive Surgery: Evolution of Operative Techniques, Safety & Effectiveness and Long-term Clinical Outcomes*. Nova Science Publishers, 2014.” [4]

may occur. As well, the patient is at an increased risk of having a stroke [3] and may suffer from long-term cognitive loss [2].

These risks could be removed if a surgeon could operate on a freely beating heart. However, due to the heart’s fast motion – with velocities and accelerations up to 210 mm/s and 3800 mm/s<sup>2</sup>, respectively [6] – normal operation on the beating heart is extremely difficult for a surgeon as it would require superhuman skill to follow the heart’s motion and simultaneously perform a surgical procedure. Letting the heart beat freely during the procedure would be feasible if the surgical robot and the surgical tool attached to it followed the heart’s beating motion. This would mean that there would be no relative motion between a point of interest (POI) on the heart and the tip of the surgical tool. Then, the surgeon is given “remote” control over the surgical robot and a stabilized view of the heart. The surgeon’s motions are simply added to the surgical robot’s heart-tracking motions, allowing the surgeon to operate on a seemingly stationary but actually beating heart.

Beating-heart surgery promises many benefits for surgeons and patients. It would eliminate the adverse side effects associated with mechanically stabilizing or arresting the heart. In addition, normal heart beating motion during the surgery would allow for intra-operative evaluation of the effectiveness of reconstructive procedures on dynamic heart structures (e.g., mitral valve repair), which is impossible when the heart is arrested.

## 2.1 Surgical System Configurations

The goal of a robot-assisted beating-heart surgical system is to enable a surgeon to operate on a beating heart. There are several ways to develop the surgical system as the chosen design depends on the intended surgical procedure. However, certain components are required in all cases. These include a robot that holds and moves the surgical tool, a sensor to measure the heart’s motion, a user interface that allows the surgeon to control the robot’s motion, and a controller to make the robot follow the summation of

the heart's motion and the surgeon's motion. Hence, relative to the heart, the surgical tool will follow the surgeon's motion. With this and a stabilized view of the heart, the surgeon will be able to operate on the beating heart.

In the literature, the two main configurations of the surgical system presented include a hand-held tool and a teleoperated tool. Block diagrams of the two different systems are shown in Figs. 2.1a and 2.1b [7, 8]. The first, Fig. 2.1a, is designed for a hand-held tool that is controlled to track the heart's motion. The second, Fig. 2.1b, is designed for a teleoperated system, where the surgeon's console is physically separated from the surgical robot, which is controlled to track the heart's motion *and* the surgeon's motion.

Even though the surgeon will interact differently with these two systems, they have many elements in common. The first is a method of capturing the heart's and the surgical tool's motion. This is the "Sensor" in Figs. 2.1a and 2.1b. Many different ways of measuring heart's motion and surgical tool's motion have been proposed in the literature, each with their own benefits and limitations. Section 2.2 includes a description of these methods. Once the heart's and the surgical tool's motion is known, a control system is developed that will take the heart's motions (and the surgeon's motions where applicable) into account and move the surgical robot accordingly. This is the "Robot Controller" in Fig. 2.1a and 2.1b. The various control methods that have been proposed are later discussed in Section 3.2.

The difference between these systems is in how the elements interact with each other. For example, note how the surgeon's hand motion is added in Fig. 2.1b and in Fig. 2.1a. The surgeon interacts with the surgical system through the surgeon's user interface. This may be the surgical tool itself in the case of a hand-held surgical tool or a physically separated console in the case of a teleoperated surgical tool or a catheter-based system. In both cases, the surgical tools are controlled to follow the heart's motion, but the inputs to the control system are different. The different surgical tools and their corresponding user interfaces are discussed below.

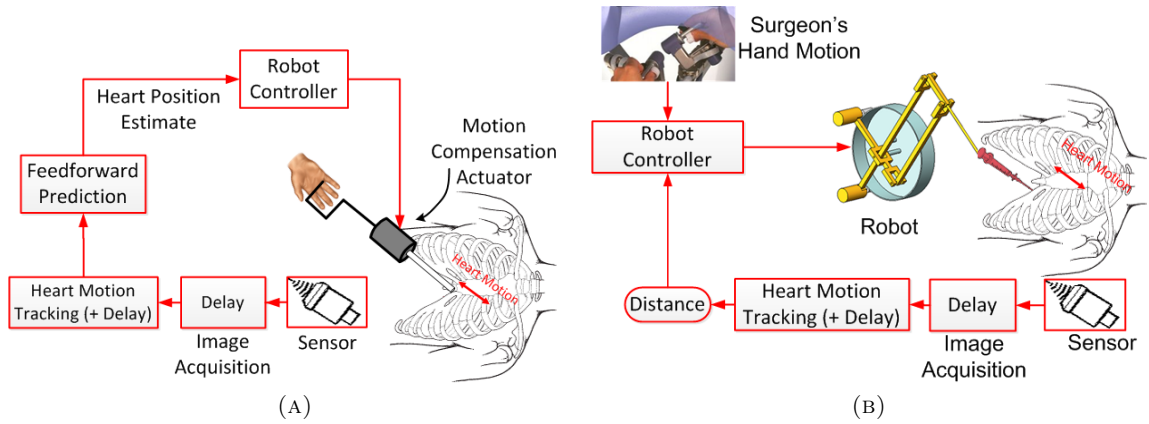


FIGURE 2.1: Two block diagrams of a robot-assisted beating-heart surgical system. (a) A system designed for a hand-held robot [7]. (b) A system designed for a teleoperated robot [8].

### 2.1.1 Hand-held Surgical Tools

Hand-held surgical tools are similar to laparoscopic tools where the surgeon holds the long rod-like tool in his or her hand [9]. Such tools can be modified for robot-assisted beating-heart surgery by attaching an actuator, which moves the surgical tool tip with respect to the surgical tool's handle. A hand-held surgical tool has been designed at the Harvard BioRobotics Lab [6]. A picture of the prototype is shown in Fig. 2.2 [10]. The surgeon is able to directly affect the distance between the tool tip and the heart because the surgical tool tip is moving in synchrony with the heart. The usefulness of such a tool was tested under multiple conditions resembling surgical tasks by multiple users. The users were asked to draw a circle between two concentric circles attached to a platform moving in the same manner as a point on the edge of the mitral valve leaflets. The first trial did not include motion compensation between the tool tip and the platform, while the second was under complete motion tracking and the remainder were under varying degrees of positional errors and motion asynchrony errors [6]. This study showed that the use of heart motion compensation greatly improved the users' ability to draw the circle.

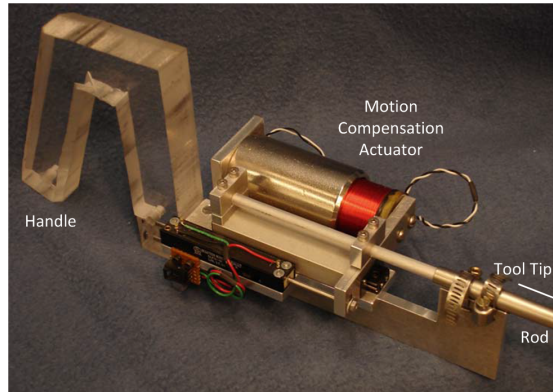


FIGURE 2.2: A prototype of a hand-held tool for robot-assisted beating-heart surgery [10].

This above tool has been designed for procedures that require heart motion compensation in one direction only. This is sufficient, e.g., for stapling an annuloplasty ring in place to reshape a mitral valve [6]. This surgical tool can only offer the limited dexterity that a regular laparoscopic tool has.

### 2.1.2 Teleoperated Surgical Tools

Another method is to use a teleoperated surgical tool where the surgical robot and the surgeon's console (user interface) are physically separated. The surgical tools can be similar to those used in laparoscopy except that they are held by a surgical robot. The surgeon loses physical contact with the surgical tools and hence, also may lose the sense of touch depending on the teleoperation configuration. In unilateral teleoperation, the focus of this work, the sense of touch is lost and the surgeon must rely on visual cues to determine the forces with which he or she is interacting with the tissue. In contrast, bilateral teleoperation, which is beyond the scope of this work, will transmit a sense of touch to the surgeon. Unlike a hand-held tool, the dynamics of the robot are now important.

There are many benefits associated with a teleoperated surgical tool. The first is that the surgeon can sit behind a console comfortably and does not need to attempt to

operate (as with hand-held tools) at an awkward position above the patient. Also, more dexterity is possible as a multi-degree of freedom wrist can be added to the tool tip in surgical teleoperation. This gives the surgeon improved dexterity that is not possible with current laparoscopic tools. In addition, teleoperation can also enhance the surgeon's capabilities as the surgeon's motions can be scaled and hand tremors can be reduced [11]. Teleoperation is also important for training new surgeons as the motion trajectories of experienced and inexperienced surgeons can be compared as they complete the same task [12]. Control of the surgical robot can also be split between multiple surgeons or between a control system and a surgeon if, for example, the surgical tool should not cross into a specific area. Teleoperated surgical tools are well suited for many procedures including annuloplasty [8] and coronary artery bypass graft (CABG) [13, 14]. Because of the many benefits associated with teleoperated surgical tools, this thesis will focus on designing a teleoperated robot-assisted beating-heart surgical system.

### **2.1.3 Catheter-based Surgical Tools**

Catheter-based surgical tools, long and thin flexible tools that reach the heart via the vascular system, offer a less invasive method of performing beating-heart surgery as compared to teleoperated and hand-held surgical tools. This is beneficial for patients, but the catheters are extremely difficult to steer and control at the fast rate required by beating-heart surgery. The target procedure for catheter-based surgical tools is ablation [15] or discriminating tissue stiffness [16]. Kesner et al. have found that moving the catheter within its sheath is difficult due to friction and backlash and appropriate compensation is required [17]. Loschak et al. have extended the work done by Kesner et al. in order to automatically move the catheter tip to a desired location in three-dimensional space [18]. Catheter-based surgical tools can be considered a special case of teleoperated surgical tools because the surgeon controls the catheter from a user interface. The main difference is that with teleoperated tools we must consider the inertial contributions due to the weight of the robot, whereas with catheter-based tools we must consider friction and backlash within the sheath.

## 2.2 Heart Motion Measurement Methods

The ability to track the location of the POI on the heart is essential for the development of the proposed robot-assisted beating-heart surgical system. One cannot control the surgical robot to follow the POI if its location is unknown. This is one of the greatest challenges in developing a beating-heart surgical system. Before the various motion-capture methods are described, it is important to understand how the heart moves. The heart's complete motion is caused by two different sources: the contraction and expansion of the heart muscle tissue as it beats and the motion of the lungs during respiration. The complete robot-assisted surgical system will need to track both types of motion. Respiratory motion is slow and can be made quite periodic when the patient is connected to a ventilator. This type of motion is much easier to track than the heart's beating motion, which can be three-dimensional and can have large accelerations, especially for dynamic tissue inside the heart.

Various types of sensors can be used to gather information about the POI's motion. For example, the heart's position may be measured by a force sensor, by sonomicrometry crystals, by high-frame-rate cameras, or by medical scanners. Force sensors are preferable for procedures where the surgical tool is constantly in contact with the POI, such as ablation [16, 19–23] or tissue palpation [15]. However, force sensors cannot measure the POI's position before the surgical tool makes contact. For this reason, force sensors are not considered in this thesis.

A discussion of the remaining tracking methods is facilitated by breaking them into two categories: image-based methods and non-image-based methods. There are advantages and disadvantages to each method as will be discussed later in greater detail. The image-based methods can be used only if the motion of the POI remains within the field of view of the image.

### **2.2.1 Image-based Motion Tracking Methods**

Images constitute an effective method to provide information about the heart's motion to the surgeon. Many different types of image-based tracking methods can be used to track the motion of the heart, e.g. high-speed cameras and medical scanners. All image-based tracking methods require a certain amount of time to acquire and process each image to find the location of the heart. This may or may not introduce a non-negligible time delay into the system. The image-based tracking methods will be further separated into two categories: camera-based methods and medical scanner-based methods.

#### **2.2.1.1 Camera-based Methods**

Camera-based methods provide colour images of the heart that are rich with detail. This aids in tracking a specific point on the heart. However, this method is limited to tracking points on the surface of the heart because cameras cannot visualize through the opaque blood pool. The advantage of camera-based methods is that these images often have better resolution, show more detail, and are obtained faster than medical scanner images such as ultrasound and MRI. In addition, if the camera is held motionless, both the respiratory-induced motion and the heart beat-induced motion of the heart are captured. The target surgical procedure that uses camera-based methods is a CABG.

High-speed video cameras are used by [13, 24, 25] – a 500 Hz camera in the case of [13, 24] and a 955 Hz monochrome camera in the case of [25] – to capture the heart's motion. Because the images are acquired quickly, neither method needs to consider the minimal image acquisition delay. The next step is to process the images in order to identify the location of the POI. Three markers on the simulated heart, an LED marking the surgical tool's tip, and a laser shining onto the simulated heart along the axis of the surgical tool allowed Ginhoux et al. to quickly identify the simulated heart's position with respect to the surgical tool tip [13, 24]. The image processing required to find these markers is described in [26]. Nakamura et al. do not place markers on the heart; instead, they identify a POI in an image and then track this same structure in subsequent images [25].

Others are trying to identify how the entire heart (and not simply the POI) moves in each image [27] and how to track it [28].

### **2.2.1.2 Medical Scanner-based Methods**

Ultrasound images are the most common medical images used for heart motion capture. These images are relatively inexpensive and simple to obtain. MRI images could be used; however, it is challenging to operate on the patient within the large magnetic field and the confines of the MRI scanner itself. Also, obtaining images from an MRI scanner in real-time is still very difficult. The advantage of using ultrasound images is that they can visualize the interior heart tissue through the opaque blood pool in real-time. However, ultrasound scanners still have low frame rates. For instance, the frame rate of a 3D ultrasound scanner can be as low as 18 Hz [29]. The location of the POI must then be found in each image frame, which can introduce a delay due to the processing that is involved. This time delay and the low image acquisition rate must be compensated for by the control system (Section 3.2). Otherwise, the teleoperated robot end-effector (i.e., the surgical tool) may collide with and puncture the fast-moving heart.

The hand-held tool discussed in Section 2.1.1 relies on data from ultrasound images in [30, 31]. The image processing method used to locate the POI on the heart and the surgical tool in each image frame is the “flashlight” approach described in [32] and used in [8]. This method identifies the surgical tool by finding the longest straight line in the image through the Radon Transform [32]. This line is then extended to the nearest bright point (the closest heart tissue). This is the location of the POI – the tissue directly in front of the surgical tool tip. This information is used by the controller to make the surgical tool follow the motion of the POI, as will be discussed in Section 3.2.

The catheter-based systems also use ultrasound images. However, instead of an external probe, a catheter mounted intracardiac echocardiography probe is used [18, 33]. Some preliminary work to create a larger field of view from the individual ultrasound images

has been performed in [33]. Later, these images will be used to track a POI on the interior surface of the heart.

The target procedures for medical scanner-based motion measurement methods are procedures performed inside the heart such as annuloplasty for mitral valve correction or ablation to treat arrhythmia. The image resolution is much worse than that of a camera-based system, and hence research about procedures performed on the exterior surface of the heart does not typically use ultrasound images. However, if the resolution of a medical scanner image is sufficient for a procedure performed on the surface of the heart, a medical scanner-based method could be used for this procedure.

### **2.2.2 Non-image-based Motion Tracking Methods**

Different groups have also proposed tracking methods that do not require images of the heart. Some of these methods are feasible for surgical procedures such as those that use force sensors [15, 20, 34] or a fiber optic probe [35], while others such as those using sonomicrometry crystals are not [14, 36–39].

One possible method is to use a force sensor [19]. The goal is to keep the contact force between the heart tissue and the surgical tool the same. The difficulty is that the rapid back and forth motion of the surgical tool creates vibrations at the tip. This can lead to instability and tracking errors. Nevertheless, if the vibrations can be controlled, this method is feasible for performing a surgical procedure such as tissue ablation, where the surgical tool can be in constant contact with the heart tissue. The main advantage of using a force sensor for motion tracking is that it would also give the surgeon a sense of touch, which is not currently available in most teleoperated robotic surgical systems.

Some researchers use sonomicrometry crystals to track the position of the heart [14, 36, 37, 40]. Sonomicrometry crystals are small piezoelectric crystals that transmit and receive ultrasound signals. In order to measure the motion of the POI on the heart, a base of six asymmetrically mounted crystals is set under the heart and another crystal

is sutured onto the POI [36]. The “time of flight” data is used to calculate the distances between the crystals. This is a complex calculation and is currently not done in real time. In this approach, both the heart’s beating motion and respiratory-induced motion can be measured [14]. Inserting the crystal base and suturing another crystal to the POI is not feasible for a surgical procedure. However, it does provide an excellent method for accurately measuring the heart’s position and the accuracy of other methods that are feasible for surgical procedures can be tested with respect to it. This method does suffer from noise caused by ultrasound echoes. Horiuchi et al. use various filters to increase the accuracy and reduce the effect of noise in this system [37]. Tuna et al. continued the work by Bebek et al. by modeling the heart’s motion as a weighted sum of previously collected heart motion data points [14].

### **2.3 Concluding Remarks**

A robot-assisted beating-heart surgical system has the potential to improve the outcome of many surgical procedures performed on the heart. There are different ways to design such a system as each surgical procedure has different requirements. For example, the procedure could be performed on the outside surface of the heart or within the heart, which would affect the choice of the required motion-capture module. This motion-capture system, in turn, affects the choice of a controller because there may or may not be a non-negligible time delay in acquiring the heart motion data. In addition, whether the surgeon prefers to use a teleoperated device or whether a hand-held device will suffice also affects the choice of the controller. Furthermore, the speed of the motion of the POI on the heart may mean that the robot control loop will need to have fast dynamics (large bandwidth of error tracking), again affecting the controller choice.

Once the requirements for a specific surgical procedure have been determined, the robot-assisted beating-heart surgical system can be designed. This will include a controller that can compensate for both the respiratory-induced motion and the heart beat-induced motion while still following the surgeon’s motion. A motion capture system is needed

to collect data about the heart's position and the surgical tool's position. Next, a user interface for the surgeon is required. Finally, a stabilized view of the target site on the heart must be given to the surgeon in order for him or her to operate.

## Chapter 3

# Problem Formulation

The side effects and limitations of arrested heart surgery and the use of mechanical stabilizers can be eliminated if the heart is allowed to beat freely during the surgical procedure. This would be feasible if a robot could follow the heart's beating motion, allowing the surgeon who is teleoperating the surgical robot, to operate on a seemingly stationary heart. In addition, normal heart beating motion during the surgery would allow for *intra-operative* evaluation of the effectiveness of reconstructive procedures on dynamic heart structures (e.g., mitral valve repair), which is impossible when the heart is arrested. The main components of such a system, the imaging method and the control method, will be discussed further in this chapter.

---

Portions of this chapter were published in “Meaghan Bowthorpe and Mahdi Tavakoli. Advances towards beating heart surgery. In Frederick T. Hawthorne, editor, *Minimally Invasive Surgery: Evolution of Operative Techniques, Safety & Effectiveness and Long-term Clinical Outcomes*. Nova Science Publishers, 2014.” and in “Meaghan Bowthorpe and Mahdi Tavakoli. Physiological Organ Motion Prediction and Compensation Based on Multi-rate, Delayed, and Unregistered Measurements in Robot-assisted Surgery and Therapy. *ASME Mechatronics*, Accepted September 2015, In press.”[4]

## 3.1 Image Guidance

In this work, ultrasound images were chosen as they can visualize both the interior and exterior surface of the heart. As specific examples, we describe pericardiocentesis and mitral valve annuloplasty as potential procedures that could benefit from a robot-assisted motion compensating surgical system.

### 3.1.1 Pericardiocentesis

Pericardiocentesis is a surgical procedure that is performed when there is a build-up of excess fluid in the pericardial sac. The extra fluid puts increased pressure on the heart and does not allow it to beat properly. The fluid is drained by inserting a needle through the chest wall and into the pericardial sac as shown in Fig. 3.1. Currently, the surgeon inserts the needle (while the heart is beating and the patient is conscious) with little to no intra-operative image guidance [41]. As a precaution and to limit the chest motion, the patient is instructed to hold his/her breath as the needle is inserted. However, if the needle punctures a coronary artery, immediate surgery may be required to stop the bleeding, making this emergency procedure highly stressful. To reduce the risks associated with this procedure, the general framework of beating-heart surgery using a heart motion-synchronized needle can be applied. This will allow the surgeon to insert the needle as if the heart wall is stationary, making the operation safer for the patient and less stressful for the surgeon.

### 3.1.2 Mitral Valve Annuloplasty

Mitral valve annuloplasty is a surgical procedure that is performed when the mitral valve does not close properly, thus a lower volume of blood is pumped during each heart beat due to regurgitation – see Fig. 3.2. To correct this, an annuloplasty ring is stapled around the mitral valve to reshape it. The ability to perform this procedure while the heart is beating would allow the surgeon to evaluate the function of the reshaped mitral

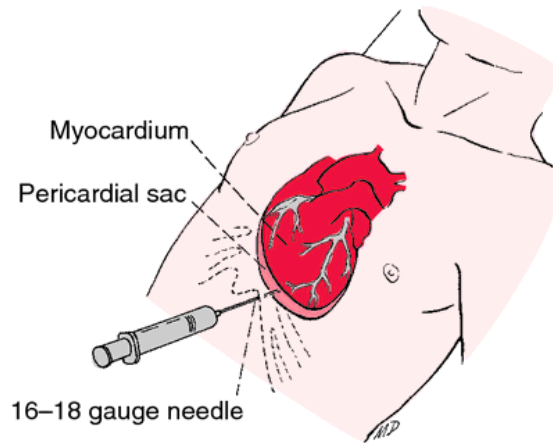


FIGURE 3.1: A diagram of pericardiocentesis. The needle is inserted through the chest wall and into the pericardial sac but should stop short of the heart tissue [42].

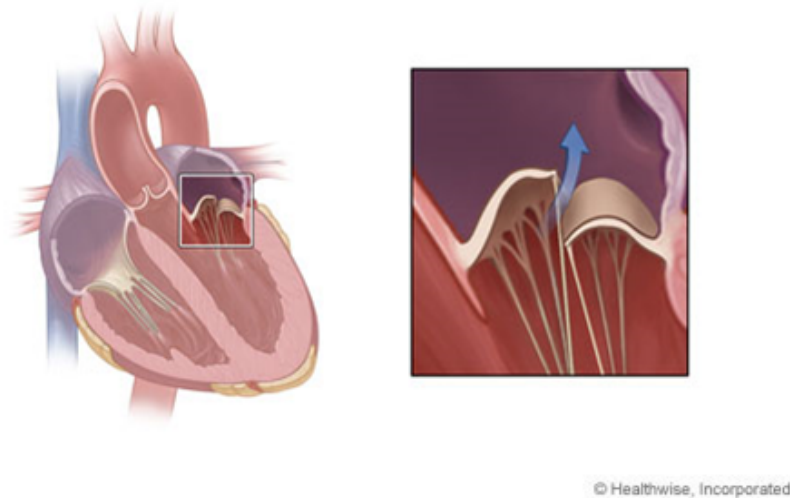


FIGURE 3.2: A diagram of a mitral valve that does not close, allowing the blood to flow backwards [43].

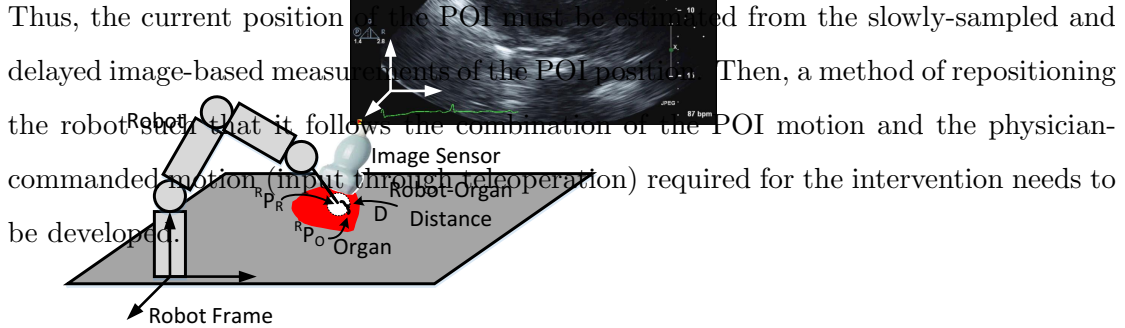
valve on the fly. The surgeon would then be able to readjust the shape of the mitral valve as necessary during the procedure. Currently, the result of the procedure is only known after the heart is restarted when it is too late to make adjustments. If a surgical tool could be made to follow the mitral valve's motion, which is mainly in one dimension [6], it would offer a better outcome of the procedure for the patient.

### 3.1.3 Heart Motion Measurement from Images

Obtaining the position and distance measurements from images creates three main challenges in designing the robot-assisted motion compensating system.

1. *Slowly sampled data from the image sensor*: The images, from which measurements about the motion of the target tissue on the organ are to be taken, can be acquired at a rate as low as 20 Hz from an ultrasound scanner. If the robot is controlled to follow these slowly sampled measurements of the position of the POI on the organ, its motion will not be smooth, which will not make performing the procedure much easier for the physician. Therefore, the slowly sampled position measurements must first be upsampled before being used in the robot's feedback control loop.
2. *Delay in data acquisition and processing from the image sensor*: To measure the target tissue's position, an appropriate image-based sensor such as ultrasound scanners, magnetic resonance imaging (MRI) scanners, CT scanners, or endoscopes is used. Depending on the utilized sensor, the data acquisition delay, which is dependent on the sampling rate, may be small as with high-speed endoscopes or large as with ultrasound scanners. Once the image is obtained, it must be processed to locate the position of the POI and robot within the image. This processing time varies between image sensors and adds to the acquisition delay. If the delayed position data concerning the POI motion is used in the feedback control loop without delay compensation, the robot control loop may become unstable, possibly leading to uncontrolled collisions between the robot and the POI in the case of beating-heart surgery.
3. *Unregistered frames between data sources*: The POI's position measurements are taken in the image's frame of reference, whereas the real-time position of the robot, measured by the robot's encoders, is in the robot's frame of reference - see Fig. 3.3. If the robot is to follow the motion of the POI, the POI motion must be transformed from the image frame into the robot frame.

FIGURE 3.3: The robot's position measurements will be recorded with respect to the robot frame and the sensor's position measurements will be recorded with respect to the sensor frame.



### 3.2 Control Methods

The controller is an essential part of the targeted surgical system. It takes data about the heart's position (and about the surgeon's position in the teleoperated and catheter-based case) and calculates a signal such as a torque or current that will be fed to the robot, causing it to move in the desired direction. Interestingly, the choice of a control method is tied closely to the choice of the heart motion measurement method. Some motion-capture methods collect data quickly, with a negligible time delay as is the case with a video camera or a force sensor. Others, such as ultrasound imaging, take time to capture an image and introduce a non-negligible time delay into the system.

Next, the collected data is processed. This may or may not increase the time delay further. If a non-negligible time delay is present in measuring the heart's position, then the heart's latest position at any instant in time is unknown. This adds a challenge in designing a controller that must now make the surgical tool follow the heart's unknown motion accurately. If this non-negligible delay is ignored and the surgical tool is made to track heart data that is inevitably "old", there is a great risk that the surgical tool will collide with and possibly damage the heart tissue. Figure 3.4 shows such a system's poor performance [8].

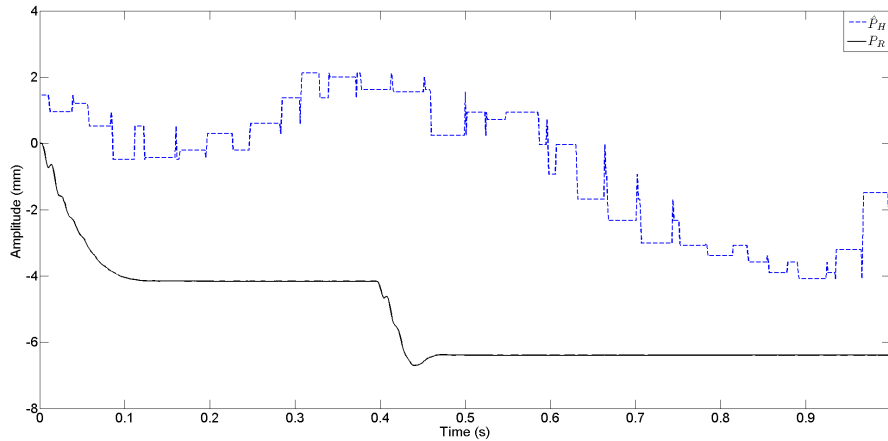


FIGURE 3.4: This diagram shows the position of the simulated heart,  $\hat{P}_H$ , (blue dotted line) and the position of the surgical tool,  $P_R$ , (solid black line) when ultrasound images are used to capture the heart's and the surgical tool's position but the time delay is not compensated for. The surgical tool does not follow the heart's position, even though it should as the surgeon's motion was set to zero. This demonstrates the need for time delay compensation [8].

To address this issue, the heart's current position needs to be estimated either by a predictive controller or a separate estimator. Different estimation techniques can be used but they all rely on the fact that the heart's motion is quasi-periodic. This means previously collected data can give us some insight about the heart's current position. If the delay is in fact negligible and the heart's position does not move significantly between the point in time when the measurement was taken and when the heart's position is calculated from that measurement, a heart motion estimator and/or a predictive controller is not necessary. However, at least fast motions of the heart make the delay compensation necessary in most practical cases, even if the delay is not too large.

As was discussed in Section 2.2, the heart's complete motion is composed of respiratory-induced motion and heart beat-induced motion. The final robot-assisted surgical system must take both sources of motion into account. As a first step, some past research has ignored the respiratory-induced motion in favour of studying how to compensate for the heart beat-induced motion, and vice versa. When the patient is in the operating room, his or her breathing is controlled by a ventilator, which makes the respiratory-induced motion almost completely periodic, much more periodic than the heart beat-induced

motion. For this reason, more emphasis has been put on tracking the heart beat-induced motion as this is more challenging.

Prior art has attempted different and sometimes intertwined methods of controlling robots to follow the heart's quasi-periodic motion. Here, we will first distinguish at a high level between two approaches to delay compensation: *prediction-based controllers*, which use the *predicted* POI's position as the reference position for the teleoperated robot, and *predictive feedback controllers*, which account for the POI measurement time delays in a *feedback* structure and are thus informed by the dynamic characteristics of the robot.

### 3.2.1 Prediction-based Controllers

Prediction-based controllers are primarily based on estimating the heart's current position from the heart's past motion. This is meant to compensate for the delay in measuring the heart's current position. Prediction-based controllers are presented in Chapters 6 and 7. Because the motion of the heart can change slightly from beat to beat, most research does not directly use the previous heart beat as an estimate of the current heart beat. Rather, data from one or more previous heartbeats are analysed and used to create a more accurate prediction of the current heart motion. Much work has been done on developing accurate mathematical models of the heart's motion [30, 44]. An overview of these methods is given in [45]. However, beat-to-beat variability is still poses a challenge.

Bebek et al. temporally align the motion from the previous heart beat to estimate the current position [36]. The temporal alignment is based on the electrocardiogram (ECG) signal. Other prediction methods address heart rate variability through the use of adaptive filters, which gradually change the length of the predicted heart beat to make it coincide with the length of the actual heartbeat [39]. Some have fit an equation to the heart's motion by exploiting its quasi-periodic nature. The heart's motion was described by a weighted sum of previously recorded heart motion data points in [14, 30].

Others modeled the heart's motion as a weighted sum of sine waves where both the amplitude and frequency are allowed to change [10, 30, 35].

### 3.2.2 Predictive Feedback Controllers

Predictive feedback controllers account for the time delay within the feedback loop. This may occur by using the heart's "old" motion and the delayed surgical tool's motion in the feedback loop as is presented in Chapter 4 and 5. Also, the heart's predicted motion can be added within the feedback loop to cancel the effect of the heart's current motion as is presented in Chapter 6. Finally, the controller may take the time delays into account directly in the cost function as is presented in Chapters 8 and 9.

Ginhoux et al. describe a two-part controller to follow the respiratory-induced motion in [13]. It uses the knowledge of the surgical robot's dynamics as well as the period of the respiratory-induced motion to make the surgical tool move in the same manner as the lungs. Then, a separate controller is introduced in [24] that follows the heart's beating motion. Others also consider both the heart beat-induced motion and respiratory-induced motion, but the heart's complete motion is measured by the force the surgical tool exerts on the heart tissue [21, 34]. Cagneau et al. use a technique where the controller learns from previous tracking errors to continually reduce the tracking error between the heart and the surgical tool [20].

A brief overview of the literature is presented in Table 3.1. The literature is categorized based on which method was used to measure the heart's motion, whether a feedforward or feedback controller was used, and which type of surgical tool was used.

	Control Method	Surgical Tool	Measurement Source
[5, 44]	Prediction	Teleoperated	Camera
[6]	Prediction	Hand-held	Pre-recorded
[7, 10, 19, 30–32]	Prediction	Hand-held	Ultrasound
[8, 46, 47]	Feedback	Teleoperated	Ultrasound
[13, 24, 25]	Feedback	Teleoperated	Camera
[14, 37, 40]	Prediction	Teleoperated	Sonomicrometry
[15]	Feedback	Catheter	Force Sensor
[17, 33]	Prediction	Catheter	Ultrasound
[18]	Prediction	Catheter	Position Sensor
[20, 22, 34, 48]	Feedback	Teleoperated	Force Sensor
[35]	Prediction	Teleoperated	Fibre Optic Probe
[36, 38, 39]	Feedback	Teleoperated	Sonomicrometry
[49, 50]	Prediction	Teleoperated	Ultrasound

TABLE 3.1: This is a summary of the literature. It is categorized based on the control method, where Prediction refers to prediction-based control and Feedback refers to predictive feedback control, the intended surgical tool, and the method of measuring the POI's position.

## Chapter 4

# Smith Predictor-based Delay Compensation

The ability to track the location of the point of interest (POI) on the heart is essential for the development of the proposed robot-assisted beating-heart surgical system. Various types of sensors have been presented to gather this information and they were explained in Sec. 2.2.

For procedures performed inside the heart, the focus of this thesis, medical images such as ultrasound should be used as they can visualize through the opaque blood pool. The downside is that medical images have a low frame rate, as low as 28 Hz in the case of 3D ultrasound scanners [30]. The location of the POI must then be found in each image, which introduces a time delay. This time delay must be compensated for; otherwise, the surgical tool may collide with and puncture the fast-moving heart.

---

Portions of this chapter have been published in “Meaghan Bowthorpe, Mahdi Tavakoli, Harald Becher, and Robert Howe. Smith predictor-based robot control for ultrasound-guided teleoperated beating-heart surgery. *IEEE Journal of Biomedical and Health Informatics*, 18(1):157-166, 2014.” and “Meaghan Bowthorpe, Mahdi Tavakoli, Harald Becher, and Robert Howe. Smith Predictor Based Control in Teleoperated Image-guided Beating-Heart Surgery. *IEEE International Conference on Robotics and Automation*, Karlsruhe, Germany, pp. 5825-5830, 2013.” [8, 46]

Once the location of the POI on the heart has been tracked, the robot-assisted surgical system will make the surgical tool follow the heart's motion. In addition, the surgeon must also be able to control the surgical tool's position in order to perform a surgical procedure. Different techniques such as hand-held tools, teleoperated tools, and catheters have been employed and they are explained in Sec. 2.1. Many, including the work in this thesis, involve a user interface for the surgeon as part of a teleoperated robot-assisted surgical system. Finally, although beyond the scope of this chapter, giving the surgeon a stabilized view of the heart will make performing the surgical task much more intuitive [28].

The proposed research in this chapter introduces a model that considers *both the time delay due to the image-based heart motion tracking and the teleoperated robot's dynamics in a feedback control structure*. While a variety of methods are used to estimate the current heart position, we augment the feedback control system with a modified Smith predictor to ensure that the teleoperated robot remains at a set distance from the heart as commanded by the surgeon's hand position despite the time delays caused by image acquisition and operations needed for calculating the heart position.

This chapter is organized as follows. The research problem is formulated in Section 4.1. Section 4.2 discusses the Smith predictor principles and Section 4.3 discusses the implementation of the Smith predictor in a teleoperated beating-heart surgical system. Sections 4.4 and 4.5 highlight simulation and experimental results, respectively. Finally, concluding remarks are given in Section 4.6.

## 4.1 Problem Formulation

The goal of beating-heart surgery is to have a teleoperated robot follow the heart at a set distance as commanded by the surgeon's hand position. To accomplish this, a control system must be designed to track the surgeon's position while compensating for the heart's repetitive beating motion. This thesis focuses on the heart's beating motion and

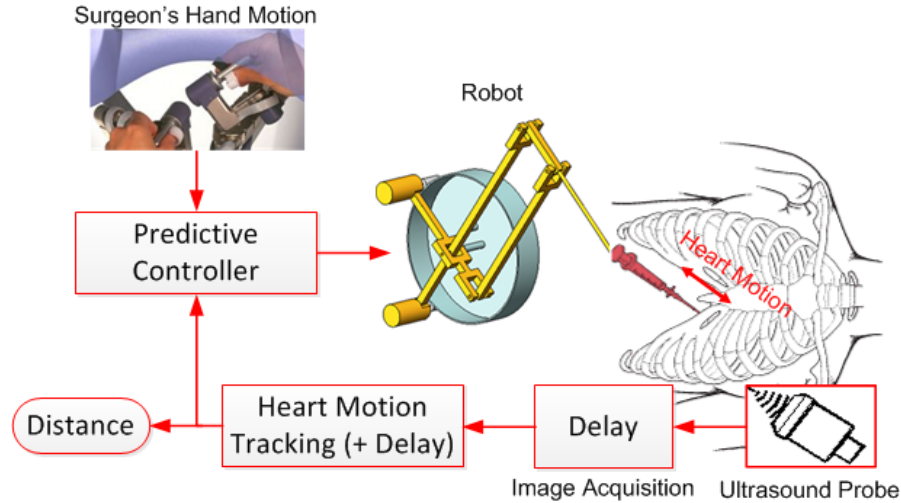


FIGURE 4.1: A diagram of the teleoperated image-guided beating-heart surgical setup [51]. The predictive feedback controllers uses both the surgeon's motion and the distance between the surgical tool and the POI on the heart to calculate the control signal.

not the translational motion caused by respiration. A diagram of the proposed robot-assisted motion compensating system is shown in Fig. 4.1. A provision for including respiratory motion has been included in [24], where the control effort coming from two controllers, one to make the surgical robot follow the heart's motion and a second to make the surgical robot follow the respiratory motion, was added together.

Before commencing the robot control design process, let us make the following observations:

- The heart motion is quasi-periodic,
- There is a constant time delay in measuring the POI's motion

Next, we will make the following assumptions:

- The robot is a linear time-invariant system and has one degree of freedom,
- The surgeon is capable of performing a surgical procedure in the presence of the above time delay if the heart motion is compensated for.

In designing the motion compensating system, we have limited the robot to one degree of freedom because two representative procedures, pericardiocentesis, the insertion of a needle through the chest wall to drain excess fluid, and mitral valve annuloplasty, attaching a ring to reshape a mitral valve that does not close properly, only require the surgical tool to be inserted into the patient along a single axis. These two representative surgical procedures have been described in more depth in Secs. 3.1.1 and 3.1.2, respectively. A Smith predictor was chosen as the controller because it remains stable though the system's output, the distance between the surgical tool and the heart,  $d_{RH}$  is measured with a known and fixed time delay.

## 4.2 Preliminaries: Smith Predictor

A Smith Predictor is a predictive feedback controller used to ensure that a closed-loop control system retains its stability and good performance in the presence of a known, fixed time delay within the loop [52]. Consider the generic feedback loops in Figs. 4.2a and 4.2b that include and do not include a time delay in the plant, respectively. If the delay is not compensated for, the performance of the feedback loop that includes a time delay in Fig 4.2b will be much worse than that of the feedback loop in Fig. 4.2a. In this situation, a Smith predictor is used to estimate the output of the plant before the delay and use this value in the feedback loop. The estimated output is then delayed and used to cancel the plant's delayed output. To begin the design of the Smith predictor, as shown in Fig. 4.2a the controller  $C$  is first designed for the no delay closed-loop system  $H$  where:

$$H = \frac{Y}{R} = \frac{CG}{1 + CG} \quad (4.1)$$

where  $G$  is the plant transfer function,  $R$  is the Laplace transform of the input, and  $Y$  is the Laplace transform of the plant output. For the delayed case in Fig. 4.2b, the controller  $C$  is replaced by  $\bar{C}$ , the Smith predictor, and the closed-loop transfer function becomes:

$$\bar{H} = \frac{Y}{R} = \frac{\bar{C}Ge^{-sL}}{1 + \bar{C}Ge^{-sL}} \quad (4.2)$$

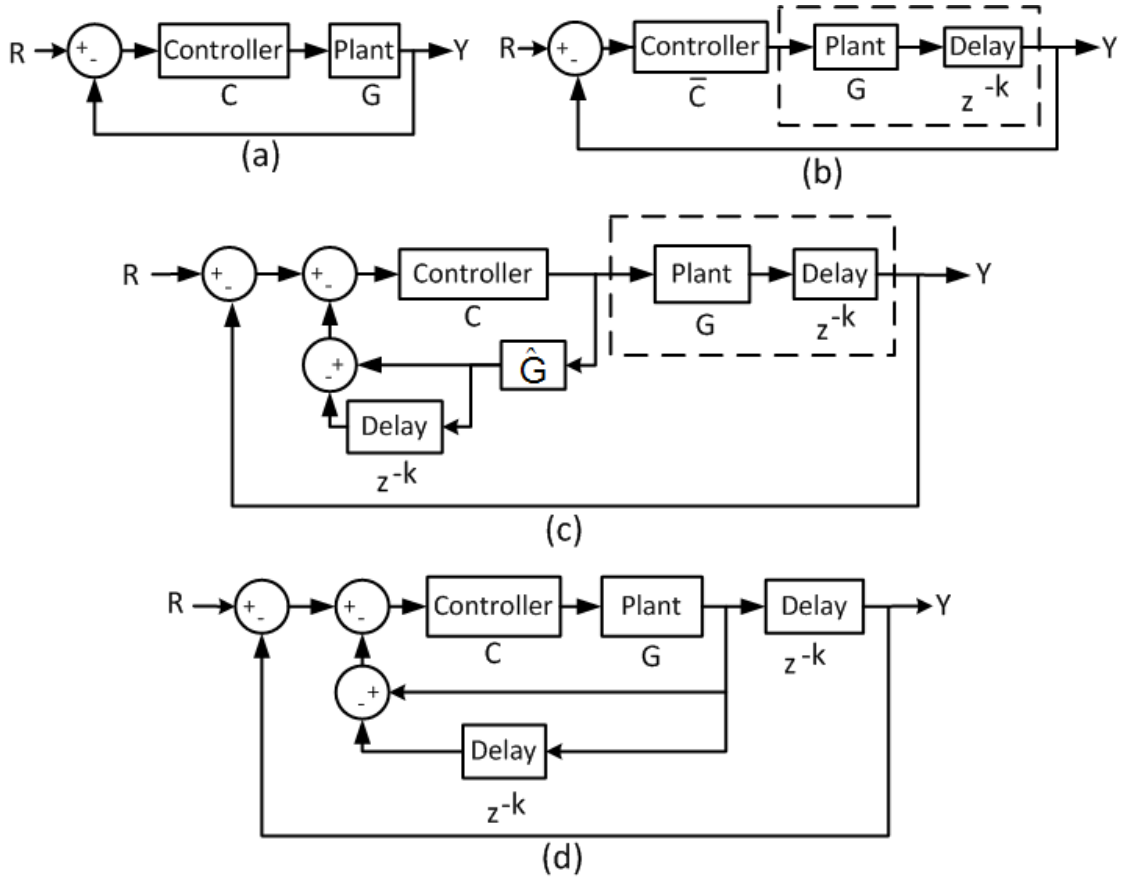


FIGURE 4.2: (A) A standard feedback controller and plant that does not include time delay. (B) A standard feedback controller and plant with time delay. (C) The Smith Predictor is added to the feedback loop where the plant's model must be estimated. (D) The Smith predictor is added to the feedback loop where the plant's model does not need to be estimated.

To retain the same performance as the not delayed system, we need  $\bar{H} = He^{-sL}$ . Therefore,  $\bar{C}$  is calculated to be:

$$\bar{C} = \frac{C}{1 + CG(1 - e^{-sL})} \quad (4.3)$$

The Smith Predictor  $\bar{C}$  as shown in Fig. 4.2c requires an estimate of the plant  $G$ . However, if the plant can be separated from the delay, we do not need the estimate of the plant's model; rather, the output of the plant can be used directly – see Fig. 4.2d.

### 4.3 Proposed Smith Predictor Based Design

A simple feedback loop representing this system is shown in Fig. 4.3a, where the system has been separated into a part that we can design, “Performed via Software”, and a part that we cannot change, “Physical System”. In fact, we cannot predict or alter the surgeon’s position nor can we change the robot’s dynamics or the heart’s motion, hence these blocks form the physical system. In contrast, we can design the controller and chose how to calculate the tissue/robot distance from the ultrasound images as these blocks are performed in the software. The inputs to the robot control system are the surgeon’s position  $p_S$  and an estimate of the heart’s current position  $\hat{p}_H$ . The measured variable, which experiences delays due to image acquisition and processing, is the distance between the robot and the heart  $d_{RH}$ . *The set-point for this distance is the surgeon’s position,  $p_S$ .* Note that the configuration in Fig. 4.3a has no provision for compensating for the heart’s motion.

As it stands, a shortcoming of the system in Fig. 4.3a is that due to the delay present in the feedback loop, it is unstable and/or has poor performance. To tackle this problem, we will use a modified Smith predictor to compensate for the delay to ensure that the system remains stable and performs well. Consequently, a prediction or an estimation of the heart’s position,  $\hat{p}_H$ , must be added to the control system – see Fig. 4.3b. The feedback loop incorporates this estimate as an additional position set-point for the robot-heart distance. This feedback loop helps the robot follow the heart’s (outdated) position as well as the surgeon’s (current) position. To add more design parameters, four gain blocks,  $K_1$ ,  $K_2$ ,  $K_3$ , and  $K_4$ , have been added: one for each feedback loop and one to scale the surgeon’s position.

#### 4.3.1 Controller Design in the Absence of Delay

In order to design a control system that will perform well under delay, it must first perform well under no delay. Therefore, the control system is first analysed without

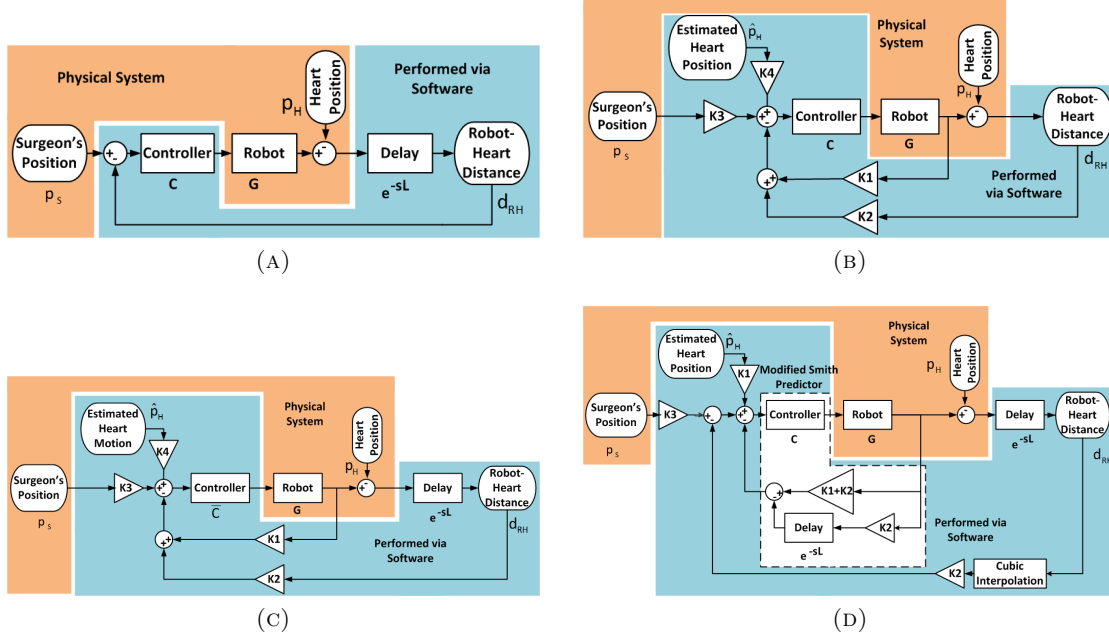


FIGURE 4.3: (a) The initial representation of the components of the feedback controller. (b) The feedback controller designed to make the robot-heart distance follow the surgeon's position. Four gain blocks are added ( $K_1$ - $K_4$ ), which increase the number of design parameters. (c) The initial controller  $C$  is then replaced by a Smith predictor. (d) The complete control loop including the modified Smith predictor.

any time delay in Fig. 4.3b. First, the transfer function between the three inputs, the estimated heart's position  $\hat{P}_H$ , the heart's actual position  $P_H$ , and the surgeon's position  $P_S$ , and the output, the robot-heart distance  $D_{RH}$ , is calculated:

$$D_{RH} = \frac{(K_4CG)\hat{P}_H - (1 + CGK_1)P_H + (CGK_3)P_S}{1 + CG(K_1 + K_2)} \quad (4.4)$$

The controller  $C$  was chosen to be a proportional controller  $C = k$ .

The goal is to make the robot-heart distance  $D_{RH}$  follow the surgeon's hand position  $P_S$ . For this reason, the steady-state value of  $D_{RH}$  is calculated when each of the inputs is a step function using the following equation:

$$d(\infty) = \lim_{s \rightarrow 0} sD_{RH}(s) \quad (4.5)$$

$$\begin{aligned}
 &= \lim_{s \rightarrow 0} s \left( \frac{K_4 CG \frac{\hat{P}_H}{s} - (1 + CGK_1) \frac{P_H}{s} + CGK_3 \frac{P_S}{s}}{1 + CG(K_1 + K_2)} \right) \\
 &\approx \frac{K_4 \hat{P}_H - K_1 P_H + K_3 P_S}{K_1 + K_2}.
 \end{aligned} \tag{4.6}$$

assuming  $CG \gg 1$ ,  $K_1 \geq 1$ , and  $K_2 \geq 0$ .

The distance,  $d(\infty)$ , given in (4.6), needs to be equal to the surgeon's position  $P_S$ , therefore the heart's position  $P_H$  and the estimated heart's position  $\hat{P}_H$  need to cancel each other. Hence, we need  $K_1 = K_4$  as the heart's past position,  $\hat{P}_H$ , should be approximately equal to the heart's current position  $P_H$ . Next, for the steady-state value  $D_{RH}$  to approach  $P_S$ ,  $K_3 = K_1 + K_2$ .

### 4.3.2 Smith Predictor Design

Once the controller has been designed for the no delay case, it is redesigned to preserve its performance when the delay is present. Hence, the new controller  $\bar{C}$  is designed to preserve the transfer function between the surgeon's position  $P_S$  and the distance  $D_{RH}$  when the time delay is present – see Fig. 4.3c. The transfer function between the surgeon's position  $P_S$  and the robot-heart distance  $D_{RH}$  for the time-delayed case, where the first two terms of (4.4) have been cancelled by equating  $K_1$  and  $K_4$  is:

$$D_{RH} = \frac{\bar{C} G K_3 e^{-sL}}{1 + \bar{C} G (K_1 + K_2 e^{-sL})} P_S \tag{4.7}$$

where  $L$  is the length of the time delay. By equating the third term of the original transfer function in (4.4) multiplied by  $e^{-sL}$  to (4.7) and substituting in the gain values found previously ( $K_1 = K_4$  and  $K_3 = K_1 + K_2$ ), the controller  $\bar{C}$  is calculated as:

$$\bar{C} = \frac{C}{1 + \hat{C} G K_2 (1 - e^{-sL})} \tag{4.8}$$

which is a modified version of the original Smith predictor given in (4.3). The final control system is shown in Fig. 4.3d where  $\bar{C}$  has been replaced by (4.8), resulting in the reappearance of the original controller  $C$ . An estimate of the robot's model is not needed as the robot and the delay are separate entities, giving us access to the output from the robot before the time delay. Hence, we do not need to estimate the robot's model. Because the ultrasound images are acquired at a slower rate than the robot's update rate, a method for upsampling the slow data is needed. The heart's principal motion has a frequency of 1 Hz and it is shown in [30] that the heart's motion can be approximated by this base frequency and the next 7 harmonics up to a frequency of 8 Hz. Because the ultrasound images are acquired at a rate of 28 Hz, the heart's motion is not aliased and the motion signal can be reconstructed using interpolation. In the simulation and experimental sections, Secs. 4.4 and 4.5, two methods will be compared: zero order hold and cubic interpolation.

### 4.3.3 POI Motion Upsampling

The POI measurements are collected at a slow sampling rate, but the surgical robot can be controlled at a much higher sampling rate. To take advantage of this, the slowly sampled position measurements should be upsampled. Two methods are chosen: zero-order-hold and cubic interpolation. In the case of a zero-order-hold, the most recent measurement value is kept until a new measurement is available. This method does not affect the delay in the system. In the case of cubic interpolation, new values are inserted in between two consecutive measurements (end points) in such a way that the derivative of the measurements at each end point and the value of each end point are preserved. The following equation describes the upsampled values.

$$\mathbf{p}(t) = h_{00}(t)\mathbf{p}_0 + h_{10}(t)\mathbf{m}_0 + h_{01}(t)\mathbf{p}_1 + h_{11}(t)\mathbf{m}_1 \quad (4.9)$$

where the  $h$  coefficients are given by

$$h_{00}(t) = 2t^3 - 3t^2 + 1 \quad (4.10a)$$

$$h_{10}(t) = t^3 - 2t^2 + t \quad (4.10b)$$

$$h_{01}(t) = -2t^3 + t^2 \quad (4.10c)$$

$$h_{11}(t) = t^3 - t^2 \quad (4.10d)$$

where  $\mathbf{p}(t)$  is the interpolated point,  $\mathbf{p}_0$  and  $\mathbf{p}_1$  are the two end points between which the interpolation is occurring,  $\mathbf{m}_0$  and  $\mathbf{m}_1$  are the slopes at the two end points, and  $t$  is a value between 0 and 1. As four sample points are required to measure the slope at each end point, this method increases the delay by the length of twice the slow sampling rate.

#### 4.3.4 POI Motion Prediction

In order for the robot-heart distance to follow the surgeon's motion, an estimate of the current heart position  $\hat{p}_H$  must be added to the system. Three different estimation methods are used in this section. The first method takes advantage of the heart's quasi-periodic motion. The delay in the system is approximately 100 ms to 150 ms and is much smaller than the length of an actual heartbeat – i.e., 667 ms to 1 s for heart rates ranging from 60 bpm to 90 bpm. Therefore, the heart position in the previous heartbeat is known and is used as an estimation of the current heart position. The estimated and actual positions are temporally aligned using the average heart rate, which is assumed to be constant and known. This method is referred to as “Fixed”. The second method uses an extended Kalman filter (EKF) to directly estimate the heart position. The trajectory

of the heart motion is modeled by an  $m$ -order Fourier series with a DC offset as in [30].

$$y(\mathbf{x}(t)) \triangleq c + \sum_{l=1}^m r_l \sin \theta_l(t) \quad (4.11a)$$

$$\theta_l(t) = l \int_0^t \omega(\tau) d\tau + \phi_l(t) \quad (4.11b)$$

$$\mathbf{x}(t) = [c(t), r_l(t), \omega(t), \theta_l(t)]^T \quad (4.11c)$$

The EKF describing the POI's motion is based on the state space model (4.12) that evolves through random walk, where the offset  $c$ , the sine wave coefficients  $r_l$ , and the frequency  $\omega(t)$  remain constant between samples. Only the  $\theta_l$  values are updated according to (4.11b) in each sample time. These values are later updated by the EKF based on the error between the predicted and actual measurement.

$$\mathbf{x}(t + \Delta t) = \mathbf{F}(\Delta t)\mathbf{x}(t) + \mu(t) \quad (4.12a)$$

$$z(t) = y(\mathbf{x}(t)) + v(t) \quad (4.12b)$$

where

$$\mathbf{F}(\Delta t) = \left[ \begin{array}{c|ccc} \mathbf{I}_{m+1} & & & \mathbf{0} \\ \hline & 1 & & \\ & \Delta t & 1 & \\ \mathbf{0} & 2\Delta t & 0 & 1 \\ & \vdots & & \ddots \\ & m\Delta t & & 1 \end{array} \right]_{[2m+2] \times [2m+2]} \quad (4.13)$$

and  $\mu(t)$  and  $v(t)$  are independent Gaussian noise terms.

Next, the EKF is updated every fast sample time by the following equations as the POI motion was previously upsampled:

$$\mathbf{P}(t + \Delta t|t) = \mathbf{F}(\Delta t)\mathbf{P}(t|t)\mathbf{F}(\Delta t)^T + \mathbf{Q} \quad (4.14a)$$

$$S = \sigma_R^2 + \mathbf{H}(\Delta t)\mathbf{P}(t + \Delta t|t)\mathbf{H}(\Delta t)^T \quad (4.14b)$$

$$\mathbf{K}(t) = \mathbf{P}(t + \Delta t|t)\mathbf{H}(\Delta t)^T S^{-1} \quad (4.14c)$$

$$\hat{\mathbf{x}}(t + \Delta t|t + \Delta t) = \mathbf{F}(\Delta t)\hat{\mathbf{x}}(t|t) + \mathbf{K}(t)(z(t + \Delta t) - y(\mathbf{F}(\Delta t)\hat{\mathbf{x}}(t|t))) \quad (4.14d)$$

$$\mathbf{P}(t + \Delta t|t + \Delta t) = (\mathbf{I} - \mathbf{K}(t)\mathbf{H}(\Delta t))\mathbf{P}(t + \Delta t|t) \quad (4.14e)$$

where  $\mathbf{P}(t)$  is the estimated covariance matrix, which is a  $[2m + 2] \times [2m + 2]$  diagonal matrix with  $[0.001, 0.1/1, 0.1/2, \dots, 0.1/l, 0.1, 0.2_{1 \times m}]$  along the diagonal,  $\mathbf{Q}$  is the process noise covariance matrix, which is also a  $[2m + 2] \times [2m + 2]$  diagonal matrix with 0.0001 along the diagonal,  $\sigma_R^2$  is the observation noise covariance matrix, which is a scalar with a value of 0.01, and  $\mathbf{H}(\Delta t)$  is

$$\mathbf{H}^T(\Delta t) = \left( \frac{\partial y}{\partial \mathbf{x}} \right)^T \bigg|_{\hat{\mathbf{x}}(t+\Delta t|t) = \mathbf{F}\hat{\mathbf{x}}(t|t)} = \begin{bmatrix} 1 \\ \sin \hat{\theta}_1(t + \Delta t|t) \\ \vdots \\ \sin \hat{\theta}_m(t + \Delta t|t) \\ \hat{r}_1(t + \Delta t|t) \cos \hat{\theta}_1(t + \Delta t|t) \\ \vdots \\ \hat{r}_m(t + \Delta t|t) \cos \hat{\theta}_m(t + \Delta t|t) \end{bmatrix} \quad (4.15a)$$

where the  $\hat{\cdot}$  symbol denotes the estimated value.

To predict future POI positions, the state matrix  $\mathbf{x}$  is multiplied  $j$  times by the update matrix  $\mathbf{F}$  to move  $j$  steps ahead:

$$\hat{\mathbf{x}}(t + j\Delta t|t + \Delta t) = \mathbf{F}(\Delta t)^j \hat{\mathbf{x}}(t + \Delta t|t) \quad (4.16)$$

## 4.4 Simulation Results

The proposed Smith predictor based controller is simulated in Simulink. The simulated heart signal is created by measuring the distance between the heart and the robot in each frame from a sequence of clinical ultrasound images throughout multiple heartbeats. A single simulated heart beat is found by averaging the corresponding distances from the heartbeats. The period of this averaged heart beat is matched to the period of a clinical ECG signal from the MITBIH database [53] to create simulated heart motion (see Fig. 4.4a). A time delay of 100 ms and an acquisition rate of 25 Hz is used to simulate the delay and down sampling caused by the ultrasound image acquisition and processing. The surgical robot was modeled as the  $y$  axis of the Phantom Premium 1.5A robot (Sensable/Geomagic, Wilmington, MA) with the transfer function given in (4.17)[54]. The gain parameters  $K_1$  and  $K_2$  are chosen to be 9 and 1, respectively. Following the guidelines set Sec. 4.3.1,  $K_3$  and  $K_4$  are then 10, and 9, respectively. The robot-heart distance should follow the surgeon's hand motion. The performance of this system is evaluated by calculating the mean of the command following error,  $e = |p_S - d_{RH}|$  and the integrated squared error  $ISE = \frac{1}{n} \sum_{i=1}^n e^2$ , where  $n$  is the number of data points.

To begin, the need for delay compensation is proven by simulating the system without the Smith predictor or the estimate of the heart motion. The robot-heart distance steadily increases as is shown in Fig. 4.4b, proving this is not a suitable control method.

Next, three trials are performed to characterize the system's performance as compared to the best possible case when the delay equals zero. The results are presented in Table 4.1. First, to have a baseline for performance comparison, the delay is removed from the system and so is the Smith predictor. The result is shown as line ND in Fig. 4.4c and line ND NSP NSM of Table 4.1. Next, the delay and the Smith predictor are returned to the system. The surgeon's position is set to zero, the slow data was upsampled using cubic interpolation, and the heart position is estimated using the method "EKF Period". The result is shown as line SP in Fig. 4.4c and line D SP NSM of Table 4.1. Then, a

$$G = \frac{s^4 + 30.25s^3 + 2.923 \times 10^5 s^2 + 5.741 \times 10^5 s + 1.784 \times 10^{10}}{1.526s^4 + 233s^3 + 2.848 \times 10^5 s^2} \quad (4.17)$$

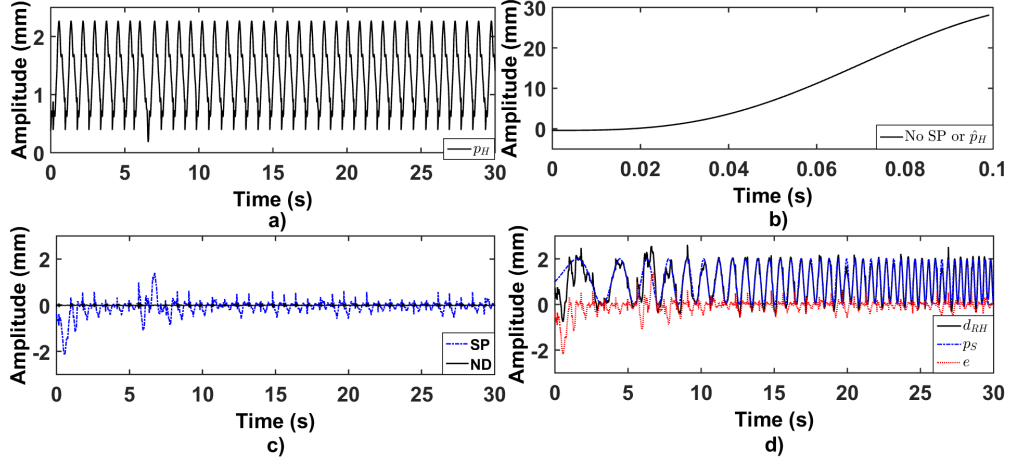


FIGURE 4.4: (a) The simulated heart motion  $p_H$ . (b) The command following error  $e$  when only a proportional controller is used, i.e., no Smith predictor or estimation of the heart's position are used even though the delay is present in the system. (c) The command following error  $e$  for the best case scenario where the delay is removed (ND) and when the Smith predictor and delay are present (SP). In both cases the surgeon's motion is set to zero. (d): The surgeon's motion  $p_S$  is a chirp signal, the robot-heart distance  $d_{RH}$  follows  $p_S$ .

chirp signal with an amplitude of 2 mm and a frequency ranging from 0.1 Hz to 2.3 Hz – see line  $p_S$  in Fig. 4.4d – is used to represent the surgeon's position as a surgeon can track motion up to 1 Hz and has voluntary motion as fast as 4 Hz to 7 Hz [55]. The robot's position  $p_R$  and the command following error  $e$  are shown in Fig. 4.4d and line D SP SM of Table 4.1. The mean command following error  $e$  and ISE match those of the case when the surgeon's position is set to zero. This suggests that the surgeon's position has little if any adverse effect on the performance of the predictive control loop.

To improve the performance of the control system, the slowly obtained robot-heart distance must be upsampled and an estimate of the heart's current motion is needed. Two methods are used to upsample the robot-heart distance in each set of trials. A zero order hold (ZOH) increases the number of measurements but does not estimate the value of the robot-heart distance between samples, whereas cubic interpolation (CI) does estimate

	Mean $e$ (mm)	ISE (mm <sup>2</sup> )
ND NSP NSM	0.45	0.033
D SP NSM	0.77	0.089
D SP SM	0.77	0.088

TABLE 4.1: Command following errors found in the preliminary simulations. D: Delay, ND: No Delay, SP: Smith Predictor, NSP: No Smith Predictor, NSM: No Surgeon Motion, SM: Surgeon Motion

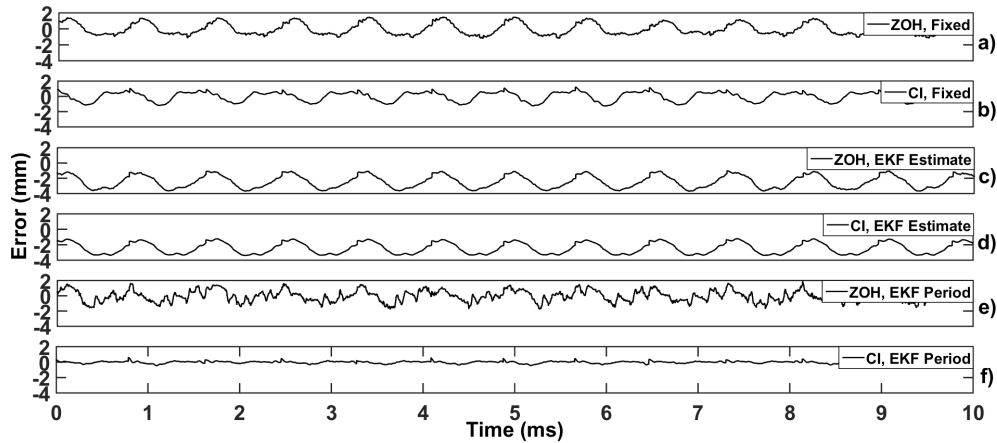


FIGURE 4.5: The error  $e$  is measured for each simulation. (a), (b) The current heart motion is estimated by the previous heart cycle when the heart rate is assumed to be fixed. A ZOH (a) and CI (b) are used to upsample the data. (c), (d) The current heart motion is estimated by the EKF. A ZOH (c) and CI (d) are used to upsample the data. (e), (f) The current heart motion is estimated by the previous heart cycle motion where the period has been changed to match the current heart period as estimated by the EKF. A ZOH (e) and CI (f) are used to upsample the data.

the value of the robot-heart distance between samples. The three methods described above are used to estimate the current heart position: “Fixed”, “EKF Estimate”, and “EKF Period”. The chirp signal described above is included as the surgeon’s position in each of the following trials. This computer-generated signal was used in the experiments in order to simulate the same user and keep the effect of the surgeon’s motion on the error the same throughout all of the remaining trials.

The effect of these upsampling and heart motion estimation methods are studied by testing each combination. The results are summarized in Fig. 4.5 and Table 4.2. For the first two trials the “Fixed” estimation method is used and the length of the heart

Estimation Method	ZOH		CI	
	Mean $e$ (mm)	ISE (mm <sup>2</sup> )	Mean $e$ (mm)	ISE (mm <sup>2</sup> )
Fixed	0.95	1.12	0.57	0.42
EKF Estimate	2.44	6.63	2.44	6.46
EKF Period	0.82	0.98	0.15	0.07

TABLE 4.2: A summary of the simulation results. Fixed: Heart position estimated from the previous heartbeat where the heart rate is assumed fixed. EKF Estimate: Heart position estimated from the EKF. EKF Period: Heart position estimated from the previous heartbeat but is period matched based on the the current heart rate estimated by the EKF.

beat is set to 803 ms, the average heart beat length. The results are shown in Figs. 4.5a and 4.5b. In the next two trials, the estimated heart rate is the value predicted by the EKF, “EKF Estimate”. The results are shown in Figs. 4.5c and 4.5d. In the last two trials, the estimated heart motion is the same as the past heart beat but its period has been matched to the current heart rate, which is estimated by the EKF, “EKF Period”. The results are shown in Figs. 4.5e and 4.5f. The cases where cubic interpolation is used to increase the sampling time (Figs. 4.5b, d, and f) have a smaller mean command following error because the position of the heart is estimated between measurements. This is important as the heart continues to move between sample times. The actual heart rate – see Fig. 4.4a – changes throughout the trial. This is why directly using the previous heart motion did not have good performance. However, the amplitude of the heartbeat remains fairly constant, hence there is value in using the shape of the past heartbeat. Estimating the current heart rate and then period matching the motion from the past heart beat along with upsampling the slow data with cubic interpolation gives the best result.

## 4.5 Experimental Results

Following the successful simulation of the system, preliminary experiments are performed with a teleoperated 1-DOF surgical tool under ultrasound guidance. The experimental setup (Fig. 4.6) includes a mechanical heart simulator and a 1-DOF surgical robot. The

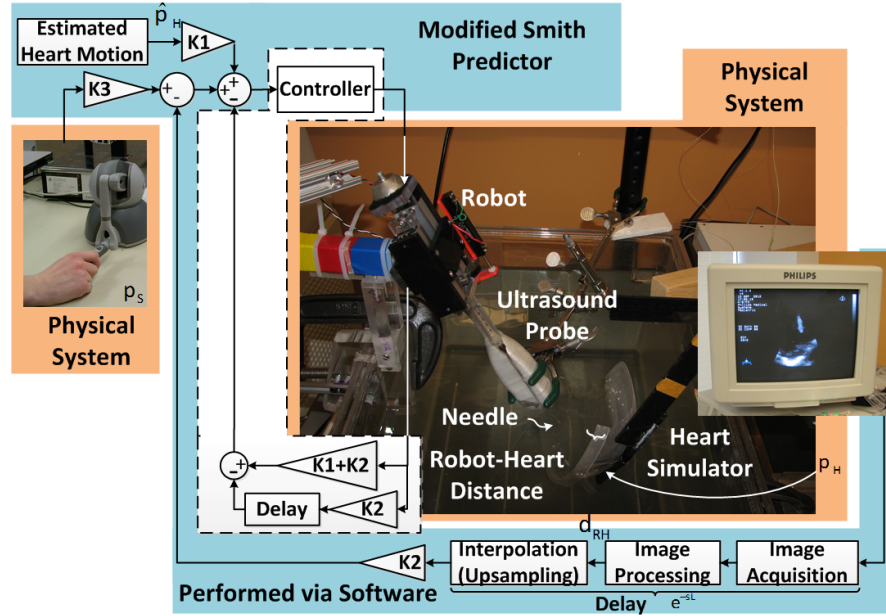


FIGURE 4.6: The experimental setup. A linear voice coil actuates a needle which follows the mechanical heart simulator and the surgeon’s motion based on ultrasound image guidance.

robot is actuated by a NCC20-18-02-1X linear voice coil motor (H2W Technologies Inc, Valencia CA). The heart simulator has a 12 mm stroke. The position of the robot is measured by a A-MAC-B62 linear potentiometer position sensor (Midori America Corp, Fullerton CA). Three dimensional ultrasound images are acquired from a SONOS 7500 (Phillips Medical, Andover, MA), which has a sampling rate of 28 Hz. The image acquisition and processing delay is 136 ms and the use of cubic interpolation further increases this delay by 71 ms. A more detailed description of the experimental setup can be found in [56].<sup>1</sup>

For this work, we use three-dimensional ultrasound images from a SONOS 7500 machine (Phillips Medical, Andover, MA) as they are non-invasive and can image the exterior and interior of the heart. A two-dimensional ultrasound image could also have been used if a needle guide [57] properly oriented the needle to ensure it is visible in the ultrasound plane. To virtually stabilize the heart via proper control of the robot, the

<sup>1</sup>These experiments were performed at the Harvard BioRobotics Lab, Harvard University, Cambridge, MA, USA. I would like to acknowledge Dr. Robert Howe and the members of the Harvard BioRobotics Lab for their guidance and assistance in completing this experiment.

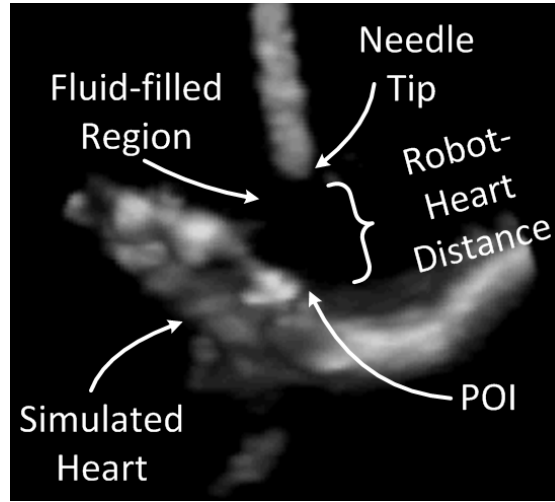


FIGURE 4.7: A 3D ultrasound image of the surgical tool and simulated heart tissue. The bright areas of the image are the simulated tissue and the needle and the dark areas are fluid-filled regions.

distance between the heart tissue and the needle tip must be measured in each image frame. This distance is calculated using the flashlight method developed by Novotny et al. [32], where the axis of the needle is found using a Radon transform. This axis is then extended towards the heart tissue. The POI (the heart wall) is the closest change from a dark area (the fluid-filled region) to a light area (the tissue) beyond the needle tip along this axis, and is marked as POI in Fig. 4.7. The distance between this tissue location and the needle tip is recorded as the robot-heart distance.

First, the need for delay compensation (Smith predictor) and the estimation of the heart position is proven. Fig. 4.8 shows the result when both the Smith predictor and the heart position estimation have been removed from the system i.e., as in Fig. 4.3a. The robot position clearly does not follow the heart's trajectory. Rather, it quickly moves to the end of its range of motion and remains there.

Next, The EKF's ability to follow a changing heart beat is tested in Fig. 4.9. The heart's motion was predicted by the EKF and cubic interpolation was used to increase the sampling rate. The estimated heart motion does, in fact, change to reflect the changing heart rate.

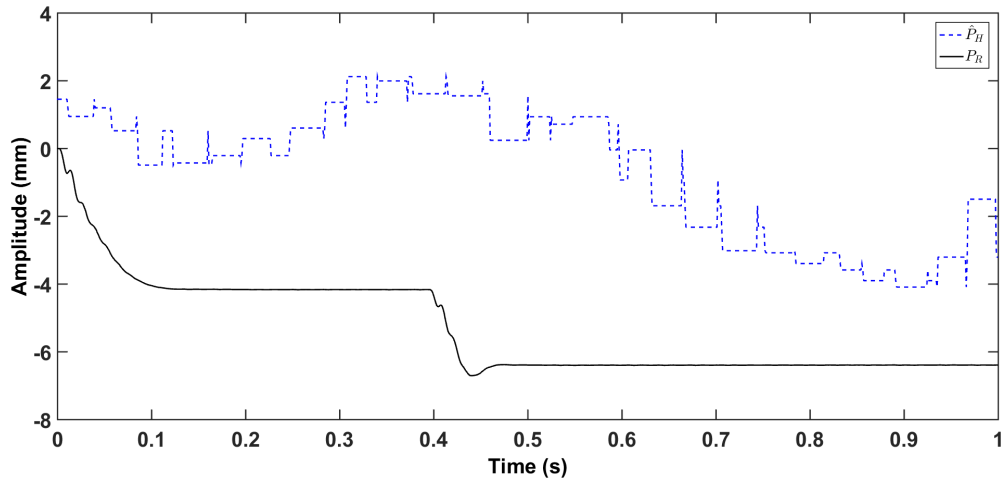


FIGURE 4.8: The necessity of the Smith predictor is shown by removing it from the system. An estimate of the heart motion is not included. The position of the robot  $p_R$  is the solid black line. It is evident that the robot moves once it is actuated, but quickly reaches the limit of it's range of motion. It does not follow the heart's motion  $p_H$ .

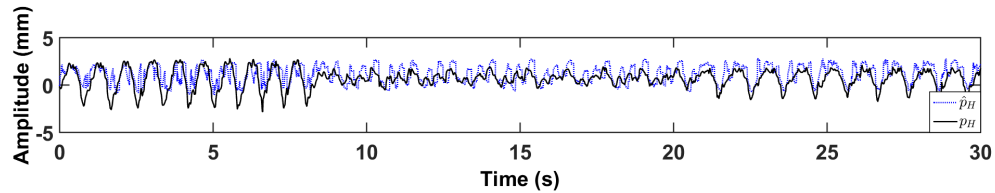


FIGURE 4.9: The EKF's ability to handle a variable heart rate is tested. The dotted blue line shows the estimated heart motion and the black line shows the actual heart motion. In this case, the prediction from the EKF was used as the estimated heart motion. Cubic interpolation was used to increase the sampling rate.

Estimation Method	ZOH		CI	
	Mean $e$ (mm)	ISE (mm <sup>2</sup> )	Mean $e$ (mm)	ISE (mm <sup>2</sup> )
Fixed	0.45	0.32	0.37	0.20
EKF Estimate	0.59	0.57	0.61	0.70
EKF Period	0.41	0.26	0.42	0.29

TABLE 4.3: A summary of the experimental results. Fixed: Heart position estimated from the previous heartbeat where the heart rate is assumed fixed. EKF Estimate: Heart position estimated from the EKF. EKF Period: Heart position estimated from the previous heartbeat but is period matched based on the the current heart rate estimated by the EKF.

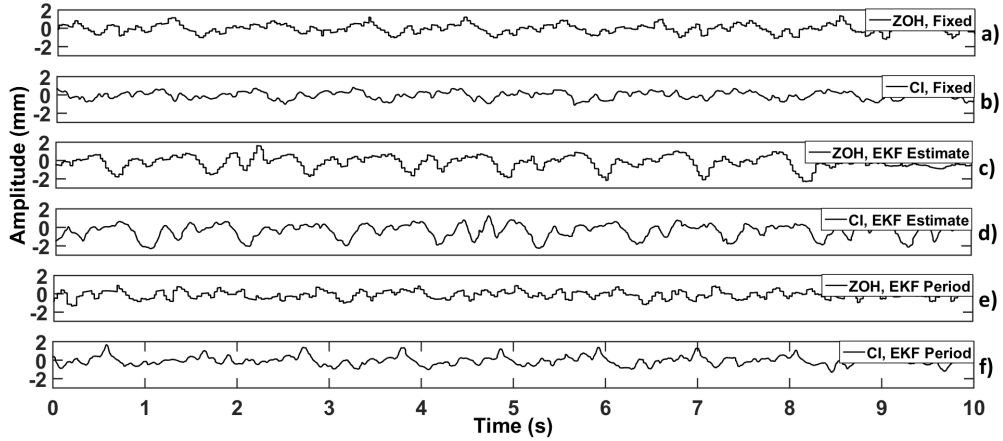


FIGURE 4.10: The command following error  $e$  is measured for each experimental trial. (a), (b) The current heart motion is estimated by the previous heart cycle when the heart rate is assumed to be equal to the average heart rate and remains fixed. (c), (d) The current heart motion is estimated by the EKF. (e), (f) The current heart motion is estimated by the previous heart cycle motion where the period has been changed to match the current heart period as estimated by the EKF. A ZOH (a), (c), and (e) and CI (b), (d), and (f) are used to upsample the data.

Finally, six trials evaluating the different upsampling and heart position estimation methods are performed. The results are given in Fig. 4.10 and Table 4.3. First, the past-cycle heart position is directly used as the estimated heart position, “Fixed”. The results are given in Figs. 4.10a and b. Then, the EKF is used to estimate the heart position, “EKF Estimate”. The results are given in Figs. 4.10c and d. Finally, the estimated heart position is obtained by delaying the previous heart beat by the length of the current heart beat, which is calculated by the EKF, “EKF Period”. The results are given in Figs. 4.10e and f.

It is shown in Fig. 4.10 that the Smith predictor based control method is able to keep the system stable. Using cubic interpolation helps to reduce the average absolute error as it corrects for the loss of data caused by downsampling during image acquisition. From the simulation results, we expect that using the past heart beat but matching its period to the current period, which is estimated by the EKF, to have the best performance. However, as the heart rate remained fairly constant throughout the trials, both the case when the heart motion is estimated by directly delaying the previous heart motion and

the case where this estimate was period-matched to the current heart rate as estimated by the EKF have similar performance. Using the estimate of the EKF directly did not perform as well because the estimate from the EKF has a smaller amplitude than the actual heart motion.

The magnitude of the tracking error in the proposed method is similar to those reported by others. It is difficult to make an accurate comparison between the proposed method and others as they use different approaches to measure the heart's motion and some methods simply ignore the surgical robot's dynamics. Kettler et al. asked participants to draw a circle between two concentric circles that were attached to a platform that moved in a manner similar to the mitral valve [6]. This study used a hand-held tool and, therefore, the robot's dynamics were not considered. It was shown that when the motion-compensating tool was used, participants were able to draw 80% of a circle between the two concentric circles as opposed to less than 60% when a solid tool was used. Bebek et al. made a surgical robot follow the heart's motion [36], but the heart's position was measured by sonomicrometry crystals, which means that they did not have to consider the delay caused by ultrasound image acquisition and processing that is inherent to the system architecture considered in this work. They reported root mean squared (RMS) errors in the range of 0.68 mm. Yuen et al. made a hand-held surgical tool follow the heart's motion under ultrasound guidance [30]. The delay was considered but the surgical robot's dynamics were not. They reported RMS errors of 1.43 mm. Frank et al. used adaptive filters to follow pre-recorded heart motion [39]. This study reported RMS errors of 0.5 mm. Ginhoux et al. followed the heart's motion with a mean tracking error of 0.08 mm and a maximum tracking error of 0.256 mm [24]. This study considered the surgical robot's dynamics but a 500 Hz video camera was used to capture the heart's motion and hence the image acquisition and processing delays were negligible. The largest mean error reported in the proposed research was 0.61 mm, which is comparable to the mean errors reported by other groups. This is while the proposed method deals with both delays and robot dynamics at the same time, which is more challenging compared to past work.

## 4.6 Concluding Remarks

This chapter proposed a predictive feedback control scheme based on a Smith predictor for image-guided teleoperated beating-heart surgery. This predictive control system ensures that the distance between the heart wall and the robot's end-effector (i.e., surgical instrument) is commanded by the surgeon's position that is input via a user interface. To estimate the heart's position, ultrasound images are used because they are inexpensive to obtain, minimally invasive, and can visualize through blood as required for intracardiac surgery. The Smith predictor successfully compensated for the time delays caused by image acquisition, processing, and possibly cubic interpolation-based upsampling as the system did not become unstable in any of the experimental trials. Of the two interpolation methods tested, cubic interpolation performed better. This was expected as cubic interpolation fills in the space between the position measurement data points such that the derivative of the motion is smooth. Zero-order-hold, on the other hand, simply keeps the same position value until the next measurement is obtained and does not reflect the POI motion that occurs between position measurements.

## Chapter 5

# Development of a Robot-assisted Beating-heart Surgical Testbed with Smith Predictor-based Delay Compensation

This chapter explains the development of a robot-assisted beating-heart surgical system test bed. A new Smith predictor configuration is introduced, where the disturbance caused by the heart's motion is better accounted for as compared to the configuration presented in Chapter 4. Many surgical procedures can benefit from a robot-assisted beating-heart surgical system. Even surgical procedures performed on organs other than the heart that are subject to periodic respiratory motions can benefit. For example, radiation treatments can be delivered more precisely if the laser beam moves in synchrony with the motion of the affected organ [58].

---

Portions of this chapter have been published in “Meaghan Bowthorpe, Vincent Castonguay-Siu, and Mahdi Tavakoli. Development of a Robotic System to Enable Beating-heart Surgery, *Journal of the Robotics Society of Japan*, invited paper, vol. 32, no. 4, pp. 339-346, 2014.”[47]

Synchronizing the surgical tool with the heart’s motion is more difficult than for other organs as the heart’s motion is composed of fast and small heartbeat-induced motion in addition to the slow and large respiration-induced motion that affects other organs. As a starting point, surgical procedures requiring one-dimensional motion tracking are considered. These include pericardiocentesis, where a needle is inserted into the pericardial sac surrounding the heart to drain the excess fluid. During this procedure, the needle should remain within the pericardial sac but should not puncture any blood vessels on the surface of the heart. Motion synchronization can aid in preventing this type of a hazard. Mitral valve annuloplasty also requires one-dimensional motion tracking [6]. The surgeon can reshape the mitral valve annulus by stapling an annuloplasty ring within it and evaluate the performance of the newly shaped valve on the fly. These two procedures are discussed in more detail in Secs. 3.1.1 and 3.1.2, respectively.

The design of the experimental testbed is given in Sec. 5.1 including the structure of the surgical tool and the design of a mechanical simulator for a beating heart. The feedback control that synchronizes the motion of the surgical tool with that of the POI on the heart and adds the surgeon’s motion in through teleoperation is discussed in Sec. 5.2. The experimental results concerning the system performance and stability are presented in Sec. 5.3. Concluding remarks are given in Sec. 5.4.

## 5.1 Experimental Testbed Design

The experimental testbed, built in the Department of Electrical and Computer Engineering at the University of Alberta, includes the (motorized) surgical tool, a Micron Tracker (model HX60 from Claron Technology Inc., Toronto, Ontario, Canada), and a mechanical heart simulator. The surgical tool as explained below allows for the synchronization between the surgical tool’s tip and the POI on the beating heart along one dimension. The Micron Tracker is used to simulate an ultrasound scanner as its frame rate of 20 Hz is similar or lower than the frame rate of an ultrasound scanner. The Micron Tracker also has a lag of 85 ms and an image processing delay of 20 ms in its

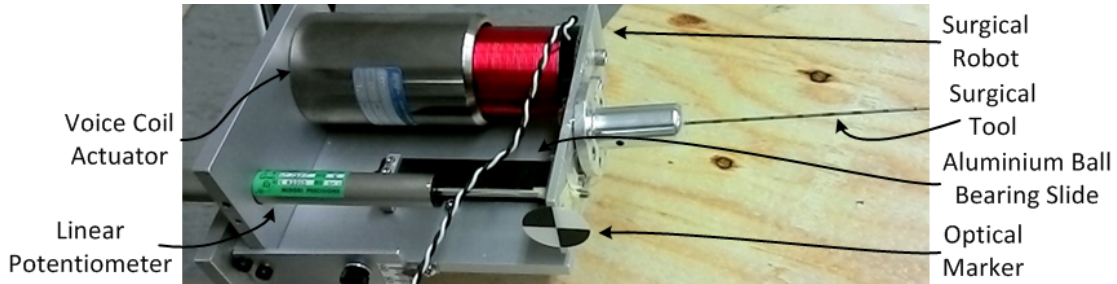


FIGURE 5.1: A close up view of the surgical tool, which is moved by a voice coil actuator. The aluminum ball-bearing linear slide confines the motion to a single dimension. A linear potentiometer measures the position of the voice coil actuator in real-time. The optical marker is required for the Claron Microtracker to measure the position of the voice coil actuator.

software. Therefore, the complete image acquisition and processing delay is approximately 105 ms. This is similar to the 150 ms image acquisition and processing delay of ultrasound images found by Yuen et al. [30]. The mechanical heart simulator designed based on the movement of a single point on the exterior of the heart calculated from ultrasound images is used to represent the POI on the beating heart.

### 5.1.1 Surgical Robot Structure

The surgical robot is designed to synchronize the motion of a surgical tool (needle) with the heart's motion along a single dimension. The surgical tool must have a range of a few centimeters and have the ability to move with velocities of 210 mm/s and accelerations of 3800 mm/s<sup>2</sup> in order to mimic the peak velocities and accelerations of the heart [6]. To meet these requirements, a voice coil actuator (NCC20-18-020-1X from H2W Technologies Inc., Santa Clarita, CA, USA) was chosen to create the necessary back-and-forth tracking motions of the surgical tool. An aluminum ball-bearing linear slide (6203K89 from McMaster-Carr, Aurora, OH, USA) is used to ensure this motion is confined to one dimension. To measure the displacement of the surgical tool (and the voice coil actuator) in real-time, a linear potentiometer (LP-75FP from Midori America Corp., Fullerton, CA, USA) is mounted on the robot. A diagram of the this tool is shown in Fig. 5.1.

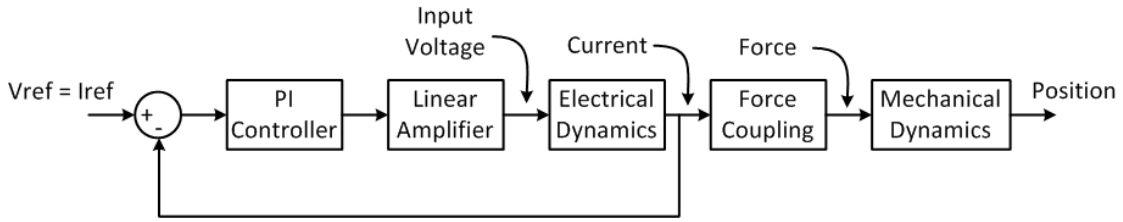


FIGURE 5.2: The electrical and mechanical characteristics of the analog controller that controls the position of the voice coil actuator.

The motion of the voice coil is controlled by applying a voltage across the coil. The resulting current creates a magnetic field which either pushes the coil out of or pulls the coil into the cylindrical permanent magnet acting as the actuator’s base. This motive force is proportional to the current passing through the coil, thus necessitating an internal current control loop as part of any system for feedback control of the voice coil’s position. A block diagram of the steps involved in controlling the position of the voice coil is given in Fig. 5.2 and the circuit diagram is shown in Fig. 5.3.

This circuit has four stages: the computation of error, the proportional-integral (PI) controller, the buffer, and the current measurement and feedback. The first section of this circuit calculates the error between the reference voltage  $V_{ref}$  representing the desired current and the voltage  $V+$  that, as explained later, is proportional to the current passing through the voice coil. The second section generates PI action based on this error. If the output of the PI controller is connected directly to the voice coil, there will be a loading effect meaning that the voltage will be reduced once any current is drawn. Therefore, the third stage of the circuit, which is a buffer (a linear amplifier from Quanser Inc. Markham, Ontario, Canada), ensures that the voltage remains unchanged while supplying a sufficient current to the voice coil. Finally, the actual current passing through the coil is calculated by measuring the voltage across a small ( $0.3 \Omega$ ) resistor placed in series with the coil and amplifying it using the fourth stage of the circuit to the range between  $-10 \text{ V}$  to  $10 \text{ V}$ . The output is the measured voltage  $V+$  used for the initial error calculation in the first stage of the circuit.

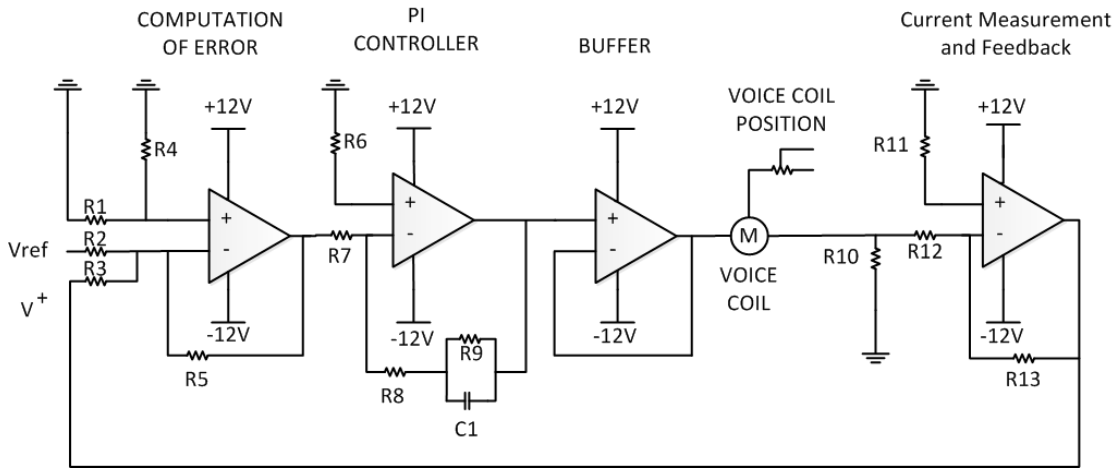


FIGURE 5.3: The circuit diagram of the analog control loop responsible for the current control of the voice coil actuator.

### 5.1.2 Simulated Heart Structure

A mechanical oscillator was built to mimic the movements experienced by a single point on a human heart. The cyclic oscillation to be replicated was extracted from the actual motion of a single point on the exterior heart wall from a series of ultrasound images. The final design utilized a mechanical cam to convert the rotational movement of a DC motor into linear movement which would then be extended into a large container full of water using arm links (a section of the device is to be used underwater whilst permitting clear visualization under ultrasound). The mechanical oscillator's target displacement away from its starting position was set to approximately 1 cm while it must have the potential to reach a maximal displacement of 3 cm with only minor adjustments to the cam. A diagram of a mechanical cam is shown in Fig. 5.4. As the cam rotates about its axis, the rectangular arm is moved back and forth in a way that is dependent on the cam's shape. The cylindrical cam is connected to a DC motor (DC Gearmotor 6331K33 from McMaster-Carr, Aurora, OH, USA) permitting control over the cam's speed and torque. The final mechanical design is shown in Fig. 5.5.

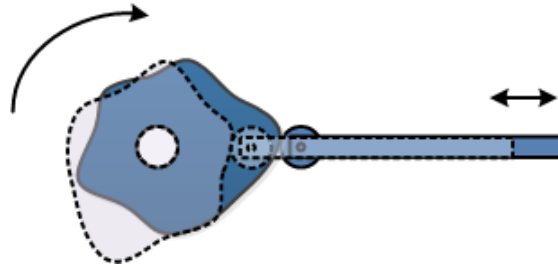


FIGURE 5.4: This mechanical cam converts rotational motion into linear motion. As the cam rotates, it moves the rectangular arm linearly.

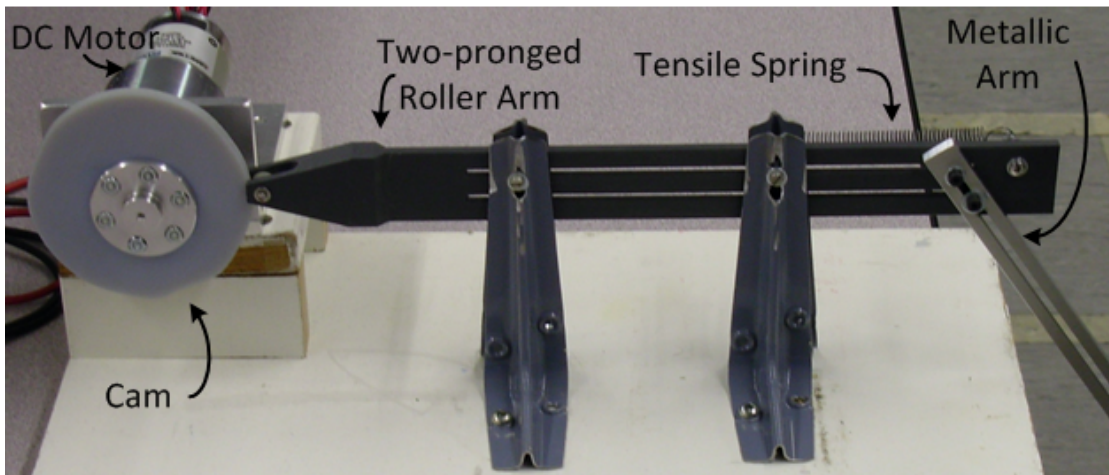


FIGURE 5.5: The mechanical oscillator built to mimic the motion of a single point on the heart. A mechanical cam is used to convert rotational motion into linear motion.

## 5.2 Feedback Control of Surgical Tool

To successfully design a robot-assisted beating-heart surgical system, several requirements must be met. Because ultrasound imaging was chosen for this work, a non-negligible time delay of approximately 40 ms is introduced into the system for image acquisition. Each image frame must then be processed to determine the location of the surgical tool and the heart as is shown in Fig. 5.6. A Radon transform, which finds the longest straight line in an image, is proposed to find the surgical tool [32]. The ultrasound image acquisition and processing adds a time delay of approximately 150 ms [30] into the system. The controller designed in this chapter must be able to accommodate such a large delay; otherwise, the surgical tool may collide with the heart. In

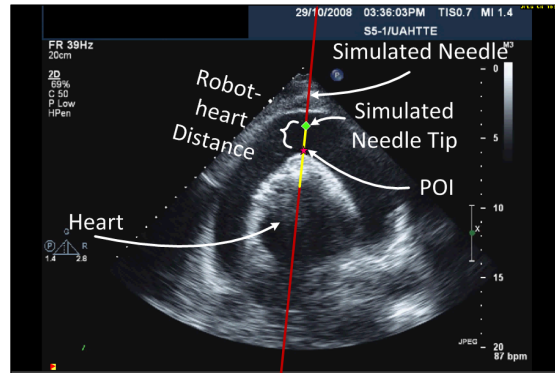


FIGURE 5.6: An ultrasound image of the heart and a simulated surgical tool (needle). First, the axis of the surgical tool is found and extended across the entire image. Then, moving along this axis the location of the surgical tool tip and the closest heart tissue is found.

addition, the ultrasound images are slowly sampled and the POI motion data should be upsampled improve the tracking results.

### 5.2.1 POI Motion Upsampling

The choice of the sampling time used to acquire the images and control the surgical robot merits further discussion. The image acquisition sampling time is limited to 50 ms or 20 Hz for this experimental setup due to the frame rate of the Micron Tracker. To determine the sampling speed required to control the surgical tool, a spectral decomposition of the heart's beating motion is required. Fig. 5.7a shows the shape of the motion of a POI on beating heart taken from ultrasound images and the frequencies present in the motion are given in Fig. 5.7b. The highest frequency component is less than 4 Hz. To follow this motion, the minimum sampling frequency according to the Nyquist theorem is 8 Hz. However, it is better to have a much higher sampling rate. Yuen et al. reported the highest frequency component in the motion of the mitral valve to be approximately 12 Hz [10] and would require a minimum sampling frequency of 24 Hz. Better tracking is possible if the sampling frequency is approximately eight times greater than the maximum frequency present, which is 96 Hz for the case of the mitral valve's motion. For this chapter, a sampling frequency of 100 Hz is chosen.

Two methods have been chosen to increase the sampling rate of the POI motion from 20 Hz to 100 Hz: zero-order-hold and cubic interpolation. In the case of a zero-order-hold, the newest measurement value is kept until a new measurement is available. This method does not affect the delay in the system. In the case of cubic interpolation, new values are inserted in between two consecutive measurements (end points) in such a way that the derivative of the measurements at each end point and the value of each end point are preserved. The following equation describes the upsampled values.

$$\mathbf{p}(t) = h_{00}(t)\mathbf{p}_0 + h_{10}(t)\mathbf{m}_0 + h_{01}(t)\mathbf{p}_1 + h_{11}(t)\mathbf{m}_1 \quad (5.1)$$

where the  $h$  coefficients are given by

$$h_{00}(t) = 2t^3 - 3t^2 + 1 \quad (5.2a)$$

$$h_{10}(t) = t^3 - 2t^2 + t \quad (5.2b)$$

$$h_{01}(t) = -2t^3 + t^2 \quad (5.2c)$$

$$h_{11}(t) = t^3 - t^2 \quad (5.2d)$$

where  $\mathbf{p}(t)$  is the interpolated point,  $\mathbf{p}_0$  and  $\mathbf{p}_1$  are the two end points between which the interpolation is occurring,  $\mathbf{m}_0$  and  $\mathbf{m}_1$  are the slopes at the two end points, and  $t$  is a value between 0 and 1. As four sample points are required to measure the slopes at each end point, this method increases the delay by the length of twice the slow sampling rate.

### 5.2.2 POI Motion Prediction

As the purpose of this chapter is to introduce the new experimental setup, a simple prediction algorithm was used to predict the delay POI motion measurements to the

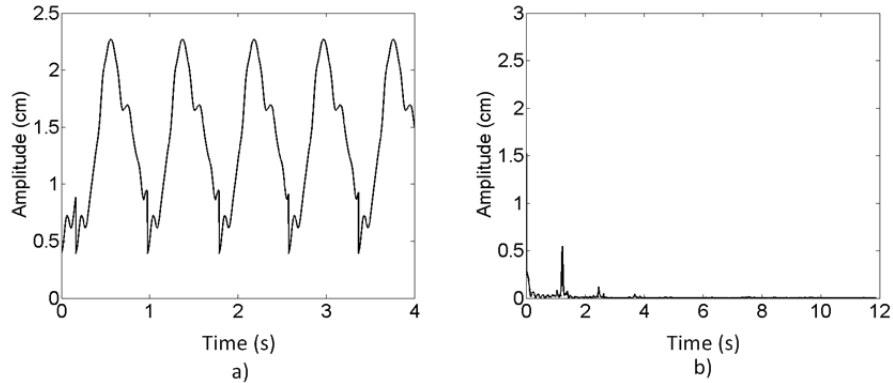


FIGURE 5.7: a) The motion of a heart beat taken from ultrasound images and temporally matched to an ECG signal to create a series of heart beats. b) The frequency spectrum of the heart beats.

current time. The simple case of a constant heart rate was considered, and as a mechanical cam generated the POI motion, the amplitude of the motion does not change. Hence, the period of the generated POI motion was measured before the experiments were performed and the current motion of the POI was predicted as the motion of the POI one period earlier in time.

### 5.2.3 Predictive Feedback Control

The feedback control system is responsible for synchronizing the movement of the surgical tool with that of the POI, and additionally superimposing the surgeon's motion onto the surgical tool's motion. In other words, the feedback controller should be designed where the input (setpoint) is the surgeon's position and the output (controlled variable) is the *distance* between the POI and the surgical tool. As mentioned before, a complicating factor is that measuring the positions of the POI and the surgical tool is subject to delays due to the ultrasound image acquisition, processing, and possibly upsampling. Using the delayed measurement in the feedback loop may cause instability and lead to collisions between the heart and the surgical tool.

In this chapter, a Smith predictor is used to compensate for this delay by effectively removing it from within the feedback loop [52]. It is assumed that the dynamical model

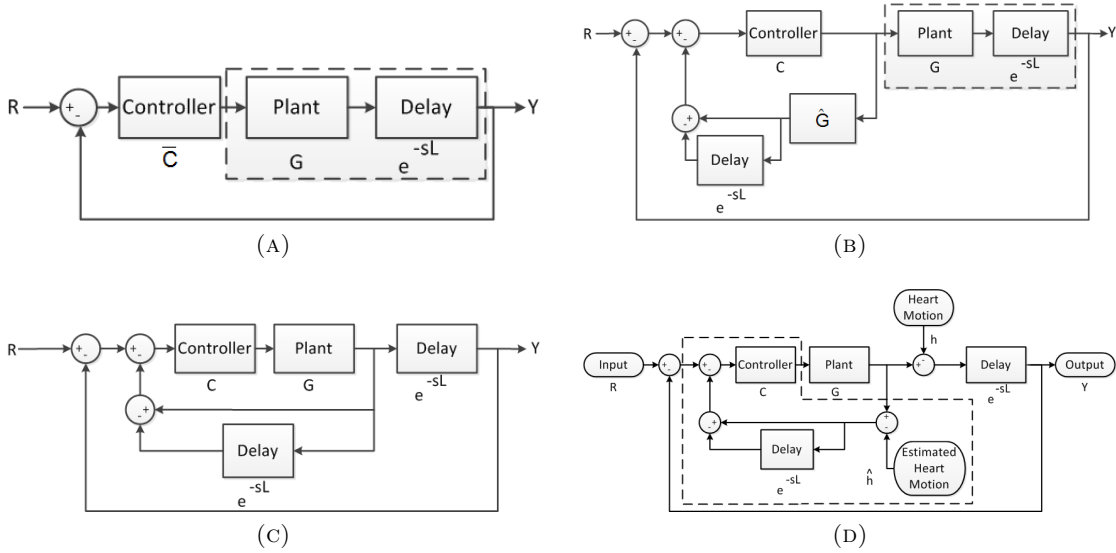


FIGURE 5.8: Diagrams a) through d) show the development of a Smith predictor controller. a) A feedback loop with a time delay. b) The same feedback loop with the addition of a Smith predictor controller. c) The Smith predictor is altered because the actual output of plant  $G$  is accessible. d) The final Smith predictor controller where the actual and estimated heart motion has been included.

of the surgical robot (plant) and the length of the delay are known or can be estimated. Consider the feedback loop with setpoint  $R$ , controller  $\bar{C}$ , plant  $G$ , delay  $e^{-sL}$ , and output  $Y$  in Fig. 5.8a. The Smith predictor,  $\bar{C}$  is calculated in the same manner as in Chapter 4.

$$\bar{C} = \frac{C}{1 + CG(1 - e^{-sL})}. \quad (5.3)$$

Note that the above expression for  $\bar{C}$  matches the Smith predictor's control system shown in Fig. 5.8b.

This thesis presents a special case of this scenario where the delay is caused by the imaging. While the distance between the positions of the POI and the surgical tool is only known after the delay, the surgical robot's position is known in real-time (from robot encoders or external trackers). Therefore, we employ a modification of the Smith predictor shown in Fig. 5.8c that has the same functionality as the system in Fig. 5.8b. A

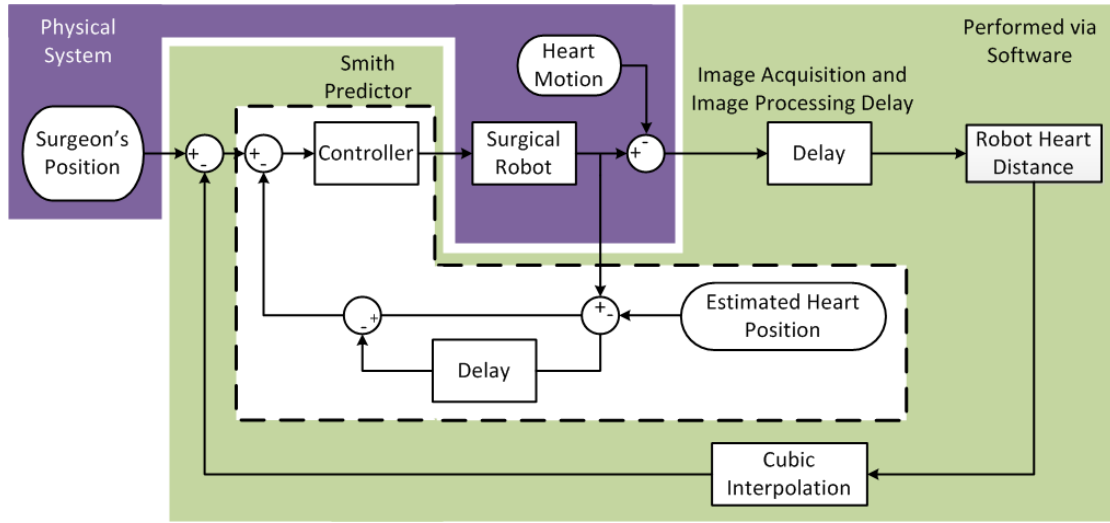


FIGURE 5.9: The final model of the Smith predictor based control loop to ensure that the distance between the surgical tool and the POI follows the surgeon’s motion.

further necessary modification, an improvement over the Smith predictor configuration discussed in Chapter 4 is shown in Fig. 5.9. The “current” position of the POI (Heart Motion block), though we can only measure the delayed value, acts as a disturbance in the feedback loop in Fig. 5.9. Hence, a “prediction” of the current position of the POI (Estimated Heart Position block) is added to the interior feedback loop of the Smith predictor. In this way, the Smith predictor compensates for the time delay in acquiring the distance between the POI and the surgical tool by using the real-time position of the surgical tool and estimating the POI’s current position (e.g., based on past POI position and electrocardiography signals).

Next, the heart motion is modeled as a disturbance  $h$ . The sensitivity function of such a disturbance if introduced after the plant in the non-delayed feedback loop shown in Fig. 5.8a would be:

$$\frac{Y}{h} = \frac{-1}{1 + CG} \quad (5.4)$$

To maintain this same sensitivity function once the delay is included in the system, an estimate of the current heart motion is added to the inner feedback loop as is shown in

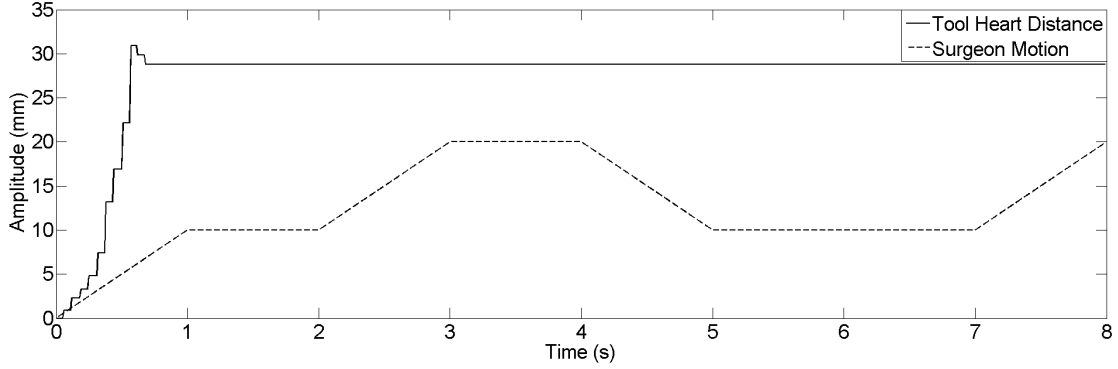


FIGURE 5.10: The motion of the surgeon and the distance between the tool and the heart when the Smith predictor is not present.

Fig. 5.8d. If the estimated heart motion  $\hat{h}$  is the same as the actual heart motion  $h$ , the sensitivity function will reduce to the following

$$Y = \frac{-he^{-sL}}{1 + CG} + \frac{(\hat{h} - h)(1 - e^{sL})CGe^{-sL}}{1 + CG} \approx \frac{-he^{-sL}}{1 + CG} \quad (5.5)$$

which is the equivalent to (5.4) multiplied by the delay. The complete model of the feedback control system is shown in Fig. 5.9.

### 5.3 Experimental Results

Initially, the Smith Predictor is removed from the system and only the controller  $C$  is used in the delayed feedback loop. The results are given in Fig. 5.10, where the solid line is the distance between the surgical tool and the heart and the dashed line is the surgeon's motion. The tool moved to its limit point and remained there. This performance is not acceptable.

Next, the Smith predictor is returned to the system and the slow data signals are up-sampled using a zero-order-hold. The actual and predicted heart motion are shown in Fig. 5.11 by the dashed and solid lines, respectively. The distance between the tool and the heart and the surgeon's motion are shown in Fig. 5.12 by the solid and dashed lines, respectively. In this case, the distance between the tool and the heart, measured with

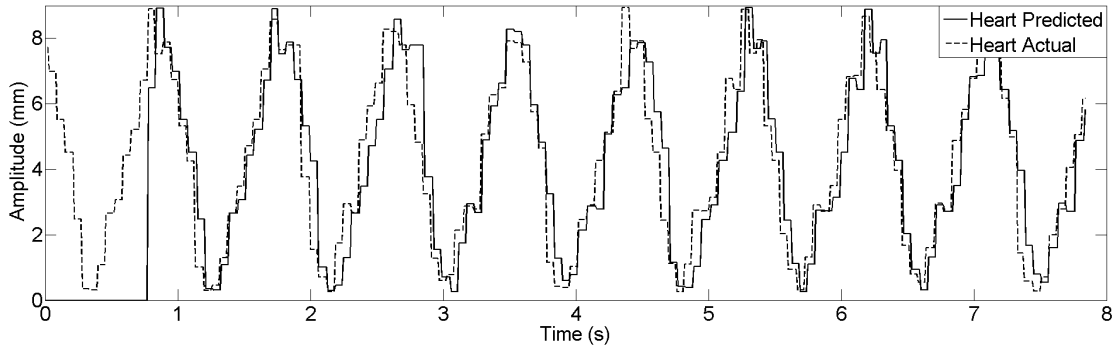


FIGURE 5.11: A comparison of the actual and predicted heart motion when a zero-order-hold is used to increase the sampling rate of the data collected from the ultrasound images.

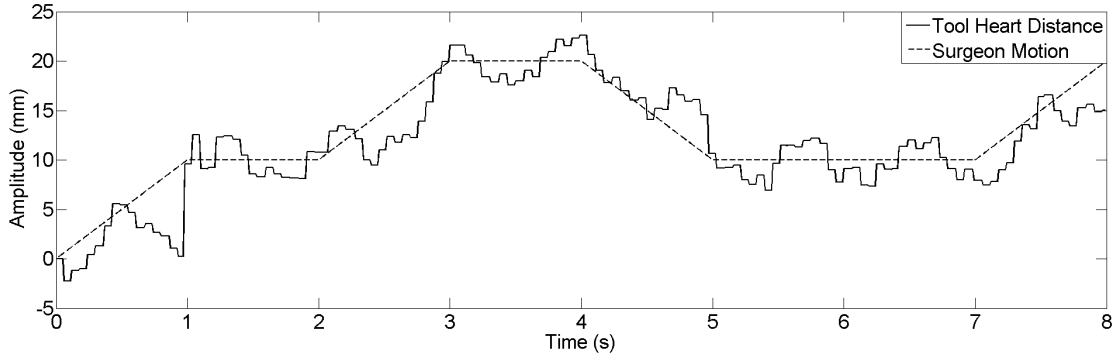


FIGURE 5.12: The motion of the surgeon and the distance between the tool and the heart when a zero-order-hold is used to increase the sampling rate of the data collected from the ultrasound images.

a delay from the images, follows the surgeon’s motion with a delay. The mean absolute error and the integrated squared error (ISE), which is  $\frac{\sum \epsilon^2}{n}$  where  $\epsilon$  is the error value and  $n$  is the number of data points, between the surgeon’s motion and the distance between the tool and the POI are 2.9 mm and 6.0 mm<sup>2</sup>, respectively.

Next, cubic interpolation is used to upsample the slow data signals. The actual and predicted heart motion are shown in Fig. 5.13 by the dashed and solid lines respectively. The distance between the tool and the heart and the surgeon’s motion are shown in Fig. 5.14 by the solid and dashed lines, respectively. The mean absolute error and ISE between the surgeon’s motion and the distance between the tool and the POI are

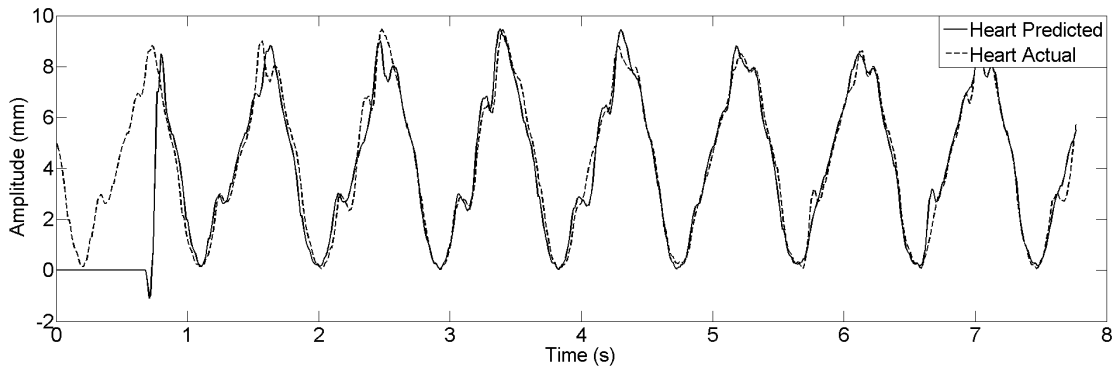


FIGURE 5.13: A comparison of the actual and predicted heart motion when cubic interpolation is used to increase the sampling rate of the data collected from the ultrasound images.

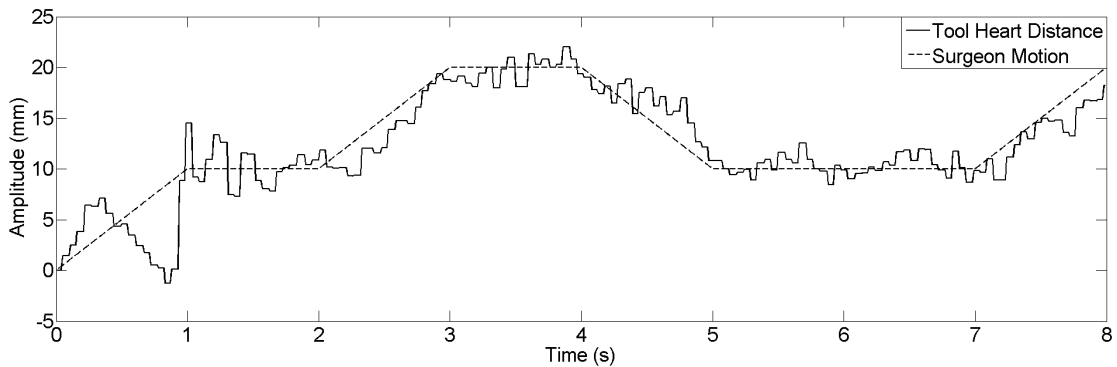


FIGURE 5.14: The motion of the surgeon and the distance between the tool and the heart when cubic interpolation is used to increase the sampling rate of the data collected from the ultrasound images.

0.55 mm and 0.80 mm<sup>2</sup>, respectively, a noticeable improvement over the use of zero-order-hold upsampling. In this case the distance between the tool and the heart follows the surgeon's motion more closely than the zero-order-hold case except that the delay is longer. In both cases, the predicted heart motion does not follow the actual heart motion immediately because the motion of one heart beat must be collected as the predicted heart motion is the motion of the POI in the previous heart beat. These experimental results have been summarized in Table 5.1.

Upsampling Method	Error	
	MAE (mm)	ISE (mm <sup>2</sup> )
Zero-order-hold	2.9	6.0
Cubic Interpolation	0.55	0.8

TABLE 5.1: A summary of the experimental results. The current POI motion was predicted from the previous POI motion

## 5.4 Concluding Remarks

An experimental testbed is designed to test the controllers proposed for motion compensation in robot-assisted beating-heart surgery. The heart motion is produced by a mechanical cam and the surgical tool is actuated by a voice coil to ensure that fast tracking is possible. The control system based on a Smith predictor was tested using both a zero-order-hold and cubic interpolation to increase the sampling rate of the slowly sampled data collected from the ultrasound images. It is shown that the use of cubic interpolation reduces the tracking errors but increases the delay.

The Smith predictor presented in this chapter should perform better than the configuration presented in Chapter 4, because the setpoint for the output, the distance between the surgical tool and the POI, is the surgeon's motion and not the combination of the surgeon's motion and the predicted POI motion as it was in Chapter 4. Also, the disturbance caused by the POI motion is cancelled in the inner feedback loop with the subtraction of the estimated POI position. This was not considered in Chapter 4. Even though we expected to receive smaller tracking errors, those of Chapter 4 are actually smaller. However, this is not a fair comparison as two different experimental setups were used, and the POI motion generated by the mechanical cam was similar, but not the same. Both Smith predictor configurations are tested on the same experimental setup in Chapter 6.

## Chapter 6

# A Comparison of Proportional and Smith Predictor-based Control for Registered and Unregistered Measurements

As was discussed in Chapters 4 and 5, in order to synchronize the surgical tool's motion with the POI's motion, the position of both the surgical tool and the POI must be continuously measured. The position of the surgical tool can easily be measured in real-time from the robot's encoders. It is more difficult to measure the position of the POI and the proposed methods have been discussed in Sec. 2.2. Ultrasound images were chosen as they can visualize the interior of the heart while it is beating.

---

Portions of this chapter have been published in “Meaghan Bowthorpe and Mahdi Tavakoli. Physiological Organ Motion Prediction and Compensation Based on Multi-rate, Delayed, and Unregistered Measurements in Robot-assisted Surgery and Therapy. *IEEE ASME Mechatronics*, Accepted September 2015, In press.”

To date it has been assumed that the motion of the POI collected from the images can be translated into a motion trajectory for the surgical robot to follow. This was the case in the previous chapters, as the Micron Tracker measured the position of markers placed on the surgical tool and the mechanical heart simulator in millimetres in Cartesian space. As the motion was confined to a single dimension, a reference point for the mechanical heart simulator's position was chosen and the distance between this point and the mechanical cam's current position was easily measured. The surgical tool simply needed to move this distance away from its reference point, as its motion is aligned with that of the mechanical heart simulator. Then, the two would have the same motion, except for a constant offset. As a surgical task has not been attempted yet, the constant offset between the two was not a problem.

It is more difficult to translate the POI's motion into a motion trajectory for the surgical robot to follow if the POI's motion is measured from ultrasound images. Here, the POI's position would be measured in pixels. This can easily be changed into millimetres, provided the ultrasound is set to a constant depth throughout the procedure. A difficulty arises if the ultrasound probe moves during the surgical procedure. If it is stationary, a transformation between the image frame and the robot frame can be calculated. However, if the ultrasound probe moves, this transformation will need to be recalculated. Tracking the ultrasound probe and calculating this transformation may be unfeasible and computationally expensive. As we are only considering tracking in one dimension, we do not necessarily need this transformation to control the surgical tool's motion. This chapter shows how the Smith predictor configurations introduced in Chapters 4 and 5 can accomplish this. Their performance is also compared to that of a proportional controller used when the transformation between the image and robot frames of reference is known.

## 6.1 Sources of Physiological Motion

The previous chapters of this thesis have focused on motion compensation for beating-heart surgery. Another type of therapy that is affected by the physiological organ motion is radiation therapy of cancerous tissue. If the cancerous tissue is continually moving due to respiration, the dosage may not be concentrated on it and healthy tissue will be treated instead.

Currently, different techniques are employed to overcome the aforementioned challenge in radiation therapy. Shirato et al. propose to intermittently run the radiation source such that radiation is emitted only when the POI is not displaced significantly [59]. In other words, when respiratory motion causes the organ and hence, the POI to move away from a specified location, the radiation source is turned off. Bel et al. automatically reposition the patient couch to cancel the effect of respiration-induced motion in order to keep the POI stationary [60]. This continual motion, however, may be uncomfortable for the patient. If the tissue motion is in-plane with respect to the radiation source, the aperture of the source can be shifted such that its focal point moves in-plane with the tissue [61, 62]. Alternatively, the beam can be steered in three dimensions electromagnetically, but this poses a challenge in terms of the required equipment cost [63]. CyberKnife has designed a radiation therapy system which automatically repositions the radiation source in near real-time if the POI has moved, but has a very low update rate [64]. The Xsight lung tracking system is an addition to the CyberKnife that tracks lung tumors during respiration without the use of fiducial markers [65]. These methods either increase the length of the procedure, are uncomfortable for the patient, are expensive, or have a very low update rate. The robot-assisted motion compensation system presented in this chapter will not significantly increase the length of the procedure, or be uncomfortable for the patient.

## 6.2 Robot-assisted Compensation for Physiological Motion

For both beating-heart surgery and radiation therapy, robotic-assistance can greatly reduce the difficulties caused by physiological motion. By controlling the robot used by the physician for delivering the therapy or performing the surgery to move in synchrony with the physiological motion along the axis of the surgical tool, the POI can be made motionless with respect to the robot. This will allow for safer and more effective interventions and can lead to the advent of new procedures such as surgery performed on a freely beating heart or radiotherapy on the spine [25, 63]. To this end, first, the position of the POI (e.g., the cancerous tissue or the point of interest on the heart) must be measured in real-time. Computed Tomography (CT) and X-ray images are often used to locate cancerous tissue while endoscopes and ultrasound images are often used to visualize the outside and inside of the beating heart, respectively. Obtaining these measurements from images creates three main challenges in designing the above-described robot-assisted motion compensating system:

1. *Slowly sampled data from the image sensor:* As discussed previously in Chapters 4 and 5, ultrasound images can have a frame rate as low as 20 Hz. Computed Tomography has an even lower frame rate, as low as 1 Hz. Such low frame rates can lead to poor motion compensation.
2. *Delay in position data acquisition and processing from the image sensor:* As discussed in Chapters 4 and 5, without delay compensation, the robot control loop may become unstable, possibly leading to uncontrolled collisions between the robot and the POI (in the case of beating-heart surgery) or dangerously exposing healthy tissue to radiation (in the case of radiation therapy).
3. *Unregistered frames between data sources:* The POI's position measurements are taken in the image's frame of reference, whereas the robot's position, measured by the robot's encoders, is in the robot's frame of reference – see Fig. 6.1. If the

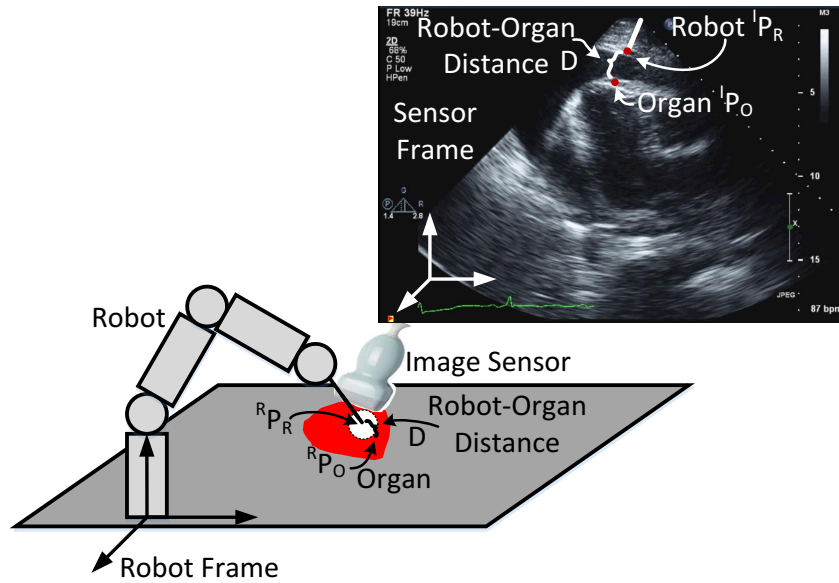


FIGURE 6.1: The robot’s position measurements will be recorded with respect to the robot frame and the sensor’s position measurements will be recorded with respect to the sensor frame.

robot is to follow the motion of the POI, the POI’s motion must be transformed into the robot frame.

Thus, the current position of the POI must be estimated from the slowly-sampled and delayed image-based measurements of the POI position. Then, a method of repositioning the robot such that it follows the summation of the POI motion and the physician-commanded motion (input through teleoperation) required for the intervention needs to be developed. Therefore, the position of the surgical tool and the target tissue or at least the distance between the surgical tool and the target tissue must be measured.

Various approaches meeting some of these requirements have been proposed for radiation therapy and beating-heart surgery. Force control, described previously in Sec. 2.2.2, is beneficial for procedures that require constant contact between the POI and the surgical tool, e.g., ablation and tissue palpation. However, force control does not account for the initial motion compensation before the surgical tool and the POI make contact. Alternatively, the surgical tool’s and POI’s positions can be controlled and the synchronization

between the surgical tool and the POI can be maintained regardless of whether or not the two are in contact. The position measurements can be obtained by three types of sensors: camera-based sensors that generally have a high frame rate, medical scanner-based sensors that generally have a low frame rate, and non-image-based sensors. These three types of measurement methods have been discussed previously in Secs. 2.2.1.1, 2.2.1.2, and 2.2.2, respectively. Medical scanners have been chosen for this work as they can visualize the interior of the heart through the opaque blood pool and can visualize cancerous tissue inside the body. In addition to the medical scanner methods referenced in 2.2.1.2, positron emission tomography (PET) and CT have been proposed for radiation therapy in [66], and [67], respectively. However, PET scanners and CT expose the patient to radiation, which is not desirable. For this reason, ultrasound images will be used once again for organ motion tracking in beating-heart surgery [30, 46, 49].

Various configurations of the surgical tool have also been presented. For example, motion compensating hand-held tools have been presented in [6] and a teleoperated system for radiation therapy has been presented in [64]. The various surgical tool configurations are discussed in more detail in Secs. 2.1.1 to 2.1.3. As in Chapters 4 and 5, teleoperated tools will be used in this chapter.

The remainder of this chapter is organized as follows. Section 6.3 describes the upsampling, prediction, and control systems. These methods are then tested experimentally in Section 6.4. A functional task where a needle removes fluid from a simulated heart is tested experimentally in Section 6.5. Finally, the concluding remarks are given in Section 6.7.

### **6.3 Control Systems**

The difficulty in using images to obtain position measurements is that the positions will be measured in the image frame, which is not aligned with the robot's frame. Consequently, the robot cannot be made to follow the POI's position as the POI's

position in the robot frame is still unknown. One possible solution is to have the POI's position measurements transformed into the robot's frame. Two approaches to designing the control system are presented in this chapter. The first, Approach 1, assumes the POI's position measurements can be transformed into the robot frame. If this is not possible, then in Approach 2, the distance between the robot and POI can be measured in the images as this distance remains the same regardless of the frame of reference. The robot-POI distance can then be controlled to follow the physician's motion.

The choice of the control system depends on the data acquired from the sensors; more specifically, whether or not the position measurements from the images can be transformed into the robot's frame of reference. If the image to robot frame transformation is available, the POI's trajectory is measured directly from the images, upsampled, and transformed into the robot's frame of reference. If the image to robot frame transformation is not available, the robot-POI distance is measured in the images and then upsampled. From this distance and the real-time measurements of the robot's position that have been delayed to match the timing of the distance measurements, the delayed position of the POI can be calculated. In both cases, the POI position is then predicted ahead to the current time. Regardless of whether the transformation between the image and the robot frames of reference is available, the controller will need to compensate for the image acquisition and processing delay incurred in extracting the slowly sampled position data.

### **6.3.1 POI Motion Upsampling**

Many of the sensors such as ultrasound or CT will capture the images at a slower rate than the typical robot control system sampling rate. To take advantage of the robot's faster sampling rate, the slowly sampled position data is upsampled. The position measurement obtained from the images is either the position of the POI if the image to robot frame transformation is available (Approach 1), or the robot-POI distance if

the sensor to robot frame transformation is not available (Approach 2). As the robot-POI distance follows the physician's motion, the shape and periodicity of this signal are unknown. On the contrary, the POI's motion will be quasi-periodic as both the heart's beating motion and respiratory motion follow a quasi-periodic trajectory. Accordingly, two upsampling methods are used in this work: cubic interpolation, which does not require a quasi-periodic input signal, and extended Kalman filter based upsampling, which does require a quasi-periodic input signal.

To begin, cubic interpolation does not require any prior knowledge about the signal and hence, it can be used to upsample either the robot-POI distance or the POI position itself. The following equations describe the cubic interpolated upsampled data points  $p(i)$ .

$$p(i) = h_{00}(i)p_0 + h_{10}(i)m_0 + h_{01}(i)p_1 + h_{11}(i)m_1 \quad (6.1)$$

$$h_{00}(i) = 2i^3 - 3i^2 + 1 \quad (6.2a)$$

$$h_{10}(i) = i^3 - 2i^2 + i \quad (6.2b)$$

$$h_{01}(i) = -2i^3 + 3i^2 \quad (6.2c)$$

$$h_{11}(i) = i^3 - i^2 \quad (6.2d)$$

where  $p_0$  and  $p_1$  are the points in between which the interpolation is occurring,  $m_0$  and  $m_1$  are the slopes at points  $p_0$  and  $p_1$ , respectively, and  $i$  is the interpolation variable and contains evenly spaced values between 0 and 1 and has a length of one greater than the number of points to be upsampled between the two slowly sampled points,  $p_0$  and  $p_1$ . As four data points are required (points  $p_0$  and  $p_1$  and a data point on either side used to calculate the slope) to ensure that the upsampled signal and its first derivative are continuous, cubic interpolation involves a processing delay of  $2n - 1$  sample times, where  $n$  is the number of samples added to the signal.

The second method, upsampling using an extended Kalman filter, does not increase

the data acquisition and processing delay, but requires a model of the input signal. Hence, the input signal must be quasi-periodic. For this reason, the image-to-robot frame transformation must be available such that the POI motion data can be extracted and fed as the input to the upsampler. The POI's motion is based on a Fourier series [30, 68].

$$y(\mathbf{x}(t)) \triangleq c + \sum_{l=1}^m r_l \sin \theta_l(t) \quad (6.3)$$

and  $\theta_l(t) = l \int_0^t \omega(\tau) d\tau + \phi_l(t)$ ,  $\mathbf{x}(t) = [c(t), r_l(t), \omega(t), \theta_l(t)]^T$ ,  $\mu(t)$  and  $v(t)$  are independent Gaussian noise terms.

The extended Kalman filter is based on the following state space model that evolves through random walk, where the offset  $c$ , the sine wave coefficients  $r_l$ , and the frequency  $\omega(t)$  remain constant between samples. Only the  $\theta_l$  values are updated according to (7.3b) in each sample time. These values are later updated by the EKF based on the error between the predicted and actual measurement, except for the frequency,  $\omega$ , which is replaced by the value measured directly from the past POI motion. The input signal has a slow sampling time of  $\Delta T$ , which is to be increased to a fast sampling time of  $\Delta t$ .

$$\mathbf{x}(t + \Delta t) = \mathbf{F}(\Delta t)\mathbf{x}(t) + \mu(t) \quad (6.4a)$$

$$z(t) = y(\mathbf{x}(t)) + v(t) \quad (6.4b)$$

where  $\mathbf{F}(\Delta t)$  is a  $[2m + 2] \times [2m + 2]$  matrix.

$$\mathbf{F}(\Delta t) = \begin{bmatrix} \mathbf{I}_{m+1} & \mathbf{0} \\ \mathbf{0} & \begin{matrix} 1 \\ \Delta t & 1 \\ 2\Delta t & 0 & 1 \\ \vdots & \ddots \\ m\Delta t & & 1 \end{matrix} \end{bmatrix} \quad (6.5)$$

Next, the extended Kalman filter is updated every time step with the following equations:

$$\mathbf{P}(t + \Delta t|t) = \mathbf{F}(\Delta t)\mathbf{P}(t|t)\mathbf{F}(\Delta t)^T + \mathbf{Q} \quad (6.6a)$$

$$S = \sigma_R^2 + \mathbf{H}(\Delta t)\mathbf{P}(t + \Delta t|t)\mathbf{H}(\Delta t)^T \quad (6.6b)$$

$$\mathbf{K}(t) = \mathbf{P}(t + \Delta t|t)\mathbf{H}(\Delta t)^T S^{-1} \quad (6.6c)$$

The estimated covariance matrix  $\mathbf{P}(t + \Delta t|t)$  is a  $[2m + 2] \times [2m + 2]$  diagonal matrix with  $[0.001, 0.1/1, 0.1/2, \dots, 0.1/l, 0.1, 0.2_{1 \times m}]$  along the diagonal, the process noise covariance matrix  $\mathbf{Q}$  is a  $[2m + 2] \times [2m + 2]$  diagonal matrix with 0.0001 along the diagonal, and the observation noise covariance matrix  $\sigma_R^2$  is 0.01.  $\mathbf{H}(\Delta t)$  is a  $[2m + 2] \times [1]$  matrix.

$$\mathbf{H}^T(\Delta t) = \left( \frac{\partial y}{\partial \mathbf{x}} \right)^T \bigg|_{\hat{\mathbf{x}}(t+\Delta t|t) = \mathbf{F}\hat{\mathbf{x}}(t|t)} = \begin{bmatrix} 1 \\ \sin \hat{\theta}_1(t + \Delta t|t) \\ \vdots \\ \sin \hat{\theta}_m(t + \Delta t|t) \\ \hat{r}_1(t + \Delta t|t) \cos \hat{\theta}_1(t + \Delta t|t) \\ \vdots \\ \hat{r}_m(t + \Delta t|t) \cos \hat{\theta}_m(t + \Delta t|t) \end{bmatrix} \quad (6.7a)$$

where the  $\hat{\phantom{x}}$  symbol denotes the estimated value.

As the extended Kalman filter is used to upsample the slowly sampled signal  $y$ , with a sampling time of  $\Delta T$ , a new position measurement  $z(t + \Delta t)$  is only available when  $\Delta t$  is a multiple of  $\Delta T$ . In this case, the estimated covariance matrix  $\mathbf{P}$  and the state matrix  $\mathbf{x}$  are updated as:

$$\hat{\mathbf{x}}(t + \Delta t|t + \Delta t) = \mathbf{F}(\Delta t)\hat{\mathbf{x}}(t|t) + \mathbf{K}(t)(z(t + \Delta t) - y(\mathbf{F}(\Delta t)\hat{\mathbf{x}}(t|t))) \quad (6.8a)$$

$$\mathbf{P}(t + \Delta t|t + \Delta t) = (\mathbf{I} - \mathbf{K}(t)\mathbf{H}(\Delta t))\mathbf{P}(t + \Delta t|t) \quad (6.8b)$$

When a new position measurement is not available, the estimated covariance matrix  $\mathbf{P}$  and the state matrix  $\mathbf{x}$  are not updated, but simply propagated ahead one time step as:

$$\hat{\mathbf{x}}(t + \Delta t|t + \Delta t) = \mathbf{F}(\Delta t)\hat{\mathbf{x}}(t|t) \quad (6.9a)$$

$$\mathbf{P}(t + \Delta t|t + \Delta t) = \mathbf{P}(t + \Delta t|t) \quad (6.9b)$$

### 6.3.2 POI Motion Prediction

Once the position data has been upsampled, the POI's position is predicted ahead to the current time to overcome the image acquisition and processing delay inherent in image-based POI motion tracking. The POI's motion is either measured from the image directly when the image to robot frame transformation is available, or by subtracting the robot-POI distance from the robot's position. Either way, there is delay in the POI motion tracking. Two methods are used in this work for POI motion prediction and both take advantage of the POI motion's periodicity. The first is to simply use the POI's motion from the last heart beat or respiratory cycle. In this case, the length of the heart beat or respiratory cycle is predetermined and the current POI position is estimated by the corresponding POI position in the previous motion cycle. This method assumes that the respiration rate or the heart beat rate does not change. The second is to use an extended Kalman filter. This method allows for a changing respiratory or heart rate and changing amplitude in the motion signal. Here, the signal's state matrix  $\mathbf{x}$  and

the estimated covariance matrix  $\mathbf{P}$  are updated every time step as the measurement signal has previously been upsampled. To predict future points, the state matrix  $\mathbf{x}$  is multiplied  $j$  times by the update matrix  $\mathbf{F}$  to move  $j$  steps ahead:

$$\hat{\mathbf{x}}(t + j\Delta t | t + \Delta t) = \mathbf{F}(\Delta t)^j \hat{\mathbf{x}}(t + \Delta t | t) \quad (6.10)$$

### 6.3.3 Robot Predictive Feedback Control

When choosing the feedback control structure, two approaches have been taken in this chapter. The first uses position measurements and compensates for the delay by predicting the current POI position rather than compensating for the delay within the feedback loop, whereas the second uses distance measurements and compensates for the delay within the feedback loop. In both cases, motion compensation is performed along one dimension – the axis of the surgical tool. Let us denote the POI position by  $P_H$ , and the physician’s position by  $P_S$ , the robot’s position by  $P_R$ , and the robot-POI distance by  $D_{RH} = P_R - P_H$ . Both continuous signals (e.g., actual POI motion) and discrete-time signals (e.g., measured POI motion) are present within the feedback loop. The continuous time signals are shown with straight lines and the discrete time signals are shown with dotted lines where the distance between the dots is proportional to the sample time, i.e., shorter sample times are shown by dots that are closer together. When referring to a specific variable, say  $X$ , let us denote the continuous time signal by  $X$ , the slowly-sampled signal by  $X'$ , the fast-sampled signal by  $X''$ , the delayed and slowly-sampled signal by  $\bar{X}'$ , the delayed and fast-sampled signal by  $\bar{X}''$ , and the prediction of  $X''$  from  $\bar{X}''$  by  $\hat{X}$ . Also, let us denote the transformation from the image to the robot frame as  ${}^R_I T$ , a variable measured in the robot frame as  ${}^R X$ , and a variable measured in the image frame as  ${}^I X$ . Consequently, if the transformation from the image to the robot frame is known, the equivalent point in the robot frame can be calculated as  ${}^R X = {}^R_I T {}^I X$ .

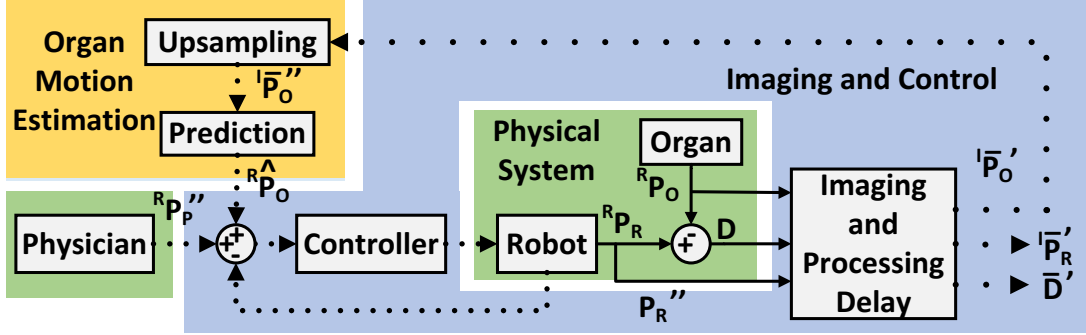


FIGURE 6.2: A simple feedback controller for teleoperated motion compensation. Here, the setpoint for the robot’s position,  ${}^R P_R''$  is the combination of the physician’s position,  ${}^R P_S''$ , and the estimated current POI position  ${}^R \hat{P}_O$ .

### 6.3.3.1 Approach 1

In the first approach, the image to robot frame transformation is available and both the delayed position of the robot,  ${}^I \bar{P}_R'$ , and the delayed position of the POI,  ${}^I \bar{P}_O'$ , are measured in the images. Here, the real-time position of the robot,  ${}^R P_R''$ , measured from the robot encoders is controlled to follow the combination of the physician’s motion,  ${}^R P_S''$ , and the estimated POI motion,  ${}^R \hat{P}_O$ . As the robot’s position,  ${}^R P_R''$ , is measured from the robot’s encoders and is not delayed, a regular (non-predictive) feedback controller shown in Fig. 6.2 is used. Note that, the position of the POI,  ${}^I \bar{P}_O'$ , is measured with a data acquisition delay in the image frame at the slow sampling rate. This can be transformed to the robot frame, upsampled to the robot’s control rate, and predicted ahead to the current time to obtain  ${}^R \hat{P}_O$ . The transfer function of this controller is

$${}^R P_R'' = \frac{({}^R P_S'' + {}^R \hat{P}_O)CG}{1 + CG} \quad (6.11)$$

This first method requires the transformation between the image and robot frame,  ${}^R T_I$ . However, this transformation may be difficult or infeasible to calculate. For instance, if the position of the sensor (e.g., a hand-held ultrasound probe) changes during the procedure, the image to robot frame transformation will need to be recalculated every sample time, assuming that the ultrasound probe position and orientation can always

be tracked. It may become computationally expensive to continually update the frame-to-frame transformation. Also, depending on the configuration of the operating room, measuring the position and orientation of the imaging sensor may be unfeasible.

### 6.3.3.2 Approach 2

In cases where the image to robot transformation is unavailable, it makes sense to instead rely on the robot-POI distance measured along the surgical tool's axis,  $D_{RH}$ , because this measurement will be the same in any reference frame, i.e.  ${}^I D_{RH} = {}^R D_{RH}$ . This means, the imaging sensor is free to move during the intervention and its position and orientation does not need to be tracked. Note that in this case, either the robot's real-time position,  ${}^R P_R''$ , or the robot's mathematical input-output model (for estimating the position based on the input control signal) must be known. This is because the position of the POI,  ${}^R \hat{P}_O''$  will later need to be calculated based on the position of the robot and the measured robot-POI distance. It is important to determine the POI's position as, unlike the robot-POI distance, it is the only quasi-periodic signal available whose current value can be estimated based on delayed measurements using predictive filters.

When the image to robot frame transformation is not available, the robot-POI distance will be controlled to follow the physician's motion. The difficulty is that the distance measurement is slowly sampled and delayed ( $\bar{D}'_{RH}$ ). Cubic interpolation can be used to upsample the signal to  $\bar{D}''_{RH}$ , but as the distance signal is not periodic it cannot easily be predicted forward to overcome the delay. Hence, the delay must be compensated for by the controller. In this configuration, the POI's motion acts as a disturbance. Because it is periodic, the POI motion can be predicted and added to the feedback loop. First, the delayed position of the POI can be found by delaying the robot's position and subtracting it from the upsampled distance measurement,  ${}^R \hat{\bar{P}}_O'' = {}^R \bar{P}_R'' - \bar{D}''_{RH}$ . Now, both the robot's position  ${}^R P_R''$  and an estimate of the delayed POI's position  $\bar{P}_O''$  are known. With this data, a Smith predictor is used in the feedback control loop to

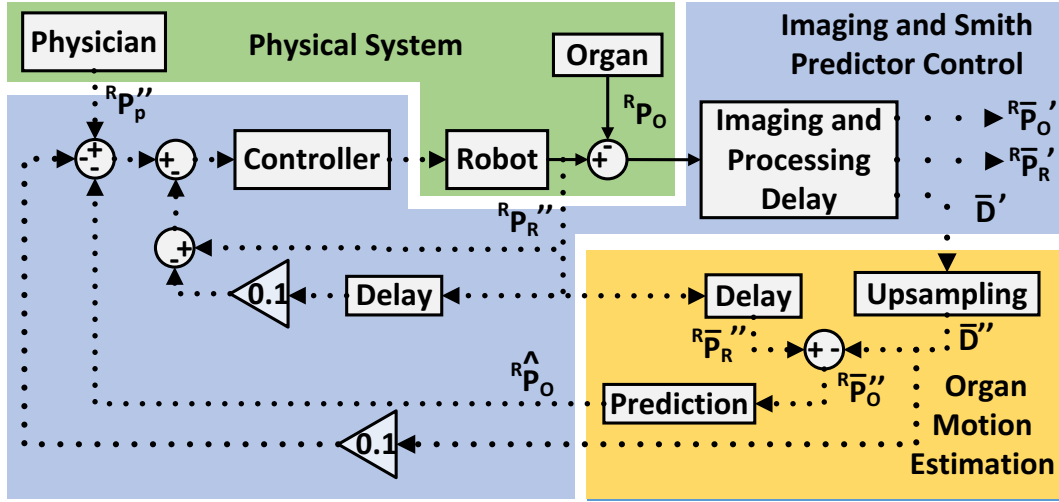


FIGURE 6.3: A Smith predictor feedback controller for teleoperated motion compensation when the output is delayed. Here, the setpoint for the robot-POI distance,  $D_{RH}$ , is the combination of the physician’s position,  $R P_S''$ , and the estimated current POI position  $\hat{P}_O$ .

effectively remove the time delay from within the feedback loop [46, 52]. A detailed description of the development of the Smith predictor is given in Chapter 4.

Two different configurations of the Smith predictor, shown in Figs. 6.3 and 6.4 are tested. In both cases, the current motion of the POI,  $P_H$ , affects the loop as an external disturbance. To cancel the effect of this disturbance, the predicted POI position,  $R \hat{P}_O''$ , is incorporated into the control system. The point at which the estimated POI position is added into the control loop is the main difference between the two Smith predictor configurations. In the first case, it is added to the surgeon’s position to form a new setpoint – see Fig. 6.3. This configuration was previously presented in Chapter 4. In the second case, it is added to the inner feedback loop to mimic where the disturbance is added to the robot’s motion to create the estimated real-time distance signal – see Fig. 6.4. This configuration was previously presented in Chapter 5. The possible upsampling and prediction methods for each approach are listed in Table 6.1.

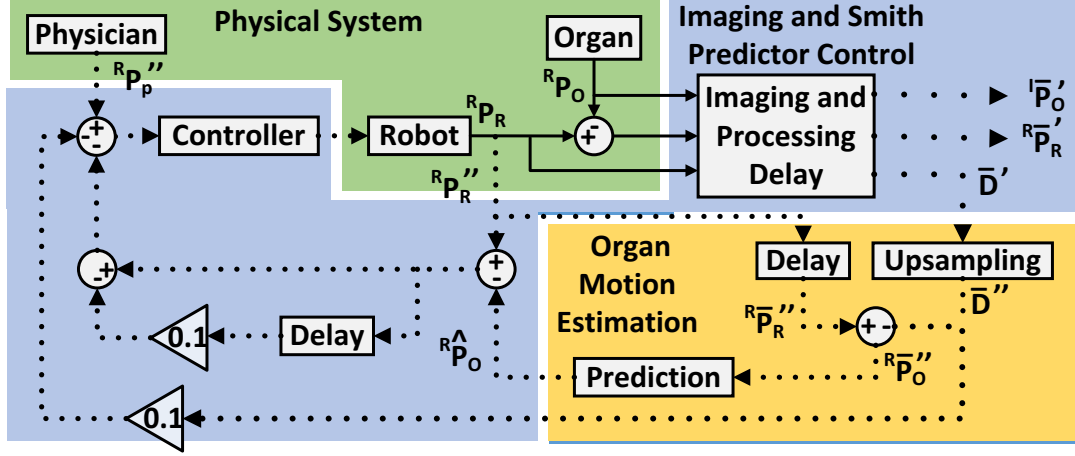


FIGURE 6.4: A Smith predictor feedback controller for teleoperated motion compensation when the output is delayed. Here, the setpoint for the robot-POI distance,  $D_{RH}$ , is the physician's position,  ${}^R P_S''$ . The estimated current POI position  $\hat{P}_O$  is added into the inner feedback loop to cancel the effect of the disturbance caused by the POI's motion.

To calculate the transfer function of the first Smith predictor configuration, an expression for  $\bar{D}'_{RH}$  is found:

$$(P_S'' - \bar{D}'_{RH} - ((P_R'' - \hat{P}_O) - P_R'' z^{-k})CG - P_H)z^{-k} = \bar{D}'_{RH} \quad (6.12)$$

where  $z^{-k}$  represents the time delay,  $C$  is the controller, and  $G$  is the robot. Assuming  $(P_R'' - \hat{P}_O) = D'_{RH}$ , (6.12) simplifies to

$$((P_S'' - \bar{D}'_{RH} + P_S'' z^{-k}CG) - P_H)z^{-k} = \bar{D}'_{RH} \quad (6.13)$$

In this case,  $\bar{D}'_{RH}$  is approximated by  $P_S'' z^{-k}$ , which is not ideal. Assuming  $D''_{RH} z^{-k}$  is equivalent to  $\bar{D}'_{RH}$ , (6.13) can be written as:

$$\bar{D}'_{RH} = \frac{P_S'' CG - P_H}{1 + CG} z^{-k} \quad (6.14)$$

	Upsampling Method	Prediction Method
Approach 1	CI or EKF	PM or EKF
Approach 2	CI	PM or EKF

TABLE 6.1: The possible upsampling and prediction methods for each approach. CI: cubic interpolation, EKF: extended Kalman filter based upsampling or prediction, PM: previous motion.

To calculate the transfer function of the second Smith predictor configuration, an expression for  $\bar{D}'_{RH}$  is found:

$$(P''_S - \bar{D}''_{RH} - ((P''_R - \hat{P}_O) - (P''_R - \hat{P}_O)z^{-k})CG - P_H)z^{-k} = \bar{D}'_{RH} \quad (6.15)$$

Assuming  $(P''_R - \hat{P}_O)z^{-k} = \bar{D}''_{RH}$  and  $P''_R - \hat{P}_O = D''_{RH}$ , (6.15) simplifies to

$$((P''_S - D''_{RH}CG) - P_H)z^{-k} = \bar{D}'_{RH} \quad (6.16)$$

Assuming  $D''_{RH}z^{-k}$  is equivalent to  $\bar{D}''_{RH}$ , (6.16) can be written as:

$$\bar{D}'_{RH} = \frac{P''_S CG - P_H}{1 + CG} z^{-k} \quad (6.17)$$

## 6.4 Experimental Results

Each of the controllers, prediction, and upsampling methods were tested experimentally. A Micron Tracker (HX60 from Claron Technology Inc., Toronto, ON, Canada) was used as the image sensor. It has a low frame rate of 20 Hz and a delay of approximately 105 ms in acquiring and storing each frame. A custom-built mechanical cam generated the POI motion. The motion trajectory was collected from the movement of a point on the side wall of the heart in a series of clinical ultrasound images of a patient's beating heart. A single degree-of-freedom (DOF) robot was used and is actuated by a voice coil motor (NCC20-18-020-1X from H2W Technologies Inc., Santa Clarita, CA, USA). To verify the results, real-time position measurements of both the POI and the robot were collected

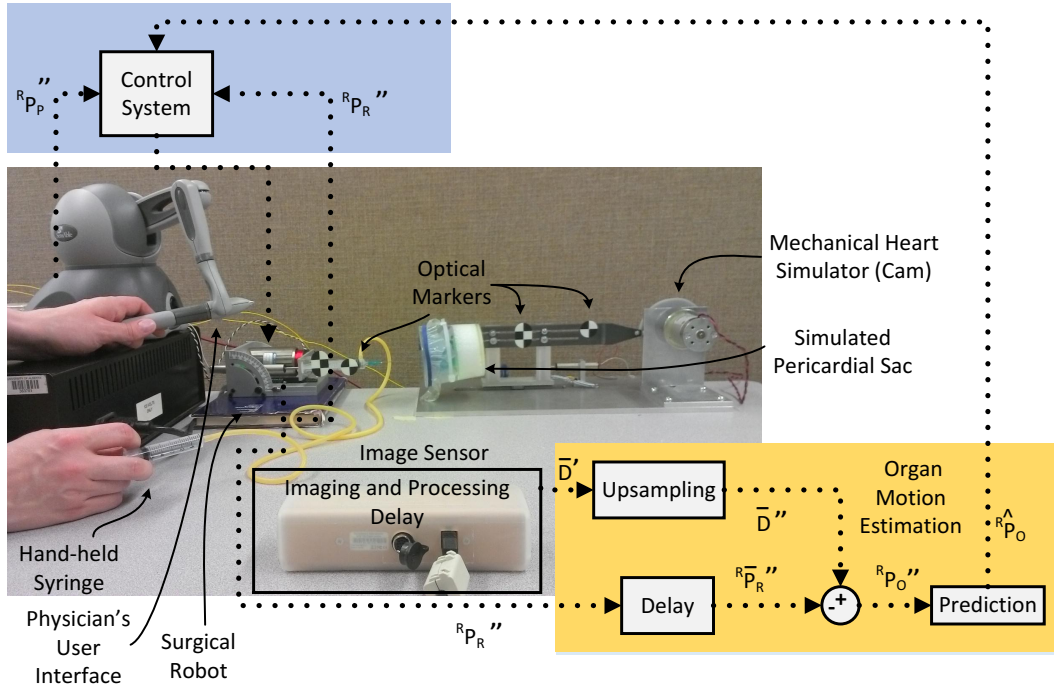


FIGURE 6.5: The experimental setup, which includes a mechanical cam that emulates the POI's motion, the image sensor and its optical markers, the physician's user interface, the surgical tool attached to the robot, and the hand-held syringe used for the functional task.

from two potentiometers (LP-75FP-5K and LP-30FP-1K from Midori America Corp., Fullerton, CA, USA); the real-time position of the POI is used for robot-POI tracking error calculations only and was not used as a measurement available to the controllers.

For each trial, a cyclic motion with a peak-to-peak amplitude of 10 mm and a period of 63 bpm (0.81 Hz) which is increase to 66 bpm (1.10 Hz) at  $t = 10s$  is used. This motion is similar to that encountered when a surgeon punctures the pericardial sac to drain the excess fluid. Here, the surgeon must puncture the pericardial sac that is approximately 5-10 mm from the exterior heart wall, keep the needle in the pericardial sac long enough to insert a guide-wire without puncturing a coronary artery on the heart wall. This procedure is described further in the following section. Three error metrics are calculated for each trial: the mean absolute error (MAE) is  $\frac{\sum |error|}{j}$ , where  $j$  is the number of data points in the sample, the integral squared error (ISE) is  $\frac{\sum (error)^2}{j}$ , and

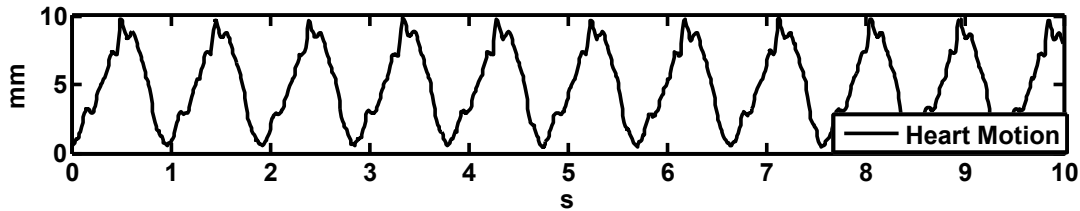


FIGURE 6.6: The simulated heart motion.

the peak error is the largest error at a single point in time. The results from each of the trials are summarized in Table 6.2.

The same parameters were used for the extended Kalman filter and upsampling in each trial. To find the initial state  $\mathbf{x}(0)$ , spectral analysis was performed on the mechanical cam's motion. The amplitude, frequency, and number of harmonics were calculated from the Fourier transformation of the mechanical cam's motion. The estimated covariance matrix,  $\mathbf{P}(0)$  is initialized to a diagonal matrix with the following values along the diagonal  $[0.001, 0.1_{1 \times m}, 0.1, 0.2_{1 \times m}]$  where  $m$  is the number of harmonics, the process noise covariance matrix  $\mathbf{Q}$  is initialized to a diagonal matrix with a value of 0.0001, and the observation noise covariance matrix  $\sigma_R^2$  is initialized to 0.01. The Micron Tracker supplied image measurements at a rate of 20 Hz or every 50 ms. The robot measurements were collected at a rate of 100 Hz or every 10 ms. To control the robot at the faster rate, four measurements were added via upsampling between measurements of the slowly sampled position signals.

In this work, the following hypotheses are tested.

*Hypothesis 1:* Predicting and upsampling the POI's motion using an EKF will perform better than using the POI's motion in the last cycle or upsampling using cubic interpolation, because the EKF can adapt to changes in the motion's period and amplitude.

*Hypothesis 2:* For the case when the transformation between the image frame and the robot frame is not available, the second Smith predictor will perform better than the first as the disturbance created by the POI motion is compensated for by the second Smith predictor.

The results of the trials are summarized in Table 6.2.

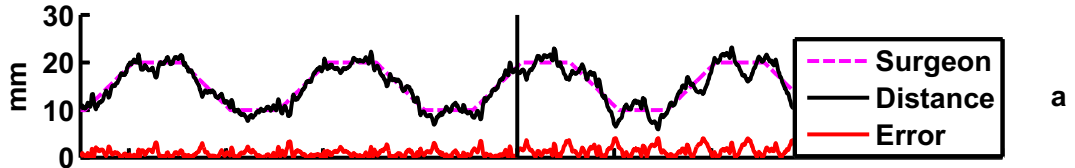
### 6.4.1 Approach 1

To begin, the simplest case, where the frame transformation from the image to the robot frame is available, is tested. In this case, a simple proportional controller with a gain of 0.2 is used – see Fig. 6.2. The result of each combination of prediction and upsampling method are given in Fig. 6.7. It can be seen from Fig. 6.7a and b that using the previous POI positions to predict future POI positions does not take cyclic rate changes into account as the error increases when the heart rate is increased. In this case, the MAE is 1.23 mm, the ISE is 2.39 mm<sup>2</sup>, and the peak error is 4.34 mm when cubic interpolation is used for upsampling in Fig. 6.7a. The MAE is 1.07 mm, the ISE is 1.99 mm<sup>2</sup>, and the peak error is 5.44 mm when extended Kalman filter based upsampling is used in Fig. 6.7b. When an extended Kalman filter is used for prediction in Fig. 6.7c and d, the cyclic rate change does not affect the error, which remains similar throughout the trial. The MAE is 1.14 mm, the ISE is 2.13 mm<sup>2</sup>, and the peak error is 4.38 mm when cubic interpolation is used for upsampling in Fig. 6.7c. The MAE is 0.99 mm, the ISE is 1.51 mm<sup>2</sup>, and the peak error is 3.62 mm when extended Kalman filter based upsampling is used in Fig. 6.7d. Because, the coefficients of the model (6.10) used by the extended Kalman filter can change with time, prediction based on the extended Kalman filter performed better than using the past heart motion. Also, upsampling based on an extended Kalman filter performed slightly better than upsampling with cubic interpolation.

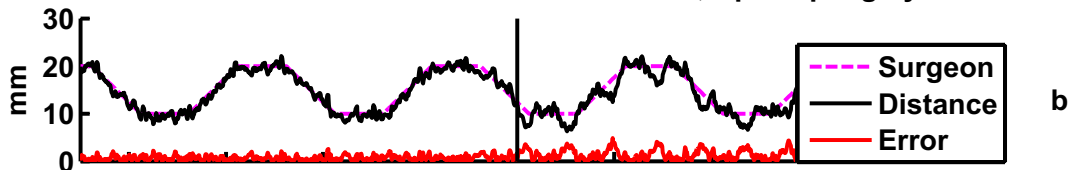
### 6.4.2 Approach 2

It is usually difficult to obtain the image frame to robot frame transformation as the position and orientation of the image sensor must be continually tracked in real-time and the frame transformation continually updated. This may become computationally

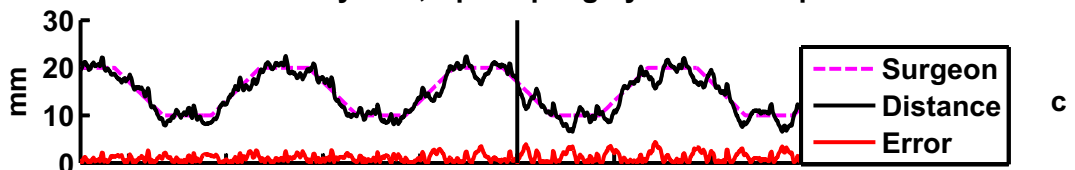
Prediction Based on Previous POI Positions, Upsampling by Cubic Interpolation



Prediction Based on Previous POI Positions, Upsampling by EKF



Prediction by EKF, Upsampling by Cubic Interpolation



Prediction by EKF, Upsampling by Another EKF

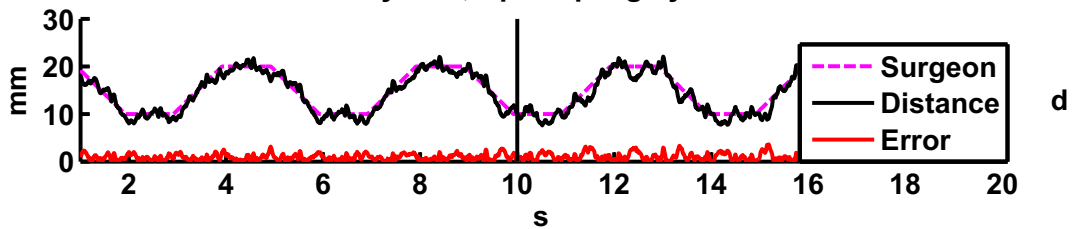


FIGURE 6.7: The tracking result of using proportional control when the transformation from the image to the robot frame is available. The dashed pink line is the physician’s motion, the solid black line is the real-time distance between the surgical tool tip and the POI, and the solid red line is the error between the surgeon’s motion and the real-time robot-POI distance. The vertical line denotes the time at which the heart rate increases.

expensive. In addition, it may be difficult to track the position and orientation of the image sensor. In this case, the delay must be compensated for within the control loop.

Here, a Smith predictor is used to compensate for the delayed distance measurements. Initially, the first Smith predictor (Fig. 6.3) is used where the predicted POI motion is added to the reference signal to counteract the effect of the disturbance, which is the POI's motion. As only the distance between the surgical tool tip and the POI is available, the delayed motion of the POI needs to be calculated. First, the robot-POI distance is upsampled. Only cubic interpolation and not an extended Kalman filter can be used in this scenario as the extended Kalman filter requires a quasi-periodic signal. Next, the motion of the robot is measured in real-time in the robot-frame. These measurements are delayed by the length of the data acquisition and processing delay of the sensor and then the robot-POI distance is subtracted. This leaves the delayed position of the POI,  ${}^R\bar{P}_O''$ . As the distance data was previously upsampled, the POI measurements only need to be predicted.

The results are given in Fig. 6.8. The MAE, ISE, and peak errors are 4.46 mm, 11.3 mm<sup>2</sup>, and 24.8 mm respectively when the last heart beat is used to predict the current heart motion shown in Fig. 6.8a. The MAE, ISE, and peak errors are 4.45 mm, 22.7 mm<sup>2</sup>, and 9.39 mm respectively when EKF based prediction is used to predict the current heart motion shown in Fig. 6.8b. It is clear from Fig. 6.8b that using an extended Kalman filter to predict the motion of the POI gives a better result than using the previous cycle of motion of the POI when the rate of the POI's motion is changing.

Then, the second Smith predictor is tested. As the predicted POI's motion is added to the inner feedback loop to account more directly for the disturbance the POI's motion adds to the output (the distance between the surgical tool and the POI), it is expected to give a better result than the previous case. Once again, cubic interpolation must be used to upsample the distance data as was previously discussed. The results are given in Fig. 6.9. The MAE, ISE, and peak errors are 3.10 mm, 13.3 mm<sup>2</sup>, and 8.29 mm respectively when the last heart beat is used to predict the current heart motion shown

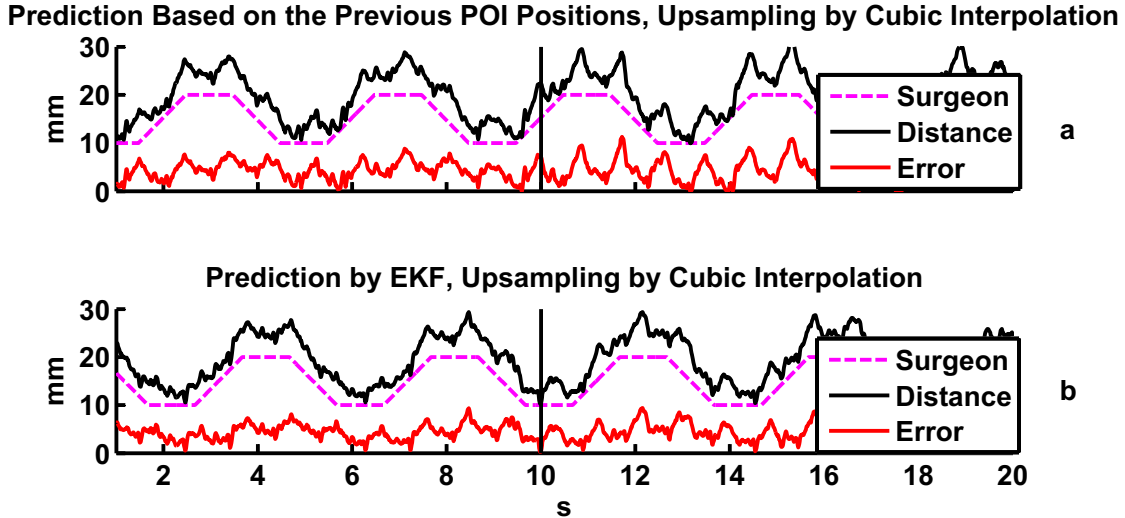
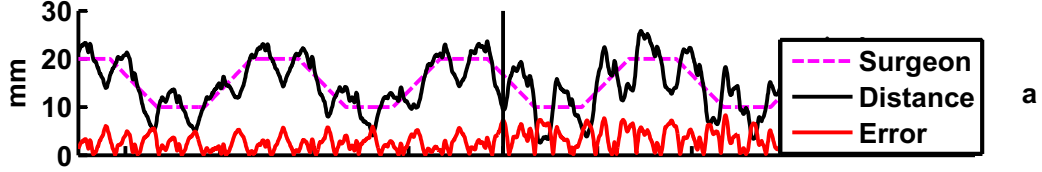


FIGURE 6.8: The tracking result of using Smith predictor method I when the transformation between the sensor frame and robot frame is not available. The dashed pink line is the surgeon’s motion, the solid black line is the real-time distance between the surgical tool tip and the POI, and the solid red line is the error between the surgeon’s motion and the real-time distance between the surgical tool tip and the POI. The vertical line denotes the time at which the heart rate increases.

in Fig. 6.8a. The MAE, ISE, and peak errors are 1.92 mm, 5.94 mm<sup>2</sup>, and 8.36 mm respectively when EKF based prediction is used to predict the current heart motion shown in Fig. 6.9b. It is again clear from Fig. 6.9b that using an extended Kalman filter to predict the motion of the POI gives a better result than using the previous motion of the POI when the rate of the POI’s motion is changing. As expected, because the estimated POI motion is subtracted from the robot’s position in the inner feedback loop in the same manner as it is subtracted from the robot’s actual position in real-time, the second Smith predictor configuration performs better than the first.

Finally, as a comparison, a Smith predictor can also be used when the frame transformation is available. In this case, the current POI motion is estimated directly from the POI motion measurements,  $\bar{P}'_{\mathcal{O}}$ . As the second Smith predictor configuration performed better than the first, only the second configuration was used during this test. The results are given in Fig. 6.10 where cubic interpolation is used, and only EKF based prediction is used as it consistently outperformed predicting the current POI motion based on

**Prediction Based on the Previous POI Positions, Upsampling by Cubic Interpolation**



**Prediction by EKF, Upsampling by Cubic Interpolation**

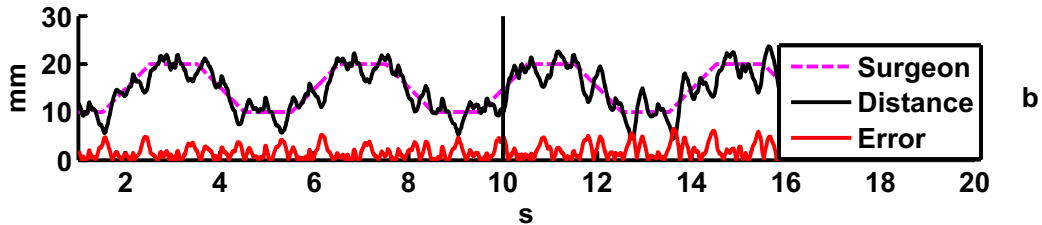


FIGURE 6.9: The tracking result of using Smith predictor method II when the transformation between the sensor frame and robot frame is not available. The dashed pink line is the surgeon’s motion, the solid black line is the real-time distance between the surgical tool tip and the POI, and the solid red line is the error between the surgeon’s motion and the real-time distance between the surgical tool tip and the POI. The vertical line denotes the time at which the heart rate increases.

previous motion. The MAE, ISE, and peak error is 1.65 mm, 4.39 mm<sup>2</sup>, and 6.28 mm, respectively as shown in Fig. 6.10a.

In all cases, the motion and delay compensation controllers maintained stability despite the delays. Most of the mean tracking errors were reduced to less than 2 mm when the heart moves approximately 10 mm as shown in the summary given in Table 6.2. The results consistently show that extended Kalman filter based prediction and upsampling where possible, performs better than the other methods – proving *Hypothesis 1*.

The proportional controller of Fig. 6.2 performed better than the two Smith predictor based controllers. However, this is an unfair comparison as these controllers are used in different situations. If the image frame to robot frame transformation is available, more direct measurements can be taken and, as expected, this case had the best performance. When the image frame to robot frame transformation is not available, the second Smith predictor configuration of Fig. 6.4 outperformed the first of Fig. 6.3 – proving *Hypothesis 2*. Depending on the availability of the image frame to robot frame transformation, both

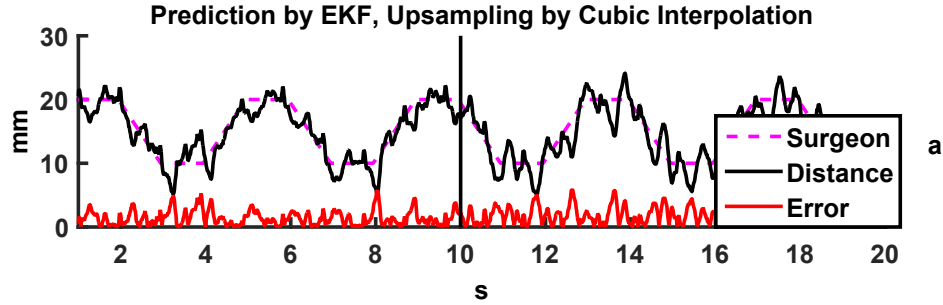


FIGURE 6.10: The tracking result of using Smith predictor method II when the transformation between the sensor frame and robot frame is available. The dashed pink line in is the surgeon’s motion. The solid black line is the real-time distance between the surgical tool tip and the POI. The solid red line is the error between the surgeon’s motion and the real-time distance between the surgical tool tip and the POI.

Controller Type	Upsampling and Prediction	MAE (mm)	ISE (mm <sup>2</sup> )	Peak Error (mm)
Proportional	CI and PM	1.23	2.39	4.34
Proportional	EKF and PM	1.07	1.99	5.44
Proportional	CI and EKF	1.14	2.13	4.38
Proportional	EKF and EKF	0.99	1.51	3.62
SP I	CI and PM	4.46	24.8	11.3
SP I	CI and EKF	4.45	22.7	9.39
SP II	CI and PM	3.10	13.3	8.36
SP II	CI and EKF	1.92	5.94	8.36
SP II F	CI and EKF	1.65	4.39	6.28

TABLE 6.2: A summary of the experimental results. Three separate controllers were tested: the control scheme of Fig. 6.2 (Proportional), and the two Smith predictor control schemes of Fig. 6.3 (SP I) and Fig. 6.4 (SP II). The final case also uses the Smith predictor of Fig. 6.4 (SP II F), but in this case it is assumed that the image to robot frame transformation is available and the POI’s motion is measured directly from the images. The two upsampling methods include cubic interpolation (CI) and extended Kalman filter based (EKF) and the two prediction methods include previous motion (PM) and EKF based (EKF).

the proportional controller of Fig. 6.2 and the second Smith predictor configuration of Fig. 6.4 provide satisfactory performance. Both have small position tracking errors, maintain the system’s stability despite the image acquisition and processing delay, and can handle a changing rate of the POI’s motion.

## 6.5 Functional Task

To test the performance of the motion compensating robotic system, a functional task is considered. This task simulates draining fluid from a patient with a pericardial effusion, which is a build-up of fluid within the pericardial sac. As the pericardial sac is stiff and does not expand when filled with excess fluid, the excess fluid puts pressure on the heart causing it to beat abnormally. This condition can leave the patient short of breath. To drain the excess fluid and relieve the pressure, a needle is inserted through the patient's chest wall and into the pericardial sac. A guide wire is then inserted through the needle, the needle is withdrawn, and a drainage tube is inserted over the guide wire. The difficulty in performing this procedure is to puncture the pericardial sac without puncturing a coronary artery, as this would require immediate surgery. More details are provided in Sec. 3.1.1.

To simulate this functional task, a small cylindrical container is placed within a larger one. The smaller container is filled with coloured water (simulating blood in a blood vessel) and is covered by a latex membrane. The larger container is filled with clear water (simulating the excess fluid to be drained from the pericardial sac) and is also covered by a latex membrane. There is a 5 mm gap between the two membranes. This set of two containers is mounted on the mechanical cam and moves in a similar manner as a point on the heart surface. The goal of this task is to puncture the outer membrane with a needle attached to the surgical robot and withdraw 1 ml of clear fluid. Since the inner membrane represents the coronary blood vessel, if it is punctured the coloured fluid will be withdrawn and the test will be considered a failure.

Three tests to extract the fluid are performed. First, there is no motion compensation; rather, the robot follows the surgeon's motions only. The result is shown in Fig. 6.11, where the dotted line is the POI's motion, the dash-dotted line is the surgeon's motion and the solid line is the robot's motion. As the surgeon must manually compensate for the heart's motion while extracting the fluid, the tracking of the heart's motion is poor and the coloured fluid is extracted meaning the needle would have punctured the

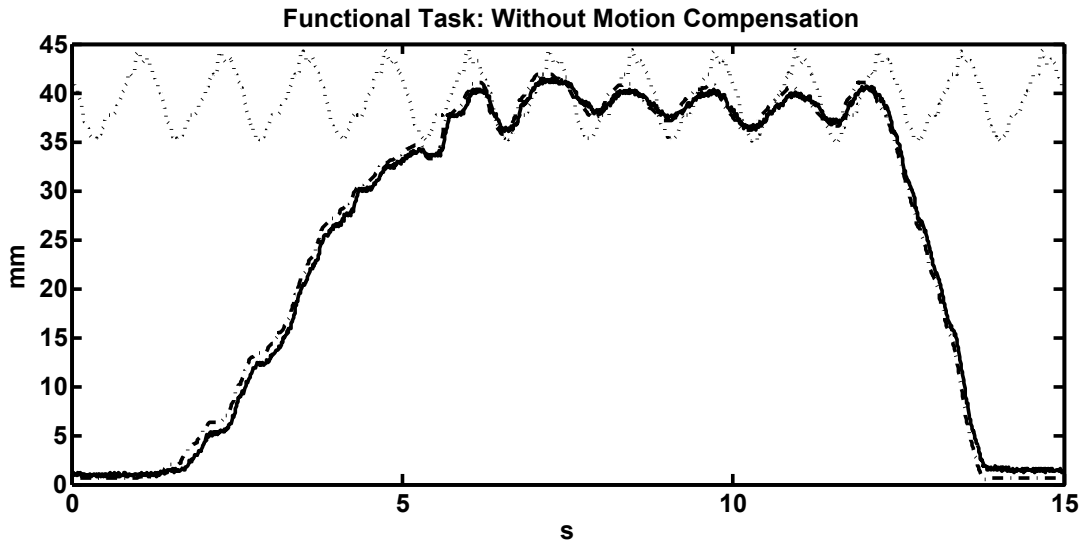


FIGURE 6.11: The tracking result of the functional task when motion compensation is not provided. Here, the dotted line is the motion of the POI, the solid line is the motion of the robot, and the dash-dotted line is the motion of the surgeon. The shapes of the two curves do not match. It is very difficult for the surgeon to control the back and forth motion of the robot from the user interface quickly enough to match the motion of the POI while also performing the surgical task.

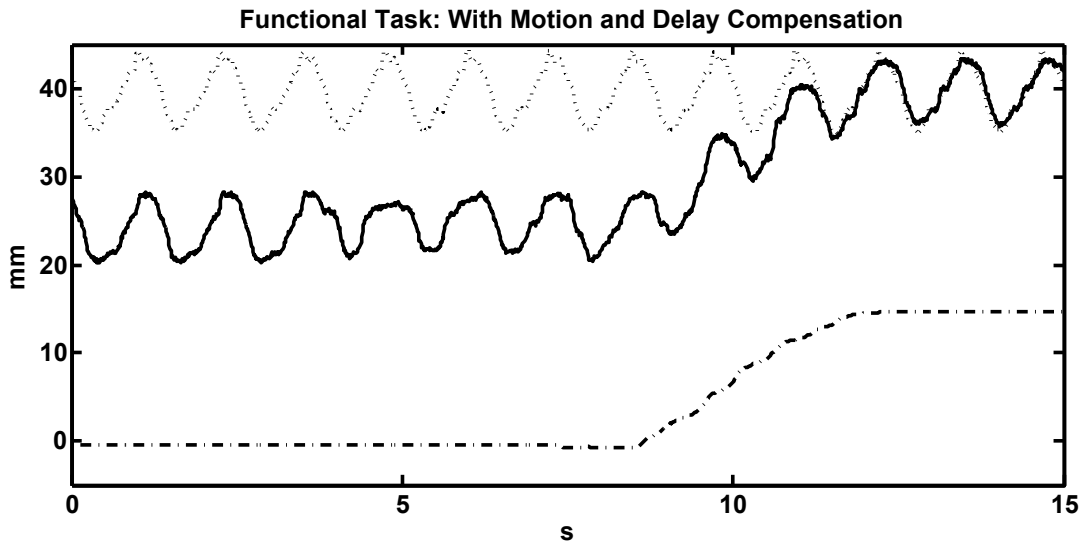


FIGURE 6.12: The tracking result of the functional task when motion compensation is provided. Here, the dotted line is the motion of the POI, the solid line is the motion of the robot, and the dash-dotted line is the motion of the surgeon. The shapes of the two motion curves are similar except for the surgeon's purposeful motions that move the robot close to the heart to withdraw fluid at 9 s.

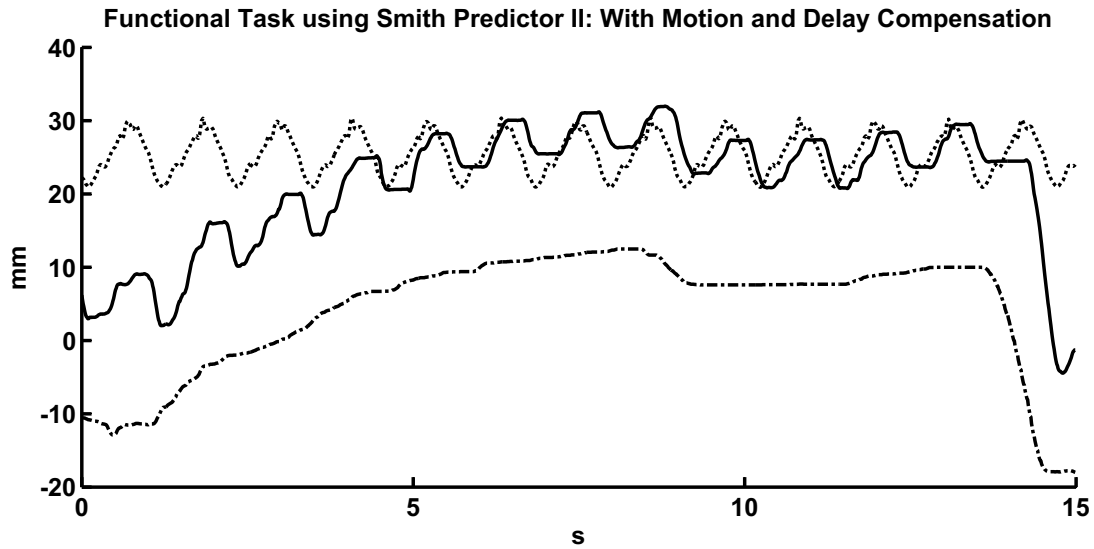


FIGURE 6.13: The tracking result of the functional task when motion compensation is provided by the second Smith predictor. Here, the dotted line is the motion of the POI, the solid line is the motion of the robot, and the dash-dotted line is the motion of the surgeon. The shapes of the two motion curves are similar except for the surgeon's purposeful motions that move the robot close to the heart to withdraw fluid.

heart if this were an actual procedure. Next, motion compensation is provided using the control scheme of Fig. 6.2. The result is shown in Fig. 6.12, where the dotted line is the POI's motion, the dash-dotted line is the surgeon's motion and the solid line is the robot's motion. Here, the surgeon only needs to move the robot towards the POI to set the desired position for the extracting the fluid. The robot follows both the surgeon's and the POI's motion. The tracking result is significantly better in this case and only the clear fluid is extracted. Finally, the motion compensation is provided by the second Smith predictor method. The results are shown in Fig 6.13, where the dotted line is the POI's motion, the dash-dotted line is the surgeon's motion and the solid line is the robot's motion. Once again, the surgeon only needs to move the robot towards the POI to set the desired position for the extracting the fluid. The robot follows both the surgeon's and the POI's motion and only the clear fluid is extracted.

## 6.6 Discussion

The results presented in this work are for a more challenging case compared to the previous literature. In this work, the POI motion data was first upsampled and predicted ahead to compensate for the image acquisition and processing delays. These delays were approximately 180 ms. The errors reported for POI motion of 10 mm have average values of approximately 0.99 mm to 1.59 mm and peak values of approximately 3.62 mm to 5.90 mm for the best cases when a proportional controller and a Smith Predictor method II were used. Some of the literature have reported smaller errors, but these cases did not all include upsampling or motion compensation for such large image acquisition and processing delays.

Using pre-recorded position data from sonomicrometry crystals sutured to the heart, average errors as low as 0.669 mm were reported in [36], but the peak error were as large as 4.3 mm. This method is not clinically viable as it is not real-time and the crystals must be sutured onto the POI site.

In [5], the residual motion (approximately 6 and 8 mm in the  $x$  and  $y$  directions) left after mechanically stabilizing the heart was compensated for by moving a 40 Hz endoscope to stabilize the image. However, this method does not let the heart beat freely and is only viable on the exterior heart surface. Mean errors of approximately 0.4 and 0.8 mm in the  $x$  and  $y$  directions and a peak error of approximately 2 mm in the  $y$ -direction were reported.

In [24], position data was collected from a 500 Hz camera. A one sample ahead predictive controller was able to reduce the tracking error to less than a millimetre. However, in this case, the position data is collected at a very fast rate meaning there is less movement between samples and the length of the prediction is much shorter.

In the most similar case to this work, Yuen et al. reported an average and peak error of 0.97 mm and 3.26 mm respectively on simulated heart motion data with a peak-to-peak amplitude of 12.36 mm [30]. These errors are very similar to those reported in this work;

however, Yuen et al. used a sampling rate of 28 Hz and therefore only predicted one time step ahead.

## 6.7 Concluding Remarks

Three controllers are presented in this chapter to provide motion compensation for physiological motion. The first assumes the transformation between the image frame and robot frame is available such that the POI's position measurements can be transformed into the robot frame. In this case, the POI's position measurements are upsampled and predicted ahead to overcome the delay. Now, a regular controller can be used to ensure that the distance between the robot and the POI follows the physician's motion.

When the transformation is not available, the distance between the POI and the surgical tool tip is measured. The POI's motion is calculated from the robot's position and the upsampled distance measurements. A Smith predictor is used in the feedback control loop to compensate for the delay. Two different configurations are proposed; the first adds the predicted POI motion to the surgeon's to form a new setpoint (previously presented in Chapter 4), and the second adds the predicted POI motion into the inner feedback loop to reflect where the POI's actual motion is added into the system (previously presented in Chapter 5). As expected, the second method which adds the predicted POI motion to the inner feedback loop performs better than the first.

In Chapters 4 and 5, it was shown that cubic interpolation performed better than zero-order-hold upsampling and that adjusting the period of the previous motion to predict the current motion performed better than EKF-based prediction. In this chapter, cubic interpolation was compared to EKF-based upsampling. As an EKF can handle quasi-periodic motion with a slowly-changing period, it outperformed cubic interpolation. EKF-based prediction performed better in this chapter as the heart rate was changed during the trials. This did not occur in Chapter 4 where adjusting the period of the previous heart motion performed the best.

## Chapter 7

# Ultrasound-based Image Guidance and Motion Compensating Control

In the previous chapters control systems that move a surgical tool in synchrony with a POI on a beating heart or organ affected by physiological motion have been presented. These control systems have been tested under imaging systems that have a similar time delay to ultrasound imaging, but were not tested under ultrasound imaging itself. In this chapter, ultrasound imaging is used to determine the position of the POI. The image processing required to find the POI quickly is presented. Finally, participants attempt to complete a task using this system to show that motion compensation can indeed enable a surgeon to operate on a moving POI.

An important aspect of the control system presented in this thesis is the fact that it is teleoperated. Previous research has presented a hand-held tool, but it does not take

---

Portions of this chapter have been submitted to the Journal of Medical Robotics Research as “Meaghan Bowthorpe and Mahdi Tavakoli. Ultrasound-based Image Guidance and Motion Compensating Control for Robot-assisted Beating-heart Surgery.”

advantage of the benefits of teleoperated robotic surgery where the surgeon operates from a separate user console with a more ergonomic posture [6, 30, 32, 56]. In addition, teleoperation can enhance the surgeon's performance as the surgeon's motions can be scaled and hand tremors can be reduced [11]. With teleoperated tools, the position of the surgical tool can easily be recorded, which is much more difficult with hand-held tools. Having this trajectory data is important for skill assessment as the motion trajectories of experienced and inexperienced surgeons can be compared as they complete the same task [12]. Teleoperation is also important for training new surgeons as trilateral teleoperation systems allow experienced and inexperienced surgeons to operate a single slave robot (the surgical robot) together [69]. In the teleoperation mode, control of the surgical robot can also be split between a control system and a surgeon if, for example, the surgical tool should not cross into a specific area. This split control could also maintain a desired contact force between an ultrasound probe and the patient, while the physician controls the other degrees of freedom of the probe's position to find the desired imaging plane [70].

This chapter is organized as follows. The development of the robot-assisted surgical system is presented in Sec. 7.1. The image processing algorithm that finds the surgical tool tip and the POI in each ultrasound image is outlined in Sec 7.1.1. The POI's slowly sampled motion is then upsampled in Sec. 7.1.2. Finally, to compensate for the delays, the POI's motion is predicted ahead to the current time in Sec. 7.1.3. The experimental setup is described in Sec. 7.2 and the surgical task based on mitral valve annuloplasty is described in Sec. 7.3. The conclusion is presented in Sec. 7.4.

## 7.1 System Development

To design a control system that will make the surgical tool tip follow the combined surgeon's and POI's motion, the surgeon's and the POI's motion must be measured. The surgical robot's position and hence the position of the surgical tool tip can be measured in the robot's frame of reference without a delay at a fast sampling rate from

the surgical robot's encoders and is denoted  ${}^R P_T''$ . The surgeon's motion can also be measured at this high sampling rate without any delay from the user console and is denoted  ${}^R P_S''$ . As the surgeon's motion is assumed to be one-dimensional, the distance between the surgeon's hand position and the user console's zero position is the same distance the slave robot should move and hence, this measurement is considered to be in the robot's frame of reference. The POI's motion is measured in ultrasound images that are acquired at a slow sampling rate. The images need to be processed to find the location of the POI which means the measurements will be delayed and the POI's position is denoted  ${}^I \bar{P}'_{POI}$ .

### 7.1.1 Ultrasound Imaging

For the proposed robot-assisted beating-heart surgical system to perform procedures on the interior surface of the heart as well as the exterior surface, the imaging modality must be able to visualize the heart tissue through the opaque blood pool. For this reason, ultrasound images were chosen despite the slow image acquisition rate because they are the most portable and least expensive medical imaging modality.

The image processing method presented in this paper does not require the use of any markers and is completed within one sample time of the image acquisition rate of 34 Hz. The image processing begins by applying a binary threshold to convert the gray-scale images to black and white images. The image processing procedure is summarized in Fig. 7.1.

The surgical tool, which has the shape of a long straight line, is found first in each image. In the first image, this is done using a Hough transform. The Hough transform converts the rectangular coordinates of each white point in the image into polar coordinates and a line is characterized by the perpendicular distance between the line and the origin ( $\rho$ ) and the angle that  $\rho$  makes with respect to the horizontal ( $\theta$ ), as shown in Fig. 7.2. All of the points on a single line have the same  $\rho$  and  $\theta$  values. A  $\rho$  and  $\theta$  pair is considered to represent a line if enough points in the image have been converted into

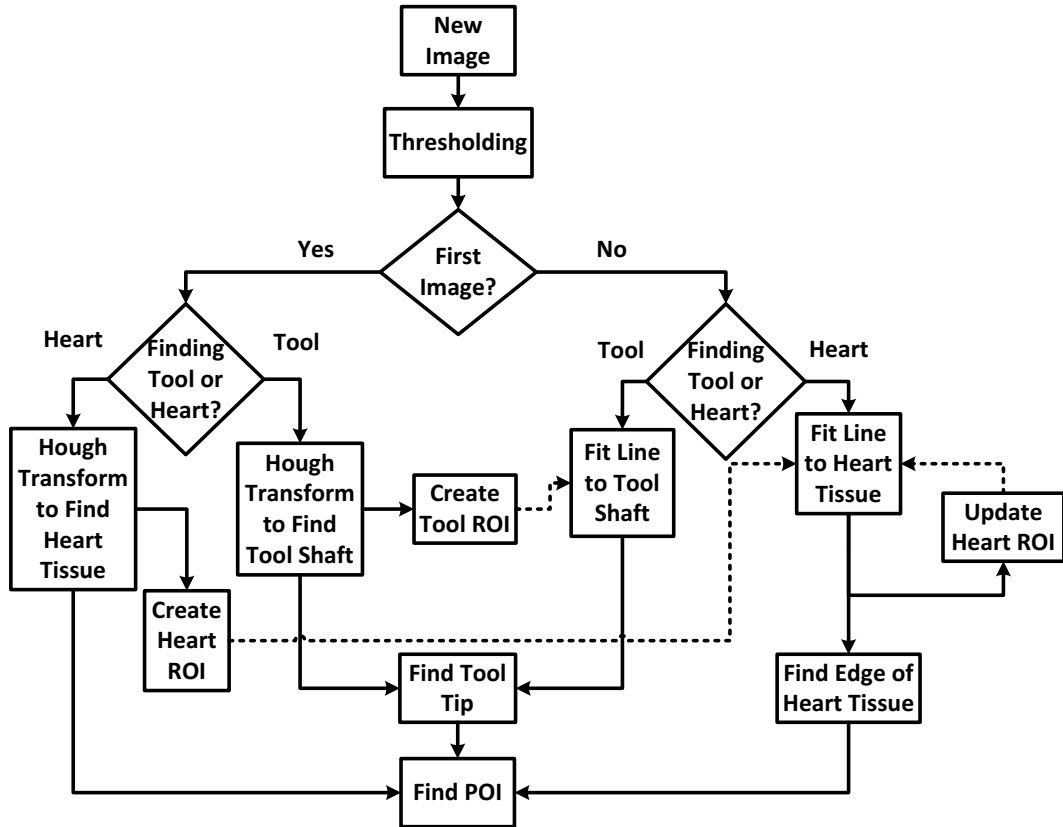


FIGURE 7.1: A flow chart of the image processing. Each image is thresholded to create a black and white image. Hough transforms are then used to locate the tool shaft and heart tissue in the first image. The ROIs are set and the tool tip and POI locations are found. Lines are then fit to the tool shaft and heart tissue in the remaining images, the edge of the heart tissue is found, the heart tissue ROI is updated, and the tool tip and POI locations are found.

polar coordinates as this pair. To find the correct line (as there will be multiple lines in the image), only the lines that form an angle with the horizontal within a  $\frac{\pi}{4}$  angular arc – the surgical tool’s expected location – are analyzed in the first image. The longest of these lines is the surgical tool shaft. Throughout the procedure, the surgical tool is confined to one-dimensional motion. To reduce the processing time of the remaining images, a region of interest (ROI) is created in the area surrounding the determined location of the surgical tool.

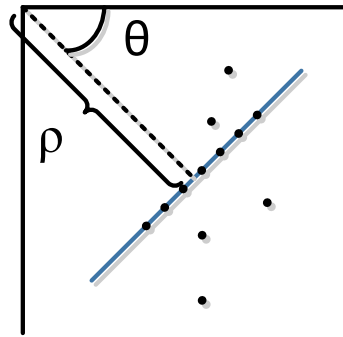


FIGURE 7.2: A Hough transform converts all points in the image to polar coordinates. All points on a single line share the same  $\rho$  and  $\theta$  value.

The Hough transform is a computationally expensive method of finding lines. In addition, as the tool shaft is a thick line, the longest line found by the Hough transform is not necessarily the centre line and may not be parallel with the tool shaft (e.g., the longest line may begin in the upper right corner of the tool and end in the lower left corner). To correctly identify the centre line of the tool shaft least squares regression is used in the remaining images, which minimizes the distance between the line and all of the candidate pixels. To minimize the computation time when identifying the candidate pixels contained within the ROI, the image is down-sampled and only every third column and third row are analysed. A line is then fit through these points using OpenCV's `fitline()`. Once the tool's shaft has been identified, the surgical tool tip,  ${}^I\bar{P}'_T$ , is found by extending the line along the surgical tool shaft until the last candidate pixel point. Fig. 7.3a shows the result of finding the tool. The ROI surrounding the tool shaft is marked by the green lines, the center of the tool shaft is given by the purple line, and the tool tip is shown by the blue dot.

The heart tissue is found in a manner similar to the tool's shaft. In the first image, a Hough transform identifies the longest line that forms an angle with the horizontal within a  $\frac{\pi}{4}$  angular arc of the image that is perpendicular to the surgical tool shaft. A second ROI is then created to identify the area surrounding the heart tissue. As the heart tissue moves continually, the ROI surrounding the heart tissue is updated after

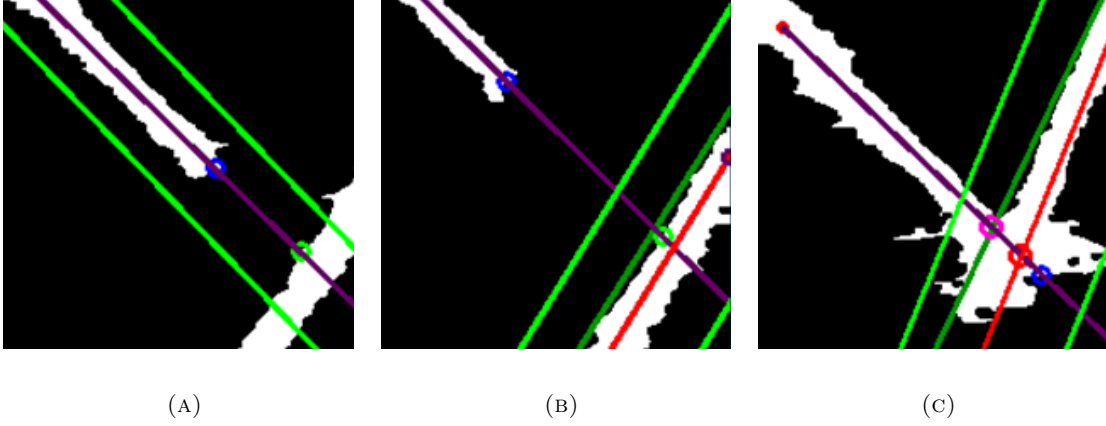


FIGURE 7.3: The result of the image processing required to find the surgical tool shaft and tip (a), and the heart tissue and the POI (b) and (c). The light green lines form the boundary of the ROI, the purple line identifies the surgical tool shaft, the blue dot shows the surgical tool tip in (a) and (b), the green dot shows the POI in (b), and the pink dot shows the surgical tool tip and POI in (c).

every image. In all subsequent images, the heart tissue is identified by fitting a line using least squares regression. Once again, to minimize the computation time when identifying the candidate pixels contained within the ROI, the image is down-sampled and only every third column and third row are analysed. Within every subsequent image, the candidate pixels on the upper edge of the heart tissue are identified and a straight line is fit through them. This identifies the edge of the heart tissue closest to the surgical tool and will later be used when finding the POI. Figs. 7.3b and 7.3c show the result of finding the heart tissue. The ROI surrounding the heart tissue is marked by the light green lines, the edge of the heart tissue is given by the dark green line, and the centre line of the heart is given by the red line.

The goal of the motion compensating controller is to maintain a desired distance between the tip of the surgical tool and the POI. Since the POI location is reported with a slow sampling rate (ultrasound image refresh rate) and is subject to the image acquisition and processing delays, it is denoted  ${}^I\bar{P}'_{POI}$ . The location of the POI is found by extending the line through the surgical tool shaft and locating the first candidate pixel beyond the surgical tool's tip – the heart tissue. However, a difficulty arises when the surgical tool tip makes contact with the heart tissue. In this case, it is still possible to identify

the shaft of the surgical tool, but not its tip location nor the location of the POI as the surgical tool and the heart tissue will appear as one solid object in the image. To separate the two, we begin by determining whether the surgical tool tip has collided with the heart. If the line identifying the tool shaft intersects with the line through the heart, there is a collision between the surgical tool tip and the heart tissue. In this scenario, the POI is identified by the intersection of the line found along the edge of the heart tissue and the line through the surgical tool shaft. Fig. 7.3b shows the location of the POI when the surgical tool and the heart do not touch – green dot – and Fig. 7.3c shows the location of the POI when they do – pink dot.

There are two main challenges to overcome when using ultrasound guidance: the slowly sampled data and the image acquisition and processing delay. To overcome these challenges, we propose to first upsample the position data using cubic interpolation based upsampling. Next the POI's motion is predicted ahead for the duration of the image acquisition and processing delay to the current time using an extended Kalman filter (EKF).

### 7.1.2 POI Motion Upsampling

To take advantage of the robot's faster sampling rate, the slowly sampled POI position data will be upsampled using cubic interpolation to 100 Hz.

The following equation describe the cubic interpolated upsampled data points  $p(i)$ :

$$p(i) = h_{00}(i)p_0 + h_{10}(i)m_0 + h_{01}(i)p_1 + h_{11}(i)m_1 \quad (7.1)$$

where the  $h$  coefficients are as follows:

$$h_{00}(i) = 2i^3 - 3i^2 + 1 \quad (7.2a)$$

$$h_{10}(i) = i^3 - 2i^2 + i \quad (7.2b)$$

$$h_{01}(i) = -2i^3 + 3i^2 \quad (7.2c)$$

$$h_{11}(i) = i^3 - i^2 \quad (7.2d)$$

where  $p_0$  and  $p_1$  are the points in between which the interpolation is occurring, and  $m_0$  and  $m_1$  are the slopes at  $p_0$  and  $p_1$ , respectively. The interpolation variable  $i$  contains evenly spaced values between 0 and 1, and has a length of one greater than the number of points to be upsampled between the two slowly sampled points  $p_0$  and  $p_1$ . As four data points are required (points  $p_0$  and  $p_1$  and a data point on either side used to calculate the slope) to ensure that the upsampled signal and its first derivative are smooth, cubic interpolation involves a processing delay of  $2n - 1$  fast sample times, where  $n$  is the number of samples added to the signal. The POI's motion,  ${}^I\bar{P}''_{POI}$  is now estimated at the fast sampling rate, but it is still delayed.

### 7.1.3 POI Motion Prediction

Once the position data has been upsampled, the POI's position must be predicted ahead to the current time to overcome the image acquisition and processing delay inherent in ultrasound-based POI motion tracking as well as the delay caused by cubic interpolation, which is 170 ms. Here an EKF is used for prediction as it allows for a changing heart or respiratory rate and changing amplitude in the motion signal.

The signal model  $y(\mathbf{x}(t))$  for the POI's position is a Fourier series in which the coefficients can vary with time (7.3) [30, 68]:

$$y(\mathbf{x}(t)) \triangleq c + \sum_{l=1}^m r_l \sin \theta_l(t) \quad (7.3a)$$

$$\theta_l(t) = l \int_0^t \omega(\tau) d\tau + \phi_l(t) \quad (7.3b)$$

$$\mathbf{x}(t) = [c(t), r_l(t), \omega(t), \theta_l(t)]^T \quad (7.3c)$$

The EKF describing the POI's motion is based on the state space model (7.4) that evolves through random walk, where the offset  $c$ , the sine wave coefficients  $r_l$ , and the frequency  $\omega(t)$  remain constant between samples. Only the  $\theta_l$  values are updated according to (7.3b) in each sample time. These values are later updated by the EKF based on the error between the predicted and actual measurement, except for the frequency,  $\omega$ , which is replaced by the value measured directly from the past POI motion.

$$\mathbf{x}(t + \Delta t) = \mathbf{F}(\Delta t)\mathbf{x}(t) + \mu(t) \quad (7.4a)$$

$$z(t) = y(\mathbf{x}(t)) + v(t) \quad (7.4b)$$

where

$$\mathbf{F}(\Delta t) = \left[ \begin{array}{c|ccc} \mathbf{I}_{m+1} & & & \mathbf{0} \\ \hline & 1 & & \\ & \Delta t & 1 & \\ \mathbf{0} & 2\Delta t & 0 & 1 \\ & \vdots & & \ddots \\ & m\Delta t & & 1 \end{array} \right]_{[2m+2] \times [2m+2]} \quad (7.5)$$

and  $\mu(t)$  and  $v(t)$  are independent Gaussian noise terms.

Next, the EKF is updated every fast sample time by the following equations as the POI motion was previously upsampled:

$$\mathbf{P}(t + \Delta t|t) = \mathbf{F}(\Delta t)\mathbf{P}(t|t)\mathbf{F}(\Delta t)^T + \mathbf{Q} \quad (7.6a)$$

$$S = \sigma_R^2 + \mathbf{H}(\Delta t)\mathbf{P}(t + \Delta t|t)\mathbf{H}(\Delta t)^T \quad (7.6b)$$

$$\mathbf{K}(t) = \mathbf{P}(t + \Delta t|t)\mathbf{H}(\Delta t)^T S^{-1} \quad (7.6c)$$

$$\hat{\mathbf{x}}(t + \Delta t|t + \Delta t) = \mathbf{F}(\Delta t)\hat{\mathbf{x}}(t|t) + \mathbf{K}(t)(z(t + \Delta t) - y(\mathbf{F}(\Delta t)\hat{\mathbf{x}}(t|t))) \quad (7.6d)$$

$$\mathbf{P}(t + \Delta t|t + \Delta t) = (\mathbf{I} - \mathbf{K}(t)\mathbf{H}(\Delta t))\mathbf{P}(t + \Delta t|t) \quad (7.6e)$$

where  $\mathbf{P}(t)$  is the estimated covariance matrix, which is a  $[2m + 2] \times [2m + 2]$  diagonal matrix with  $[0.001, 0.1/1, 0.1/2, \dots, 0.1/m, 0.1, 0.2_{1 \times m}]$  along the diagonal,  $\mathbf{Q}$  is the process noise covariance matrix, which is also a  $[2m + 2] \times [2m + 2]$  diagonal matrix with 0.0001 along the diagonal,  $\sigma_R^2$  is the observation noise covariance matrix, which is a scalar with a value of 0.01, and  $\mathbf{H}(\Delta t)$  is

$$\mathbf{H}^T(\Delta t) = \left( \frac{\partial y}{\partial \mathbf{x}} \right)^T \bigg|_{\hat{\mathbf{x}}(t+\Delta t|t) = \mathbf{F}\hat{\mathbf{x}}(t|t)} = \begin{bmatrix} 1 \\ \sin \hat{\theta}_1(t + \Delta t|t) \\ \vdots \\ \sin \hat{\theta}_m(t + \Delta t|t) \\ \hat{r}_1(t + \Delta t|t) \cos \hat{\theta}_1(t + \Delta t|t) \\ \vdots \\ \hat{r}_m(t + \Delta t|t) \cos \hat{\theta}_m(t + \Delta t|t) \end{bmatrix} \quad (7.7a)$$

where the  $\hat{\cdot}$  symbol denotes the estimated value.

To predict future POI positions, the state matrix  $\mathbf{x}$  is multiplied  $j$  times by the update matrix  $\mathbf{F}$  to move  $j$  steps ahead:

$$\hat{\mathbf{x}}(t + j\Delta t|t + \Delta t) = \mathbf{F}(\Delta t)^j \hat{\mathbf{x}}(t + \Delta t|t) \quad (7.8)$$

The predicted position,  ${}^I \hat{P}_{POI}''$  is found by calculating (7.3a) using the predicted  $\mathbf{x}(t +$

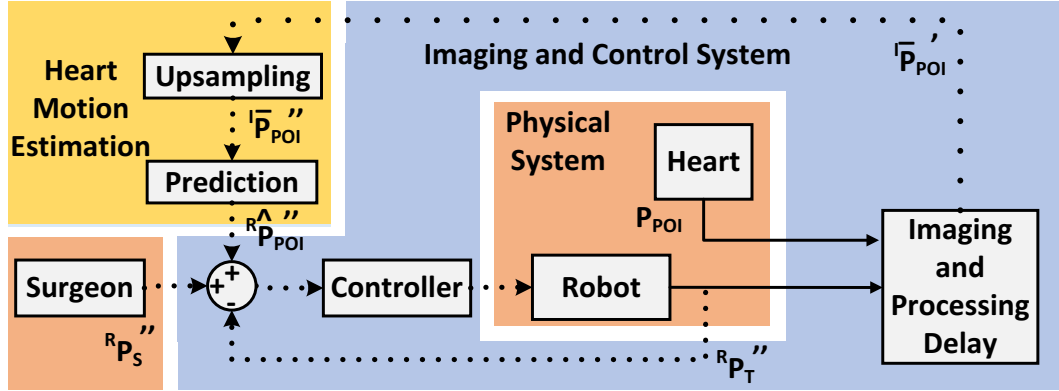


FIGURE 7.4: A simple feedback controller for teleoperated motion compensation. Here, the setpoint for the robot’s position,  ${}^R P_T''$  is the combination of the surgeon’s position,  ${}^R P_S''$ , and the estimated current POI position  ${}^R \hat{P}_{POI}''$ .

$j\Delta t|t + \Delta t)$  found above. As the POI’s motion is confined to 1D, the direction of the axis of the surgical tool, it is converted to the robot’s frame by converting the distance between the POI and the origin (common to both the image and robot frame) in pixels into millimetres to obtain  ${}^R \hat{P}_{POI}''$ .

#### 7.1.4 Predictive Feedback Control of the Surgical Robot

The feedback control structure synchronizes the distance between the surgical tool tip and the POI. When designing this controller, either the controller itself must compensate for the delayed position measurements, or the delayed position measurements must be predicted forward to the current time before being fed to the controller. Previously, we took the former approach in [8, 46]. In this work, a simpler controller will be used and the delayed position measurements are predicted forward to the current time.

A diagram of the utilized feedback loop is given in Fig. 7.4. The surgical tool tip’s motion will be controlled to follow the combination of the POI’s motion and the surgeon’s motion. First, the POI’s motion is upsampled according to (7.1), predicted ahead according to (7.3a and 7.8), and converted into the robot’s frame of reference to become  ${}^R \hat{P}_{POI}''$ .

## 7.2 Experimental Setup

The experimental setup shown in Fig. 7.5 uses a 6 MHz 4DL14-5/38 linear 4D transducer connected to a SonixTouch ultrasound scanner (SonixTouch from Ultrasonix, Richmond, BC, Canada) as the image sensor, which has a low frame rate of 34 Hz. The depth of the images was 4.5 cm. The ultrasound images were collected from the ultrasound scanner using a DVI2USB 3.0 frame grabber (Epiphan, Ottawa, ON, Canada). The entire image acquisition, processing delay and upsampling delay is 170 ms. A custom-built mechanical cam (simulated heart) generated the POI motion. The shape of the cam is based on the motion trajectory collected from the movement of a point on the side wall of the heart in a series of clinical ultrasound images of a patient’s beating heart. The single degree-of-freedom (DOF) surgical tool (surgical robot) is actuated by a voice coil motor (NCC20-18-020-1X from H2W Technologies Inc., Santa Clarita, CA, USA). To verify the results, real-time position measurements of both the mechanical cam and the robot were collected from two potentiometers (LP-75FP-5K and LP-30FP-1K from Midori America Corp., Fullerton, CA, USA); however the real-time measurement of the mechanical cam’s motion was not made available to the controller. The entire system is controlled at a fast sampling rate of 100 Hz.

For each trial, the heartbeat motion has a peak-to-peak amplitude of 10 mm and a period of 64 bpm (1.07 Hz). Three error metrics are calculated for each trial: the mean absolute error (MAE) between the upsampled and fast discrete-time signal (measured from the potentiometers) is  $\frac{\sum |error|}{l}$ , where  $l$  is the number of data points in the sample, the integral squared error (ISE) is  $\frac{\sum (error)^2}{l}$ , and the peak error is the largest error at a single point in time. The results from each of the trials are summarized in Table 7.1.

## 7.3 Surgical Task

The surgical task presented simulates deploying a staple to secure an annuloplasty ring onto the mitral valve. If the mitral valve is not shaped properly, it may not seal when

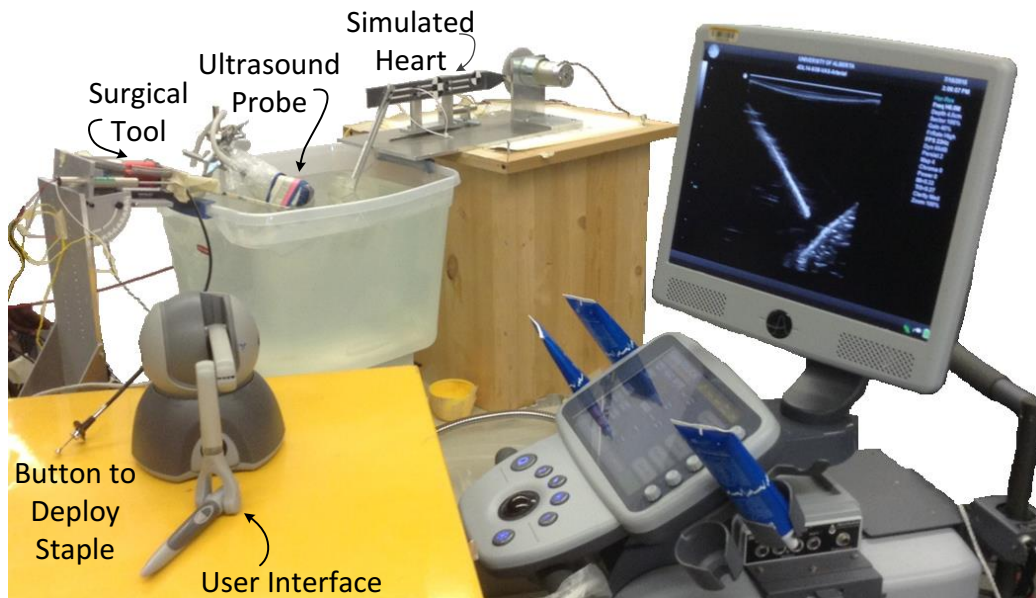


FIGURE 7.5: The experimental setup.

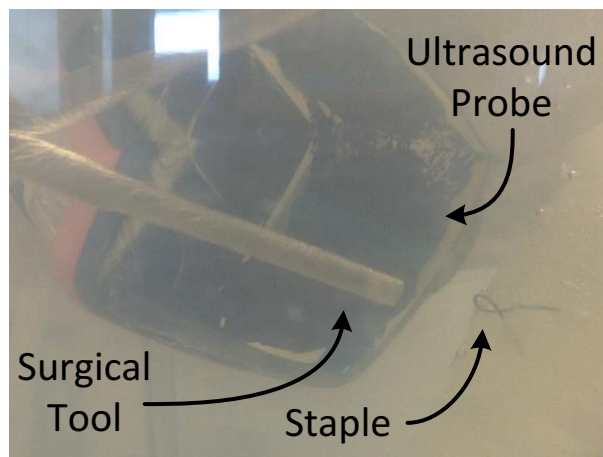


FIGURE 7.6: A successfully deployed staple.



FIGURE 7.7: An example of using too much force when deploying the staple.

the ventricle contracts. This allows blood to flow backwards through the heart, making each heart beat less efficient. Mitral valve annuloplasty is explained in more detail in Sec. 3.1.2. More than 300,000 people undergo mitral valve annuloplasty each year worldwide [71]. If securing this annuloplasty ring could be performed while the heart is still beating, the effectiveness of the newly reshaped valve could be evaluated immediately. This user study was approved by the University of Alberta's Research Ethics Office #Pro00055825.

In this study, the participant is asked to deploy the staple into moving heart tissue. The participant moves the surgical tool through teleoperation by moving the stylus of a PHANToM Omni (Geomagic, Cary, NC, USA) – the user interface. The heart tissue is a piece of soft plastic visible under ultrasound. This simulated heart tissue is connected to the mechanical cam and moves in a quasi-periodic fashion – simulated heart. The surgical tool is rigidly attached to a stand and has a 5 cm range of motion. The ultrasound probe is positioned such that the simulated heart's motion and the motion of the surgical tool are visible. The participant views the motion of the simulated heart tissue and the surgical tool on the ultrasound screen. Finally, the participant holds a button connected to the surgical tool in his or her other hand and presses it to deploy the staple. An image of a successfully deployed staple is shown in Fig. 7.6. This task

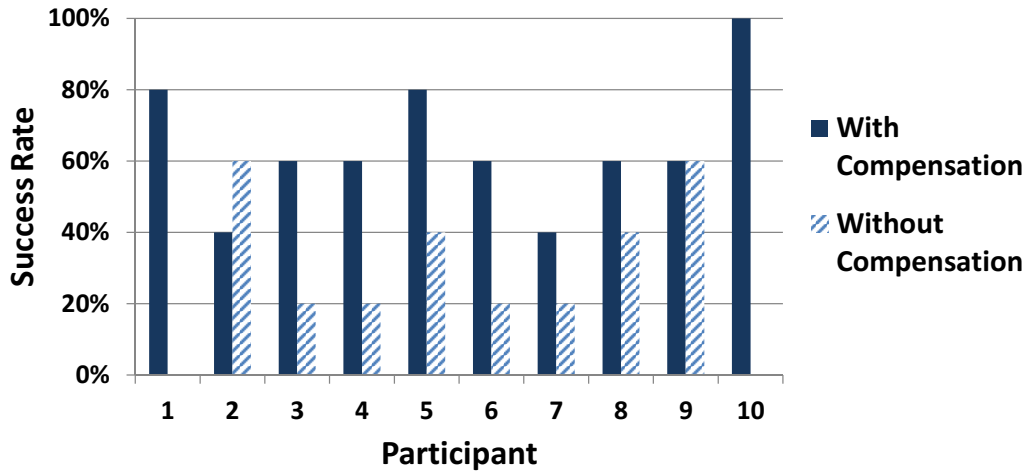


FIGURE 7.8: The rate of successful deployment of the staple for each participant.

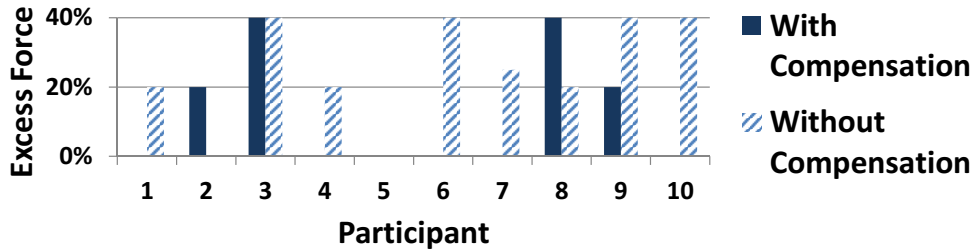


FIGURE 7.9: The rate of the use of excessive force for each participant.

is completed under two conditions: with and without motion compensation. For both conditions, the participants view the ultrasound video of the simulated heart tissue and surgical tool. While completing this task, the participant is told not to press the tool into the tissue such that the tissue deforms.

Each participant successfully deployed three staples with motion compensation before beginning the trials. They were also allowed to practice under both conditions until they felt comfortable with the system before starting the trials. Each participant completed 10 trials, 5 with motion compensation and 5 without. The trials alternated between the two control conditions starting with motion compensation. If the surgical tool left an indent in the phantom tissue when the staple was deployed (see Fig. 7.7), the trial was counted as a failure and a penalty was assigned regardless of whether or not the staple deployment was successful.

The trials included 10 participants who were not surgeons (2 females and 8 males) ages 21-30. When there was no motion compensation, the staple was successfully deployed in 28% of the trials and excessive force, leaving an indent in the tissue, occurred in 24.5% of the trials. When motion compensation was provided, the success rate more than doubled to 64% and the use of excessive force was reduced by half to 12% of the trials. The success rate of each participant is given in Fig. 7.8 and the rate of the use of excessive force is given in Fig. 7.9.

To compare the success rates we used a two-tailed *t-test* and obtained the probability of the null hypothesis  $\mu_1 = \mu_2$  for the 10 trials [72]. The probability of the results assuming the null hypothesis for the success of the staple deployment with and without compensation was 0.01 and for the use of excess force with and without compensation was 0.10. These results indicate that there was a significant difference between providing and not providing motion compensation with respect to the successful deployment of the staple, but not with respect to the use of excessive force.

When motion compensation was not provided, only 3 of the 10 participants, participants 3, 9, and 10 attempted to manually compensate for the heart's motion. These participants used excessive force in 40% of the trials, which is much higher than the average rate of 24.5%. The majority of participants simply waited for the tissue to approach the tool tip and then deployed the staple at the correct time. This method is possible, because the staple can be deployed very quickly. However, the tasks in most surgical procedures cannot be performed so quickly and would hence have higher failure rates as this method would no longer be feasible.

When motion compensation was provided, it was easier for the user to move the surgical tool towards the moving heart tissue. The user's motions for this case creates the pink line in Fig. 7.10a. The user's motion simply moves the surgical tool tip towards the heart tissue. The solid black line in this figure is the resulting distance between the surgical tool tip and the POI and the solid red line is the error. Part (b) of Fig. 7.10 shows the result of the motion compensation. Here, the surgeon's motion has been subtracted

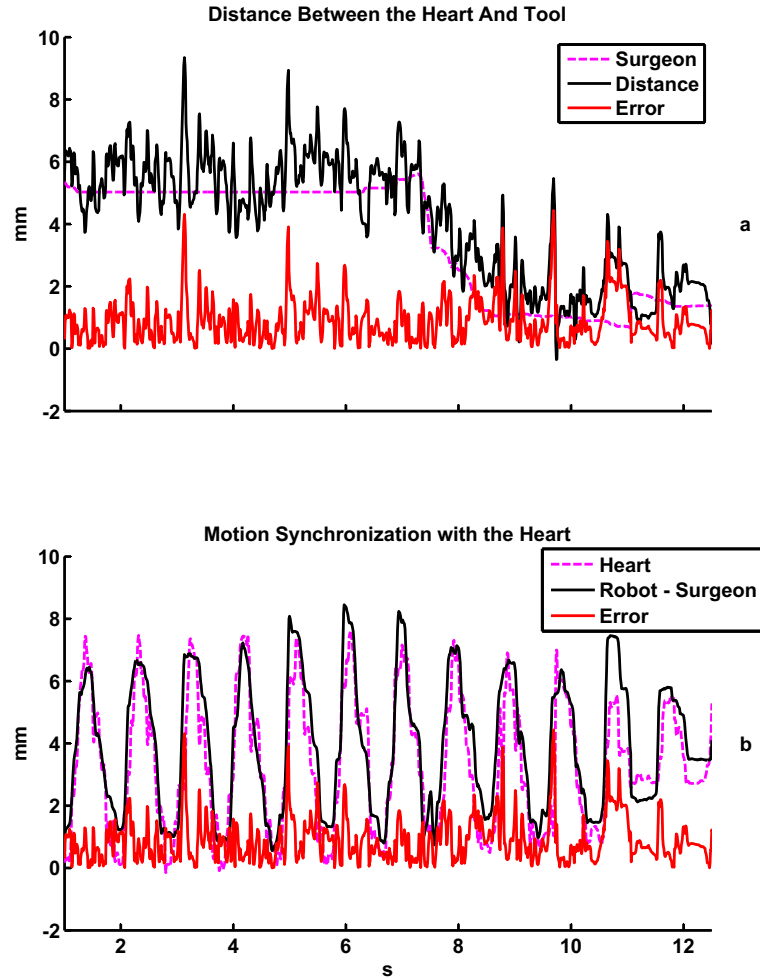


FIGURE 7.10: The result when motion compensation is provided. In case (a), the dashed pink line is the user's motion, the solid black line is the distance between the surgical tool tip and the heart tissue, and the red line is the error between these two. Case (b) shows the motion synchronization. Here, the surgeon's motions have been subtracted from the surgical tool tip's motion leaving the heart following portion of the surgical tool tip's motion – the solid black line. The heart's motion is the dotted pink line and the error between the two is the red line.

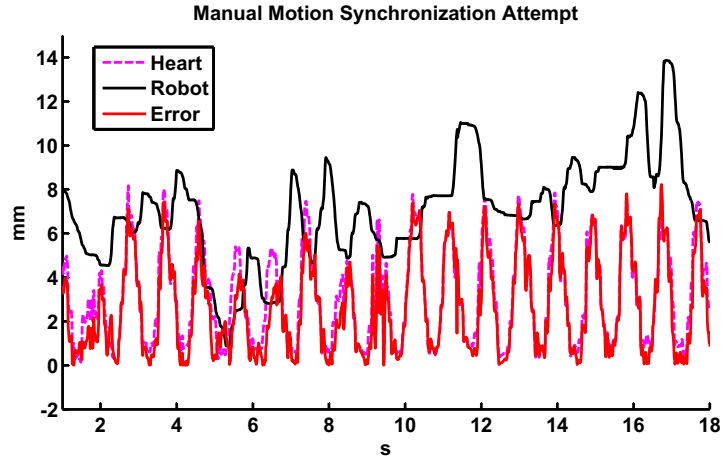


FIGURE 7.11: The result when motion compensation is not provided. Here the user tries to manually compensate for the heart’s motion. The solid black line shows the surgical tool tip minus the user’s motions, which should follow the heart’s motion.

from the surgical tool tip’s motion to remove the offset between the surgical tool tip and the heart tissue – the solid black line. The POI’s motion is given by the dashed pink line and the error is given by the solid red line. The MAE tracking error when motion compensation is provided is 0.95 mm, the ISE tracking error is  $3.58 \text{ mm}^2$ , and the absolute value of the peak tracking error is 3.58 mm. It is much harder for the user to follow the POI’s motion when no motion compensation is provided. Fig. 7.11 shows the surgeon’s motion – the solid black line and the POI’s motion – the dashed pink line. It is quite obvious that the errors are quite large – the solid red line. The MAE tracking error when motion compensation is not provided is 4.33 mm, the ISE tracking error is  $27.19 \text{ mm}^2$ , and the absolute value of the peak tracking error is 11.78 mm.

The average and peak tracking error reported in this work, 0.95 mm and 3.58 mm, is similar to those reported in the literature. Sub-millimetre errors were reported when a 500 Hz camera measured the position of the POI and the time delay was limited to one sample time in [24]. The use of pre-recorded data resulted in average errors as low as 0.669 mm and peak errors as large as 4.3 mm in [36]. However, this method is not viable in real-time. The use of motion compensation after the heart is stabilized by a

Motion Compensation	MAE (mm)	ISE (mm <sup>2</sup> )	Peak Error (mm)
Yes	0.95	1.38	3.58
No	4.33	27.19	11.78

TABLE 7.1: A summary of the experimental results.

mechanical stabilizer resulted in small errors of 0.4 and 0.8 mm in the  $x$  and  $y$  directions and a peak error of 2 mm in the  $y$ -direction in [5]. However, this method does not let the heart beat freely. Finally, an average and peak error of 0.97 mm and 3.26 mm respectively was reported in [30] where the POI motion was measured from ultrasound images. A similar user task performed with a hand-held motion compensating surgical tool reported a success rate of 74% when motion compensation was provided and only 32% when motion compensation was not provided.

## 7.4 Concluding Remarks

The control systems presented in the thesis are designed to operate under ultrasound guidance. However, in the previous chapters ultrasound imaging has been simulated by a Micron Tracker that includes its own software to locate the position of markers. In this chapter, the POI's position was found with ultrasound images. The image processing required to quickly and reliably find the POI's position is presented. An EKF-based prediction scheme is used to predict the POI's future motion from the delayed motion upsampled with cubic interpolation. A proportional controller is then used to ensure the surgical tool follows the summation of the POI's and the surgeon's motion.

To show the efficacy of this system, user trials simulating deploying a staple for mitral valve annuloplasty were conducted. The results indicate that the improvement in the success rate when motion compensation is provided is statistically significant. The success rate when motion compensation was not provided was aided by the fact that the participant did not need to follow the heart's motion to successfully deploy the staple. Rather, the participant could simply move the surgical tool to the furthest point in the

heart's trajectory so the two came into contact once every beat. They then deployed the staple at the correct moment. This method was successful in this case; however, this method would not be successful for more complicated surgical procedures where the surgical tool must remain in contact with the heart for any length of time.

## Chapter 8

# Generalized Predictive Control for Delay Compensation and Disturbance Rejection

Previously, we have compensated for the delay within the feedback loop using Smith predictors or proportional controllers. The Smith predictor and proportional controller, like many controllers, calculate the control signal based on the delayed and estimated position errors. They do not take any future position errors into account as the future output and input values are generally unknown. However, because the heart's motion is quasi-periodic we can predict where the heart will be in the future. In addition, with a model of the surgical robot, we can estimate how it will react to a given control signal and estimate future outputs. As the input to the controller is the error between the surgical robot's position and the summation of the POI's motion and the surgeon's

---

Portions of this chapter have been published in “M. Bowthorpe, A. Álvarez García, and M. Tavakoli. GPC-based Teleoperation for Delay Compensation and Disturbance Rejection in Image-guided Beating-heart Surgery, *IEEE International Conference on Robotics and Automation*, Hong Kong, China, 2014.” [50]

motion and the output is the surgical robot's position, estimates of the future input and output signals can be calculated, provided the surgeon can operate with a short delay in the transmission of his or her hand motions. Although it is more difficult, surgeons have the ability to perform a surgical procedure with a teleoperation system with delays of up to 300 ms [73]. Generalized predictive control (GPC) takes advantage of these estimated input and output positions and calculates the optimal control signal over a given horizon into the future. In this chapter two configurations of GPC are presented.

The rest of this chapter is organized as follows. Section 8.1 reviews the generalized predictive control law and describes the algorithms used to develop a beating-heart surgical system. Section 8.2 describes the experimental setup and results that validate the proposed algorithm. The concluding remarks are given in Section 8.3.

## 8.1 Generalized Predictive Control-based Motion Compensation

Generalized predictive control was chosen due to its ability to compensate for a time delay, in this case the image acquisition and processing delay, and to reject disturbances caused by the heart motion [74]. In GPC, the system is modeled by a controlled autoregressive integrated moving average (CARIMA) equation – see (8.1) – that includes a time delay of  $d$  samples [74].

An overview of GPC is shown in Fig. 8.1. The control signal is calculated by minimizing the difference between the estimated system output (position) and the given desired reference signal over a given horizon while limiting the magnitude of the control signal. Therefore, a model of the robot is required to estimate future outputs based on current inputs and the known reference signal. The reference signal is continually updated, and if the reference signal includes the estimated heart motion as will be shown later, it will be continually updated to reflect any changes in the actual heart motion.

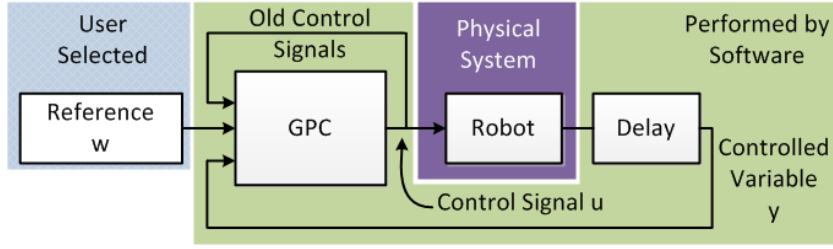


FIGURE 8.1: A GPC feedback control system.

In order to design a GPC law, we begin with a CARIMA model to describe the robot dynamics:

$$A(z^{-1})y[kT] = B(z^{-1})u[(k-1)T]z^{-d} + \frac{C(z^{-1})}{\Delta}e[kT] \quad (8.1)$$

In the above,  $z^{-1}$  is the backward shift operator,  $\Delta = 1 - z^{-1}$ ,  $T$  is the sampling interval, and  $k$  is an integer. The current system output is  $y[kT]$ , the previous sampling interval's control signal (input) is  $u[(k-1)T]$ , and the current disturbance is  $e[kT]$ .  $A$ ,  $B$ , and  $C$  are polynomials of order  $n_a$ ,  $n_b$ , and  $n_c$  respectively.

$$A(z^{-1}) = 1 + a_1z^{-1} + a_2z^{-2} + \dots + a_{n_a}z^{-n_a} \quad (8.2a)$$

$$B(z^{-1}) = b_0 + b_1z^{-1} + b_2z^{-2} + \dots + b_{n_b}z^{-n_b} \quad (8.2b)$$

$$C(z^{-1}) = 1 + c_1z^{-1} + c_2z^{-2} + \dots + c_{n_c}z^{-n_c} \quad (8.2c)$$

The goal of generalized predictive control is to minimize the difference between the optimal prediction of the plant's future outputs given the current output  $\hat{y}[(k+j)T|kT]$  and the future reference values  $w[(k+j)T]$  while keeping the change in the control effort  $\Delta u[(k+j-1)T]$  small. The cost function is then:

$$J(N_1, N_2, N_u) = \sum_{j=1}^{N_u} \lambda(j) \left[ \Delta u[(k+j-1)T] \right]^2 + \sum_{j=N_1}^{N_2} \delta(j) \left[ \hat{y}[(k+j)T|kT] - w[(k+j)T] \right]^2 \quad (8.3)$$

where  $N_1$  and  $N_2$  are the minimum and maximum costing horizons,  $N_u$  is the control horizon and is equal to  $N_1 - N_2$ , and  $\delta(j)$  and  $\lambda(j)$  are weighting factors. To estimate future values of  $y$  we start with the following Diophantine equation:

$$1 = E_j(z^{-1})\tilde{A}(z^{-1}) + z^{-j}F_j(z^{-1}) \quad (8.4)$$

where  $\tilde{A}(z^{-1}) = \Delta A(z^{-1})$ , and  $E_j(z^{-1})$  and  $F_j(z^{-1})$  are polynomials of degree  $j - 1$  and  $n_a$ , respectively.  $E_j(z^{-1})$  and  $F_j(z^{-1})$  can be uniquely found given  $A(z^{-1})$ . Now multiply (8.1) by  $\Delta E_j(z^{-1})z^j$ , considering (8.4), and the white noise case where  $C(z^{-1}) = 1$  we obtain:

$$\hat{y}[(k + j)T] = F_j(z^{-1})y[kT] + E_j(z^{-1})e[(k + j)T] + E_j(z^{-1})B(z^{-1})\Delta u[(k + j - d - 1)T] \quad (8.5)$$

Assuming the best estimate of future errors  $e[(k + j)T]$  is zero we obtain:

$$\hat{y}[(k + j)T|kT] = F_j(z^{-1})y[kT] + G_j(z^{-1})\Delta u[(k + j - d - 1)T] \quad (8.6)$$

where  $G_j(z^{-1}) = E_j(z^{-1})B(z^{-1})$ .

In vector form (8.6) is:

$$\mathbf{y} = \mathbf{G}\mathbf{u} + \mathbf{F}(z^{-1})y[kT] + \mathbf{G}'(z^{-1})\Delta u[(k - 1)T] = \mathbf{G}\mathbf{u} + \mathbf{f} \quad (8.7)$$

where

$$\mathbf{y} = \begin{bmatrix} \hat{y}[(k + d + 1)T|kT] \\ \hat{y}[(k + d + 2)T|kT] \\ \vdots \\ \hat{y}[(k + d + N_u)T|kT] \end{bmatrix} \quad (8.8)$$

$$\mathbf{G} = \begin{bmatrix} g_0 & 0 & \dots & 0 \\ g_1 & g_0 & \dots & 0 \\ \vdots & \vdots & \vdots & \vdots \\ g_{N_u-1} & g_{N_u-2} & \dots & g_0 \end{bmatrix} \quad (8.9)$$

$g_0, g_1, \dots, g_{N_u-1}$  are the coefficients of  $G_j$ ,

$$\mathbf{u} = \begin{bmatrix} \Delta u[kT] \\ \Delta u[(k+1)T] \\ \vdots \\ \Delta u[(k+N_u-1)T] \end{bmatrix} \quad (8.10)$$

$$\mathbf{G}'(z^{-1}) = \begin{bmatrix} (G_{d+1}(z^{-1}) - g_0)z \\ (G_{d+2}(z^{-1}) - g_0 - g_1z^{-1})z^2 \\ \vdots \\ (G_{d+N_u}(z^{-1}) - g_0 - g_1z^{-1} - \dots - g_{N_u-1}z^{N_u-1})z^N \end{bmatrix} \quad (8.11)$$

and

$$\mathbf{F}(z^{-1}) = \begin{bmatrix} F_{d+1}(z^{-1}) \\ F_{d+2}(z^{-1}) \\ \vdots \\ F_{d+N_u}(z^{-1}) \end{bmatrix} \quad (8.12)$$

The cost function can be rewritten as:

$$J = (\mathbf{G}\mathbf{u} + \mathbf{f} - \mathbf{w})^T(\mathbf{G}\mathbf{u} + \mathbf{f} - \mathbf{w}) + \lambda \mathbf{u}^T \mathbf{u} \quad (8.13)$$

where

$$\mathbf{w} = \begin{bmatrix} w[(k+1)T] \\ \vdots \\ w[(k+N_u)T] \end{bmatrix} \quad (8.14)$$

From (8.13)  $\Delta u[kT]$  can be calculated.

$$\Delta u[kT] = K(\mathbf{w} - \mathbf{f}) \quad (8.15)$$

where  $\mathbf{K} = (\mathbf{G}^T \mathbf{G} + \lambda \mathbf{I})^{-1} \mathbf{G}^T$ ,  $\mathbf{I}$  is an identity matrix with the same size as  $\mathbf{G}$ ,  $\lambda$  is a weighting factor, and  $K$  is the first line of  $\mathbf{K}$ . For more details see [75].

### 8.1.1 Surgical Robot Control Algorithm

Two different approaches can be taken when developing the GPC system for a robot-assisted beating-heart surgical system. This choice stems from the fact that there are three possible outputs from the processed images: the heart position, the surgical tool position, and the distance between the heart and the surgical tool. Each of these measurements will be delayed the length of the image acquisition and processing delay. The goal is to make the surgical tool follow the heart's motion and this can be done in two different ways.

The first method, shown in Fig. 8.2, is to control the distance between the surgical tool tip and the heart to follow the surgeon's commanded motion. In this case the reference signal  $w$  is simply the surgeon's motion, the controlled variable  $y$  is the distance between the surgical tool tip and the heart, and the heart's motion is treated as an unknown disturbance. In the figure, the darker section is the physical system that cannot be changed and the lighter section is performed by software and can be changed.

The second method, shown in Fig. 8.3, is to directly control the position of the surgical tool to follow the motion of the heart, which is not known in real time. An estimate of the heart position is obtained by delaying the actual heart position by the length of

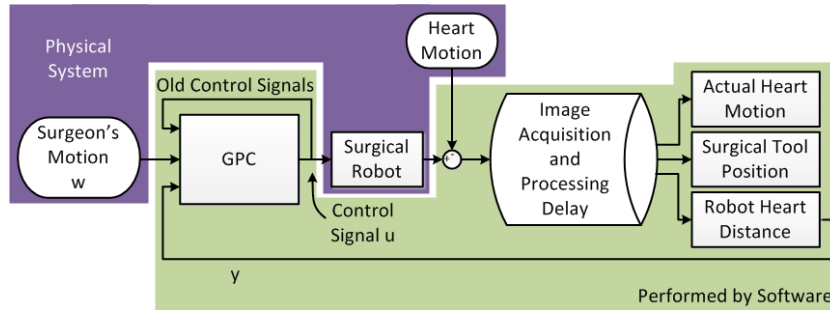


FIGURE 8.2: A model of the robot-assisted beating-heart surgical system where the distance between the surgical tool tip and the POI on the heart is being controlled to follow the surgeon's motion.

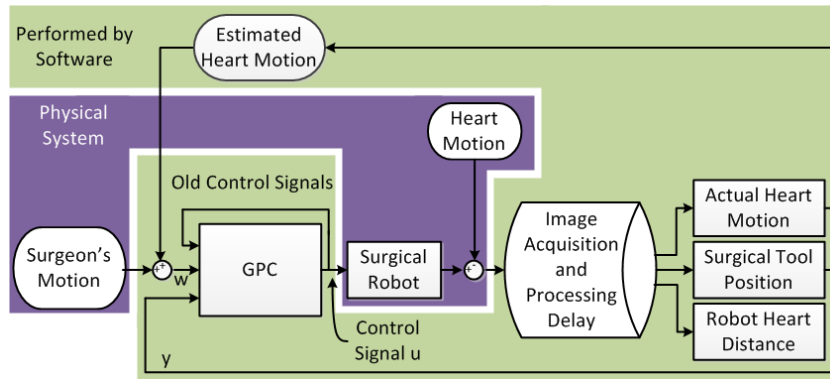


FIGURE 8.3: A model of the robot-assisted beating-heart surgical system where the surgical tool tip is being controlled to follow the combination of the estimated heart motion and the surgeon's motion. The estimated heart motion is calculated from the heart's motion in the previous heart beat.

one heart beat. The tracking error is then reduced to the difference between the heart motion and the estimated heart motion. The reference signal  $w$  is the summation of the surgeon's motion and the estimated heart motion and the controlled variable  $y$  is the surgical tool's position. In the figure, the darker section is the physical system that cannot be changed and the lighter section is performed by software and can be changed.

## 8.2 Experimental Results

The two proposed GPC control methods were tested experimentally. A voice coil (NCC20-18-020-1X from H2W Technologies Inc., Santa Clarita, CA, USA) shown in

Fig. 8.4 was used to actuate the surgical tool. The motion of the surgical tool and a simulated beating heart was captured using an Hx60 MicronTracker from Claron Technology Inc., Toronto, ON, Canada. The MicronTracker was chosen to represent an ultrasound scanner because it has a similar frame rate of 20 Hz, which introduces an image acquisition and processing delay of up to 50 ms. A Yaskawa Motoman Robot SIA5F from Yaskawa Canada, Inc., Mississauga, ON, Canada was used as a beating-heart simulator. The experimental setup is shown in Fig. 8.5 and a close up view of the surgical tool is shown in Fig. 8.4.

To begin designing a GPC system to control the surgical tool, an electromechanical model of the surgical robot is identified. This electromechanical model includes the voice coil actuator and the corresponding analog circuitry that converts the voltage setpoint to a current that drives the voice coil actuator. The voice coil actuator was modeled as that in [76], where relationship between the input current and the velocity of the voice coil actuator is

$$V = \left( \frac{1}{sL + R} \right) \left( \frac{K_t}{sJ + B} \right) \omega \quad (8.16)$$

The inductance  $L$  and resistance  $R$  of the voice coil are 1.05 mH and 3.5  $\Omega$ , respectively, and the back EMF gain  $K_t$  is 6.1 V/m. The parameters  $J$  and  $B$  were found to be -0.5264 and 16.2547 using least squares identification.

Next, consistent with past literature [30] the Motoman robot was programmed to move linearly in one direction in the same fashion as the heart – see Heart Position in Figs. 8.6-8.10. The Micron Tracker captured the motion of the Claron black and white optical markers that were attached to the robot arm and to the surgical tool. These markers will not be needed later when the system uses an ultrasound scanner to measure the motion. Each of the two methods of designing the GPC described in Section 8.1.1 are implemented. The control horizon was set to 3 and  $\lambda = 0.00001$ . A summary of the experimental results is given in Table 8.1.

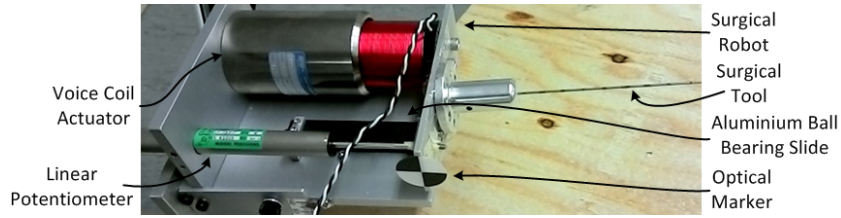


FIGURE 8.4: A close up view of the surgical tool. It is actuated by a voice coil. An optical marker is attached in order for the Micron tracker to measure its position.

First, the distance between the surgical tool and the heart is controlled to follow the surgeon's position. There is a 50 ms delay in the loop due to image acquisition and processing and the images are acquired at a rate of 20 Hz. The heart's motion is treated as a disturbance whose measurement is available after the time delay. The result when the surgeon's motion is set to zero is shown in Fig. 8.6, where the dashed blue line is the position of the simulated heart and the solid black line is the position of the surgical tool tip. The mean value of the position error is 12 mm and the integrated squared error (ISE)

$$ISE = \frac{1}{n} \sum \epsilon^2 \quad (8.17)$$

where  $\epsilon$  is the position error and  $n$  is the number of data points, is 205 mm<sup>2</sup>. The result when the surgeon's motion is a square wave with an amplitude of 3 mm and a frequency of 2 Hz is shown in Fig. 8.7, where the dashed blue line is the position of the simulated heart, the solid black line is the position of the surgical tool tip, and the dash-dotted black line is the surgeon's motion. The mean value of the position error is 8.9 mm and the ISE is 115 mm<sup>2</sup>. The errors are large because the system is not given any information about the disturbance (simulated heart motion) which has an amplitude of 20 mm. Because of the time delay, the surgical tool tip moves to correct for the heart's motion with a delay.

Second, the surgical tool tip is controlled to follow the combination of the estimated heart motion and the surgeon's motion. As a basis for comparison, the surgical tool was first controlled to follow the simulated heart motion under no delay using a proportional controller. The result is given in Fig. 8.8. It is evident from this figure that the voice

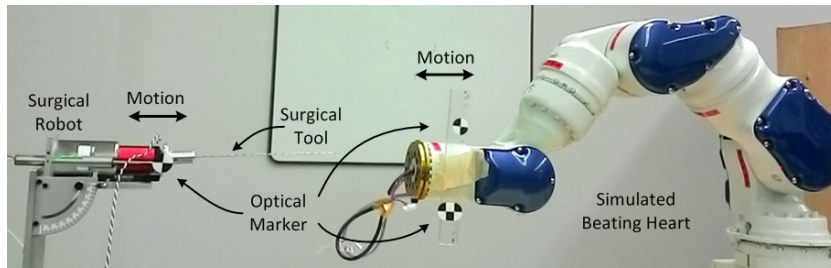


FIGURE 8.5: The experimental setup. The surgical tool is actuated by a voice coil actuator and the beating heart is simulated by an oscillating robotic arm.

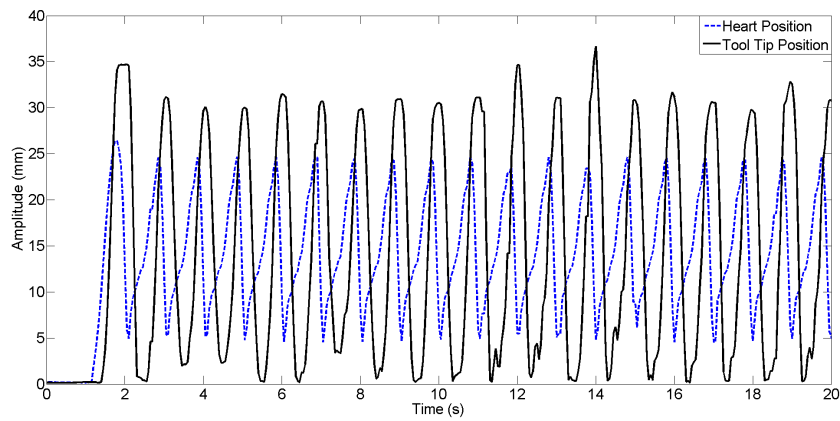


FIGURE 8.6: The result of controlling the surgical tool to keep a fixed distance between itself and the beating heart. In this case the surgeon's motion is set to zero. The diagram of this system is given in Fig. 8.2.

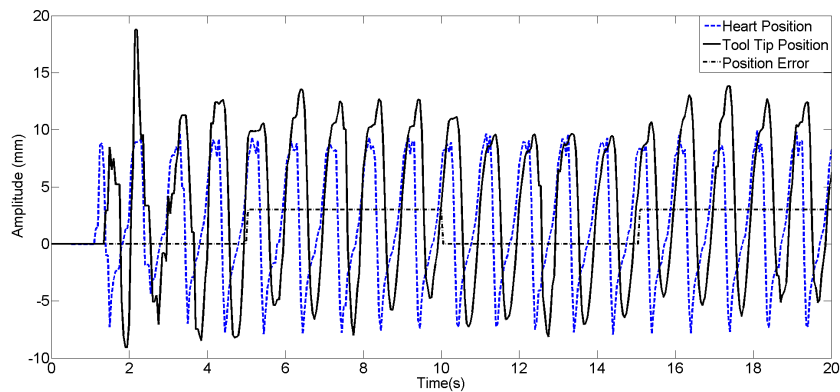


FIGURE 8.7: The result of controlling the surgical tool to keep a fixed distance between itself and the beating heart. In this case the surgeon's motion is a square wave with an amplitude of 3 mm and a frequency of 2 Hz. The diagram of this system is given in Fig. 8.2.

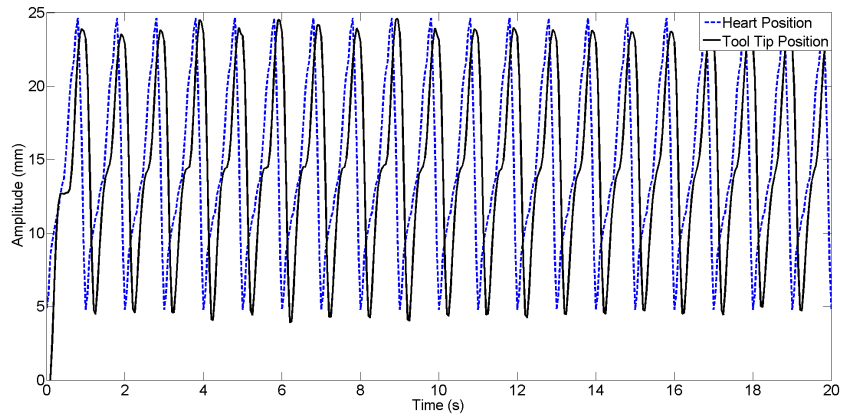


FIGURE 8.8: The result of controlling the surgical tool to follow the simulated heart motion under no delay using proportional control.

coil, under the low sampling rate of 20 Hz, follows the motion with a delay. Next, the delay and the GPC controller were returned to the system. As before, there is a 50 ms delay in the system due to image acquisition and processing before the position of the heart is known. For simplicity, the heart's motion is delayed by one heartbeat cycle and then used as a estimate of the current heart position.

Now the tracking error is the difference between the current and estimated heart motion and the GPC does not have to reject a large disturbance as in the previous case. The result when the surgeon's motion is set to zero is shown in Fig. 8.9 where the dashed blue line is the position of the simulated heart and the solid black line is the position of the surgical tool tip. The mean value of the position error is 8.1 mm and the ISE is 91 mm<sup>2</sup>. The result when the surgeon's motion is a square wave with an amplitude of 3 mm and a frequency of 2 Hz is given in Fig. 8.10 where the dashed blue line is the position of the simulated heart, the solid black line is the position of the surgical tool tip, and the dash-dotted black line is the surgeon's motion. The mean value of the position error is 8.1 mm and the ISE is 91 mm<sup>2</sup>. No additional error occurred when the surgeon's motion was added. These position errors are smaller than those in the previous method, showing the superiority of the second method.

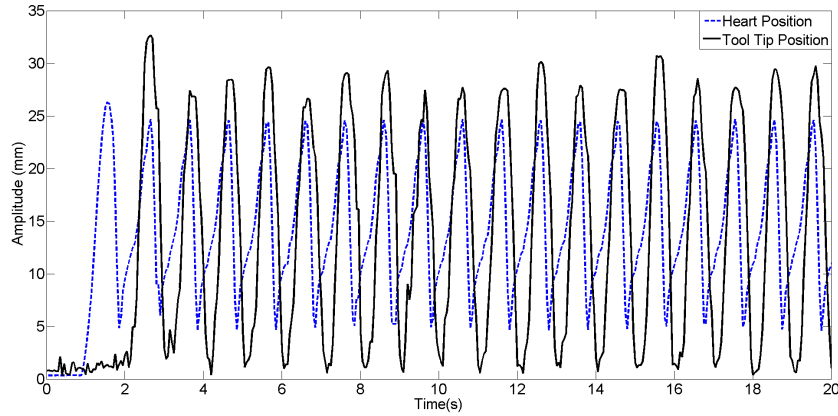


FIGURE 8.9: The result of controlling the surgical tool to follow the estimated heart position. In this case the surgeon's motion is set to zero. The diagram of this system is given in Fig. 8.3.

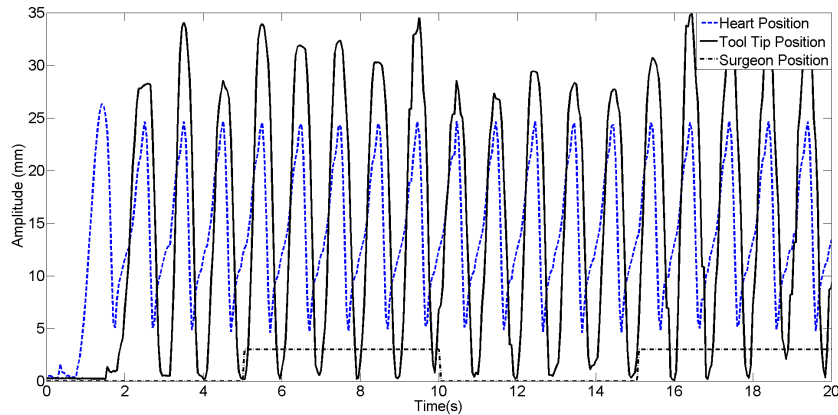


FIGURE 8.10: The result of controlling the surgical tool to follow the estimated heart position. In this case the surgeon's motion is a square wave with an amplitude of 3 mm and a frequency of 2 Hz. The diagram of this system is given in Fig. 8.3.

Surgeon's Motion	GPC Method I		GPC Method II	
	MAE (mm)	ISE (mm <sup>2</sup> )	MAE (mm)	ISE (mm <sup>2</sup> )
None	12	205	8.1	91
2 Hz, 3 mm Square Wave	8.9	115	8.1	91

TABLE 8.1: A summary of the experimental results.

### 8.3 Concluding Remarks

When developing a motion compensating control system, the heart's motion can be treated as a disturbance that the control system must reject, but this is difficult as the heart moves quickly with velocities up to 210 mm/s and accelerations up to 3800 mm/s<sup>2</sup>. In this chapter, a generalized predictive controller was implemented in two different configurations to make the surgical tool follow the summation of the heart's and surgeon's motion. The first treated the heart's motion as a disturbance and controlled the distance between the heart and surgical tool to follow the surgeon's motion. The second method estimated the heart's motion based on previous motion and controlled the surgical tool to follow the combination of the surgeon's motion and the estimated heart motion. Because a large disturbance was not present in the second GPC method, the mean error was reduced to 8.1 mm from 12 mm in the first GPC method. In closing, this chapter shows that GPC can be used to create a robot-assisted beating-heart surgical system because it can account for both the image acquisition and processing delay and the large disturbance created by the beating heart.

## Chapter 9

# Ultrasound-guided Generalized Predictive Control

In Chapter 8, two configurations for generalized prediction control (GPC) based motion compensation were presented. GPC is different from the previously presented controllers because it calculates the optimal control signal based on the current error between the system's input and output as well as estimated future errors. In the first configuration of the GPC controller presented in Chapter 8, the distance between the surgical tool tip and the POI was controlled to follow the surgeon's motion. The POI's motion was treated as a disturbance. In the second configuration, the surgical tool was controlled to follow the summation of the POI's and surgeon's motion. This method performed better than the first as an estimate of the POI's motion was included and was not simply treated as a disturbance. In this chapter, the surgical robot is controlled to follow the combination of the surgeon's and the POI's motion, but the control is performed at 100 Hz, whereas it was previously performed at 20 Hz. This control system is also

---

Portions of this chapter have been submitted to IEEE Robotics and Automation Letters as "Meaghan Bowthorpe and Mahdi Tavakoli. Generalized Predictive Control of a Surgical Robot for Beating-heart Surgery under Delay and Slowly-sampled Ultrasound Image Data."

performed with ultrasound guidance and a user task based on mitral valve annuloplasty is presented to determine whether the presented motion compensation algorithm actually helps the user perform a task while the POI is moving.

The remainder of this chapter is organized as follows. The challenges that must be overcome when designing the control system are discussed in Sec. 9.1. The chosen control method, generalized predictive control, is discussed in Sec. 9.2. The control system is implemented in Sec. 9.3. Finally, a surgical task based on mitral valve annuloplasty is presented in Sec 9.4 and the conclusion is presented in Sec. 9.6.

## 9.1 Surgical Robot Control System

As discussed previously, it is too difficult for a surgeon to operate on a beating heart, but a surgical robotic system can assist the surgeon by compensating for the POI's motion. *The key is to control the distance between the surgical robot and the POI to follow the surgeon's motion.* This work will focus on image-based sensors, more specifically ultrasound images, as we propose to design a surgical system for procedures performed inside or outside the heart. Because ultrasound images were chosen, the main issues that need to be addressed by the surgical robot feedback control system are:

- *Delay in image data acquisition and processing:* If left uncompensated for, this delay may destabilize the surgical robot control loop, possibly resulting in collisions between the surgical robot and the POI.
- *Slow sampling of image data:* The slowly sampled position measurements from the images must first be upsampled before being used in the surgical robot's feedback control loop to ensure a smooth response and to take advantage of the robot's faster sampling rate.

## 9.2 Generalized Prediction Control

In generalized predictive control, the control signal is calculated by minimizing the difference between the estimated system output (position) and the given desired reference signal over a specified horizon while limiting the control effort [74]. Therefore, a model of the robot is required to estimate future outputs based on current inputs.

In order to design a GPC law, we begin with a controlled auto-regressive integrated moving average (CARIMA) model to describe the robot dynamics:

$$A(z^{-1})y[kt] = B(z^{-1})u[(k-1)t]z^{-d} + \frac{C(z^{-1})}{\Delta}e[kt] \quad (9.1)$$

In the above,  $z^{-1}$  is the backward shift operator,  $\Delta = 1 - z^{-1}$ ,  $t$  is the sampling interval, and  $k$  is an integer. The current system output is  $y[kt]$ , the previous sampling interval's control signal (input) is  $u[(k-1)t]$ , and the current disturbance is  $e[kt]$ .  $A$ ,  $B$ , and  $C$  are polynomials of order  $n_a$ ,  $n_b$ , and  $n_c$  respectively.

$$A(z^{-1}) = 1 + a_1z^{-1} + a_2z^{-2} + \dots + a_{n_a}z^{-n_a} \quad (9.2a)$$

$$B(z^{-1}) = b_0 + b_1z^{-1} + b_2z^{-2} + \dots + b_{n_b}z^{-n_b} \quad (9.2b)$$

$$C(z^{-1}) = 1 + c_1z^{-1} + c_2z^{-2} + \dots + c_{n_c}z^{-n_c} \quad (9.2c)$$

The goal of GPC is to minimize the difference between the optimal prediction of the plant's future outputs given the current output, i.e.,  $\hat{y}[(k+j)t|kt]$  and the future reference signal values  $w[(k+j)t]$  while keeping the change in the control effort  $\Delta u[(k+j-1)t]$  small. The cost function is then

$$J(N_1, N_2, N_u) = \sum_{j=1}^{N_u} \lambda(j) \left[ \Delta u[(k+j-1)t] \right]^2 + \sum_{j=N_1}^{N_2} \delta(j) \left[ \hat{y}[(k+j)t|kt] - w[(k+j)t] \right]^2 \quad (9.3)$$

where  $N_1$  and  $N_2$  are the minimum and maximum costing horizons,  $N_u$  is the control horizon and is equal to  $N_1 - N_2$ , and  $\delta(j)$  and  $\lambda(j)$  are weighting factors. To estimate future values of the output  $\hat{y}[(k+j)t]$ , we start with the following Diophantine equation:

$$1 = E_j(z^{-1})\tilde{A}(z^{-1}) + z^{-j}F_j(z^{-1}) \quad (9.4)$$

where  $\tilde{A}(z^{-1}) = \Delta A(z^{-1})$ , and  $E_j(z^{-1})$  and  $F_j(z^{-1})$  are polynomials of degree  $j-1$  and  $n_a$ , respectively.  $E_j(z^{-1})$  and  $F_j(z^{-1})$  can be uniquely found given  $A(z^{-1})$ . Now multiply (9.1) by  $\Delta E_j(z^{-1})z^j$ , considering (9.4), and the white noise case where  $C(z^{-1}) = 1$ , we obtain

$$\hat{y}[(k+j)t] = F_j(z^{-1})y[kt] + E_j(z^{-1})e[(k+j)t] + E_j(z^{-1})B(z^{-1})\Delta u[(k+j-d-1)t] \quad (9.5)$$

Assuming the best estimate of future errors  $e[(k+j)t]$  is zero we obtain:

$$\hat{y}[(k+j)t|kt] = F_j(z^{-1})y[kt] + G_j(z^{-1})\Delta u[(k+j-d-1)t] \quad (9.6)$$

where  $G_j(z^{-1}) = E_j(z^{-1})B(z^{-1})$ .

Separating the upcoming and past changes in the control signal  $\Delta u$ , and changing to vector form, (9.6) can be written as

$$\mathbf{y} = \mathbf{G}\mathbf{u} + \mathbf{F}(z^{-1})y[kt] + \mathbf{G}'(z^{-1})\Delta u[(k-1)t] = \mathbf{G}\mathbf{u} + \mathbf{f} \quad (9.7)$$

where

$$\mathbf{y} = \begin{bmatrix} \hat{y}[(k+d+1)t|kt] \\ \hat{y}[(k+d+2)t|kt] \\ \vdots \\ \hat{y}[(k+d+N_u)t|kt] \end{bmatrix} \quad (9.8)$$

$$\mathbf{G} = \begin{bmatrix} g_0 & 0 & \dots & 0 \\ g_1 & g_0 & \dots & 0 \\ \vdots & \vdots & \vdots & \vdots \\ g_{N_u-1} & g_{N_u-2} & \dots & g_0 \end{bmatrix} \quad (9.9)$$

$g_0, g_1, \dots, g_{N_u-1}$  are the coefficients of  $G_j$ ,

$$\mathbf{u} = \begin{bmatrix} \Delta u[kt] \\ \Delta u[(k+1)t] \\ \vdots \\ \Delta u[(k+N_u-1)t] \end{bmatrix} \quad (9.10)$$

$$\mathbf{G}'(z^{-1}) = \begin{bmatrix} (G_{d+1}(z^{-1}) - g_0)z \\ (G_{d+2}(z^{-1}) - g_0 - g_1z^{-1})z^2 \\ \vdots \\ (G_{d+N_u}(z^{-1}) - g_0 - g_1z^{-1} - \dots - g_{N_u-1}z^{N_u-1})z^N \end{bmatrix} \quad (9.11)$$

and

$$\mathbf{F}(z^{-1}) = \begin{bmatrix} F_{d+1}(z^{-1}) \\ F_{d+2}(z^{-1}) \\ \vdots \\ F_{d+N_u}(z^{-1}) \end{bmatrix} \quad (9.12)$$

The cost function can be rewritten in vector form as:

$$J = (\mathbf{G}\mathbf{u} + \mathbf{f} - \mathbf{w})^T(\mathbf{G}\mathbf{u} + \mathbf{f} - \mathbf{w}) + \lambda \mathbf{u}^T \mathbf{u} \quad (9.13)$$

where

$$\mathbf{w} = \begin{bmatrix} w[(k+1)t] \\ \vdots \\ w[(k+N_u)t] \end{bmatrix} \quad (9.14)$$

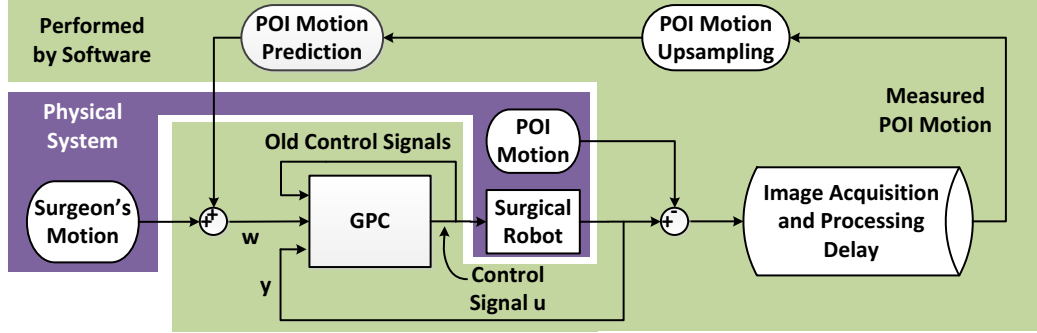


FIGURE 9.1: A model of the robot-assisted beating-heart surgical system where the surgical tool tip is being controlled to follow the combination of the estimated heart motion and the surgeon’s motion. The estimated heart motion is calculated from the heart’s motion in the previous heart beat.

From (9.13),  $\Delta u[kt]$  can be calculated as

$$\Delta u[kt] = K(\mathbf{w} - \mathbf{f}) \quad (9.15)$$

where  $\mathbf{K} = (\mathbf{G}^T \mathbf{G} + \lambda \mathbf{I})^{-1} \mathbf{G}^T$ ,  $\mathbf{I}$  is an identity matrix with the same size as  $\mathbf{G}$ ,  $\lambda$  is a weighting factor, and  $K$  is the first row of  $\mathbf{K}$ . For more details see [75].

### 9.3 Surgical Robot Control Algorithm

The configuration of the controller is shown in Fig. 9.1. The reference signal  $w$  is the sum of the surgeon’s motion and the estimated POI motion and the controlled variable  $y$  is the surgical tool’s position. In the figure, the darker section is the physical system that cannot be changed and the lighter section is performed by software and can be changed. To run this controller at 100 Hz, the POI’s motion, measured from the ultrasound images, is upsampled and then predicted the length of the horizon into the future to overcome the total delay caused by the image acquisition, processing, and upsampling.

### 9.3.1 POI Motion Measurement

The image processing method presented in this paper to locate the POI does not require any markers and is completed within one sample time at the image acquisition rate of 34 Hz. The image processing procedure is summarized in Fig. 9.2. Initially, a binary threshold is applied to convert the gray-scale images to black and white.

To begin, the surgical tool is found in each image. A Hough transform finds the longest straight line that forms an angle with the horizontal within a  $\frac{\pi}{4}$  radian angular arc – the surgical tool’s expected location – in the first image. To reduce the processing time of the remaining images, a region of interest (ROI) is created surrounding the determined location of the surgical tool. In the remaining images, least squares regression by OpenCV’s `fitline()` is used to identify the centre of the surgical tool’s shaft [77]. To lessen the computational burden, the ROI is down-sampled and only every third column and row of the ROI are analysed for candidate pixels. Fig. 9.3a shows the result of finding the tool. The ROI surrounding the tool shaft is marked by the green lines, the center of the tool shaft is given by the purple line, and the tool tip is shown by the blue dot.

The heart tissue is found in a similar manner. In the first image, a Hough transform identifies the longest line within a  $\frac{\pi}{4}$  radians angular arc perpendicular to the surgical tool shaft. A second ROI is created surrounding the heart tissue. In all subsequent images, the heart tissue is identified using OpenCv’s `fitline()`. Once again, to reduce the computation time, the image is down-sampled and only every third column and row are analysed for candidate pixels. Within every subsequent image, the candidate pixels on the upper edge of the heart tissue are identified and a straight line is fit through them. As the heart tissue moves continually, the ROI surrounding the heart tissue is updated after every image. Figs. 9.3b and 9.3c show the result of finding the heart tissue when the surgical tool and the heart tissue are not and are in contact, respectively. The ROI surrounding the heart tissue is marked by the light green lines, the edge of the heart

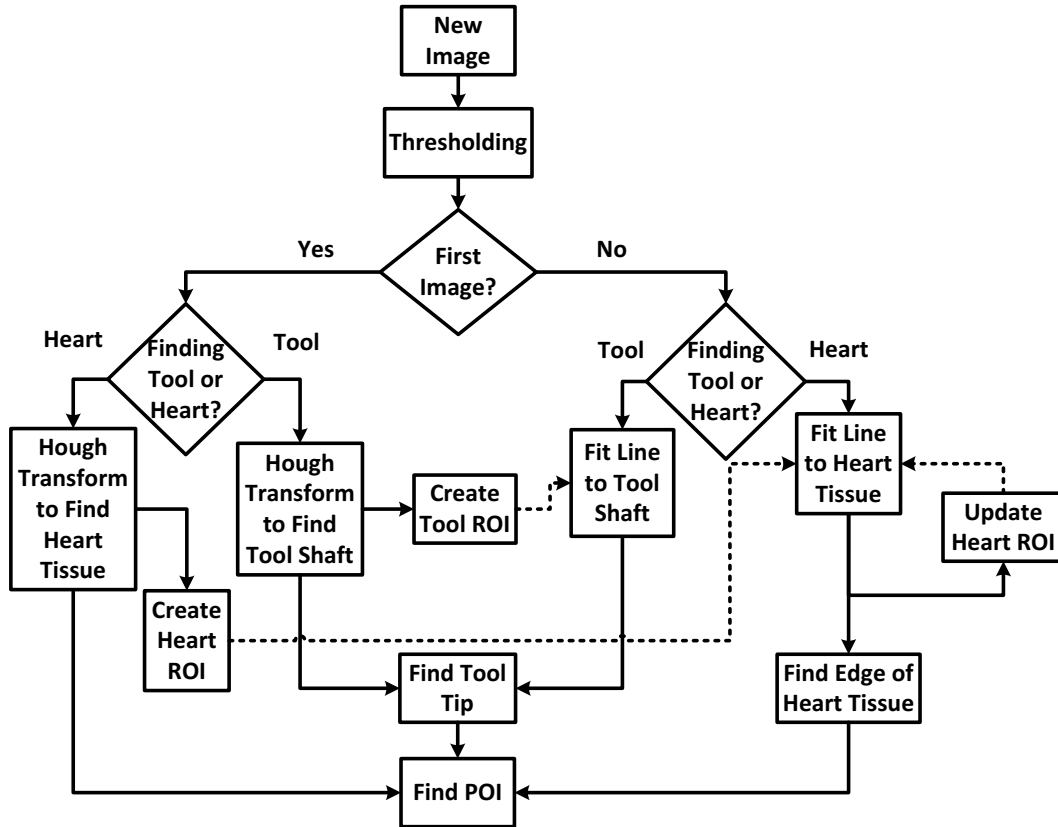


FIGURE 9.2: A flow chart of the image processing. Each image is thresholded to create a black and white image. Hough transforms are then used to locate the tool shaft and heart tissue in the first image. The ROIs are set and the tool tip and POI locations are found. Lines are then fit to the tool shaft and heart tissue in the remaining images, the edge of the heart tissue is found, the heart tissue ROI is updated, and the tool tip and POI locations are found.

tissue is given by the dark green line, and the centre line of the heart is given by the red line.

The location of the POI is found by extending the line through the surgical tool shaft and locating the first candidate pixel beyond the surgical tool’s tip – the heart tissue. However, a difficulty arises when the surgical tool tip makes contact with the heart tissue. In this case, it is not possible to identify the surgical tool’s tip as the surgical tool and the heart tissue appear as one object. When the surgical tool is touching the heart tissue, i.e., when the line marking the surgical tool tip intersects with the line

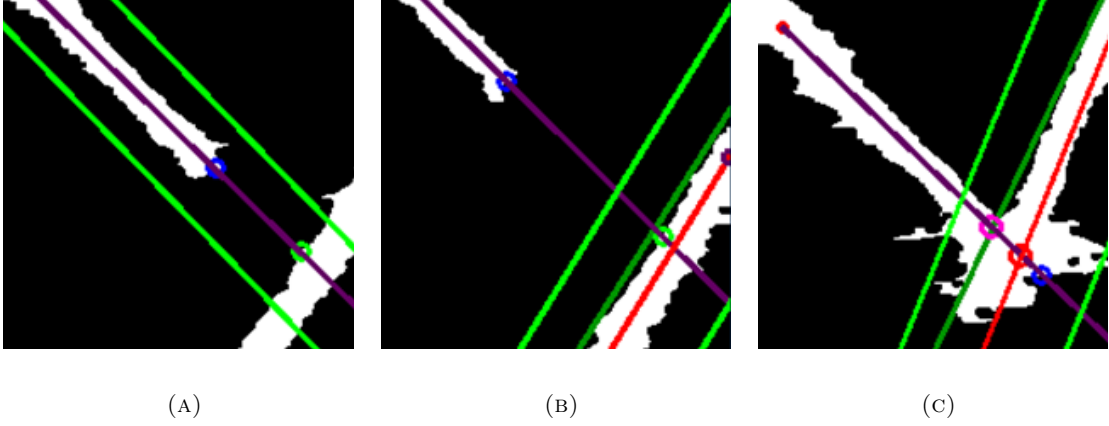


FIGURE 9.3: The result of the image processing required to find the surgical tool shaft and tip (a), and the heart tissue and the POI (b) and (c). The light green lines form the boundary of the ROI, the purple line identifies the surgical tool shaft, the blue dot shows the surgical tool tip in (a) and (b), the green dot shows the POI in (b), and the pink dot shows the surgical tool tip and POI in (c).

marking the heart tissue, the POI is identified by the intersection of the line marking the edge of the heart tissue and the line through the surgical tool shaft. The location of the POI when the surgical tool and the heart do not touch is the green dot in Fig. 9.3b and when they do touch the POI is the pink dot in Fig. 9.3c.

### 9.3.2 POI Motion Upsampling

After the POI's motion is measured from the ultrasound images, it is upsampled using cubic interpolation, which ensures that the upsampled trajectory and its first derivative are smooth. Consider the data points  $p_0$  and  $p_1$ , in between which the interpolation is to occur. One data point before  $p_0$  and one data point after  $p_1$  are required to calculate the slope at  $p_0$  and at  $p_1$ . Consequently, four data points, two of which are in the future with respect to the interval being interpolated, are required, which increases the time delay by the length of two samples at the slow sampling rate. The following equation calculates the interpolated data points:

$$p(n) = h_{00}(n)p_0 + h_{10}(n)m_0 + h_{01}(n)p_1 + h_{11}(n)m_1 \quad (9.16)$$

where  $m_0$  and  $m_1$  are the slopes at points  $p_0$  and  $p_1$ , respectively, and  $n$  is the interpolation variable, which is a vector with a length of one greater than the number of points to be interpolated and with evenly spaced values ranging from 0 and 1. When  $n$  equals 0 and 1, the result is  $p_0$  and  $p_1$ , respectively. The  $h$  coefficients are:

$$\begin{aligned}
 h_{00}(n) &= 2n^3 - 3n^2 + 1 \\
 h_{10}(n) &= n^3 - 2n^2 + n \\
 h_{01}(n) &= -2n^3 + 3n^2 \\
 h_{11}(n) &= n^3 - n^2
 \end{aligned} \tag{9.17}$$

### 9.3.3 POI Motion Prediction

Another issue to overcome is the non-negligible delay in data acquisition and processing and in upsampling the position of the POI. To address this, the POI's motion is modeled as a Fourier series and an extended Kalman filter is used to predict the POI future motion.

$$y(\mathbf{x}(t)) = c + \sum_{i=1}^m r_i \sin \theta_i(t) \tag{9.18}$$

In the above, the state vector is defined as  $\mathbf{x}(t) = [c(t), r_i(t), \omega(t), \theta_i(t)]^T$ ,  $i = 1, \dots, m$ ,  $m$  is the number of harmonics,  $\theta_i(t) = i \int_0^t \omega(\tau) d\tau + \phi_i(t)$ , and  $t$  is the current time. The coefficients in (9.18) can vary with time to account for cycle-to-cycle heart motion variation [30].

The state space model (9.19) evolves through random walk, where the offset  $c$ , the sine wave coefficients,  $r_i$ , and the frequency  $\omega$  are assumed to remain constant. These values are then updated by the EKF proportionally to the error between the predicted and actual measurement, except for the frequency,  $\omega$ , which is replaced by the value measured directly from the past POI motion.

$$\begin{aligned}
 \mathbf{x}(t + \Delta t) &= \mathbf{L}(\Delta t)\mathbf{x}(t) + \mu(t) \\
 z(t) &= y(\mathbf{x}(t)) + v(t)
 \end{aligned} \tag{9.19}$$

Here,  $\mathbf{L}(\Delta t)$  is a  $[2m + 2] \times [2m + 2]$  matrix:

$$\mathbf{L}(\Delta t) = \left[ \begin{array}{c|ccc} \mathbf{I}_{m+1} & & & 0 \\ \hline & 1 & & \\ & \Delta t & 1 & \\ \mathbf{0} & 2\Delta t & 0 & 1 \\ & \vdots & & \ddots \\ & m\Delta t & & 1 \end{array} \right] \quad (9.20)$$

The estimated covariance matrix  $\mathbf{P}(t + \Delta t|t)$  is a  $[2m + 2] \times [2m + 2]$  diagonal matrix with  $[0.001, 0.1/1, 0.1/2, \dots, 0.1/l, 0.1, 0.2_{1 \times m}]$  along the diagonal, the process noise covariance matrix  $\mathbf{Q}$  is a  $[2m + 2] \times [2m + 2]$  diagonal matrix with 0.0001 along the diagonal, and the observation noise covariance matrix  $\sigma_R^2$  is 0.01. The Kalman gain  $\mathbf{K}$  and  $\mathbf{P}(t + \Delta t|t)$  are calculated as

$$\mathbf{P}(t + \Delta t|t) = \mathbf{L}(\Delta t)\mathbf{P}(t|t)\mathbf{L}(\Delta t)^T + \mathbf{Q} \quad (9.21a)$$

$$S = \sigma_R^2 + \mathbf{H}\mathbf{P}(t + \Delta t|t)\mathbf{H}^T \quad (9.21b)$$

$$\mathbf{K} = \mathbf{P}(t + \Delta t|t)\mathbf{H}^T S^{-1} \quad (9.21c)$$

The state and covariance matrices are updated as follows:

$$\hat{\mathbf{x}}(t + \Delta t|t + \Delta t) = \mathbf{L}(\Delta t)\hat{\mathbf{x}}(t|t) + \mathbf{K}(z(t + \Delta t) - y(\mathbf{L}(\Delta t)\hat{\mathbf{x}}(t|t)))$$

$$\mathbf{P}(t + \Delta t|t + \Delta t) = (\mathbf{I} - \mathbf{K}\mathbf{H})\mathbf{P}(t + |\Delta t|t) \quad (9.22a)$$

In the above,  $\mathbf{H}$  is a  $[2m + 2] \times [1]$  matrix:

$$\mathbf{H}^T(\Delta t) = \left( \frac{\partial h}{\partial \mathbf{x}} \right)^T \bigg|_{\hat{\mathbf{x}}(t+\Delta t|t) = \mathbf{L}\hat{\mathbf{x}}(t|t)} = \begin{bmatrix} 1 \\ \sin \hat{\theta}_1(t + \Delta t|t) \\ \vdots \\ \sin \hat{\theta}_m(t + \Delta t|t) \\ 0 \\ \hat{r}_1(\Delta t|t) \cos \hat{\theta}_1(t + \Delta t|t) \\ \vdots \\ \hat{r}_m(\Delta t|t) \cos \hat{\theta}_m(t + \Delta t|t) \end{bmatrix} \quad (9.23)$$

To predict  $j$  future points ahead, the estimated state matrix  $\hat{\mathbf{x}}$  is multiplied by the update matrix  $\mathbf{L}\Delta(t)$  a total of  $j$  times,  $\hat{\mathbf{x}}(t+j\Delta t|t+\Delta t) = \mathbf{L}^j \hat{\mathbf{x}}(t+\Delta t|t)$ . The predicted position is then calculated from the predicted state and (9.18).

## 9.4 Experimental Results

The experimental setup shown in Fig. 9.4 uses a 6 MHz 4DL14-5/38 linear 4D transducer connected to a SonixTouch ultrasound scanner (SonixTouch from Ultrasonix, Richmond, BC, Canada) as the image sensor, which has a low frame rate of 34 Hz. The depth of the images was 4.5 cm. The ultrasound images were collected from the ultrasound scanner using a DVI2USB 3.0 frame grabber (Epiphan, Ottawa, ON, Canada). The entire image acquisition, processing delay and upsampling delay is 170 ms. A custom-built mechanical cam (simulated heart), based on the motion trajectory collected from the movement of a point on the side wall of the heart in a series of clinical ultrasound images of a patient's beating heart generated the POI motion. The single degree-of-freedom (DOF) surgical tool (surgical robot) is actuated by a voice coil motor (NCC20-18-020-1X from H2W Technologies Inc., Santa Clarita, CA, USA). To verify the results, real-time position measurements of both the mechanical cam and the robot were collected

$$I = \frac{-6.764 \times 10^{-5} - 0.0002029z^{-1} - 0.0002029z^{-2} - 6.764 \times 10^{-5}z^{-3}}{1 - 0.8457z^{-1} - 0.8039z^{-2} + 0.6469z^{-3}}\theta \quad (9.24)$$

---

from two potentiometers (LP-75FP-5K and LP-30FP-1K from Midori America Corp., Fullerton, CA, USA).

To implement the GPC system, an electromechanical model of the surgical robot composed of the voice coil actuator and the corresponding analog current drive circuitry is identified. The voice coil actuator was modeled as in [76] where the relationship between the input current,  $I$ , and the position,  $\theta$  of the voice coil actuator is

$$I = \left( \frac{1}{sL + R} \right) \left( \frac{K_t}{sJ + B} \right) \left( \frac{1}{s} \right) \theta \quad (9.25)$$

The inductance  $L$  and resistance  $R$  of the voice coil are 1.05 mH and 3.5  $\Omega$ , respectively, and the back EMF gain  $K_t$  is 6.1 V/m. The parameters  $J$  and  $B$  were found to be -0.5264 and 16.2547 using least squares identification. Discretized to 10 ms, the robot's transfer function between the input current and the output position is given in (9.24). The weighting factors  $\lambda(j)$  and  $\delta(j)$  were set to 0.00003 and 1, respectively. The delay,  $d$  was 2 samples and the control horizon,  $N_u$ , was 5 samples.

For each trial, the heartbeat motion has a peak-to-peak amplitude of 10 mm and a period of 64 bpm (1.07 Hz). Three error metrics are calculated for each trial: the mean absolute error (MAE) is  $\frac{\sum |error|}{l}$ , where  $l$  is the number of data points in the sample, the integral squared error (ISE) is  $\frac{\sum (error)^2}{l}$ , and the peak error is the largest error at a single point in time. The results from each of the trials are summarized in Table 9.1.

## 9.5 Surgical Task

When the mitral valve is not shaped properly, blood may flow backwards through the heart making each beat less efficient. More than 300,000 people undergo mitral valve annuloplasty – a reconstructive procedure to fix the leaky valve – each year worldwide [71].

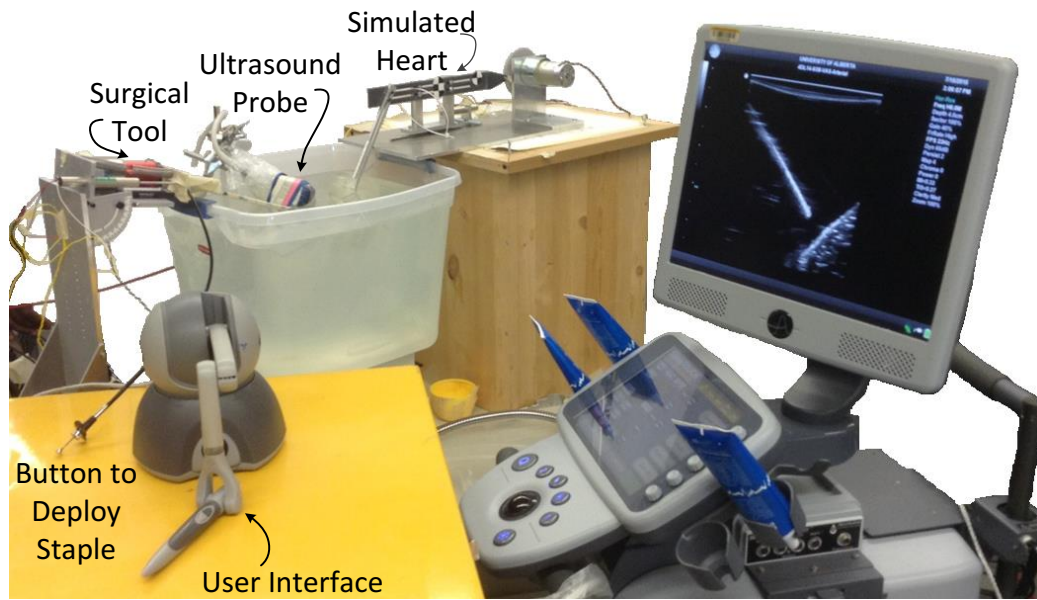


FIGURE 9.4: The experimental setup.

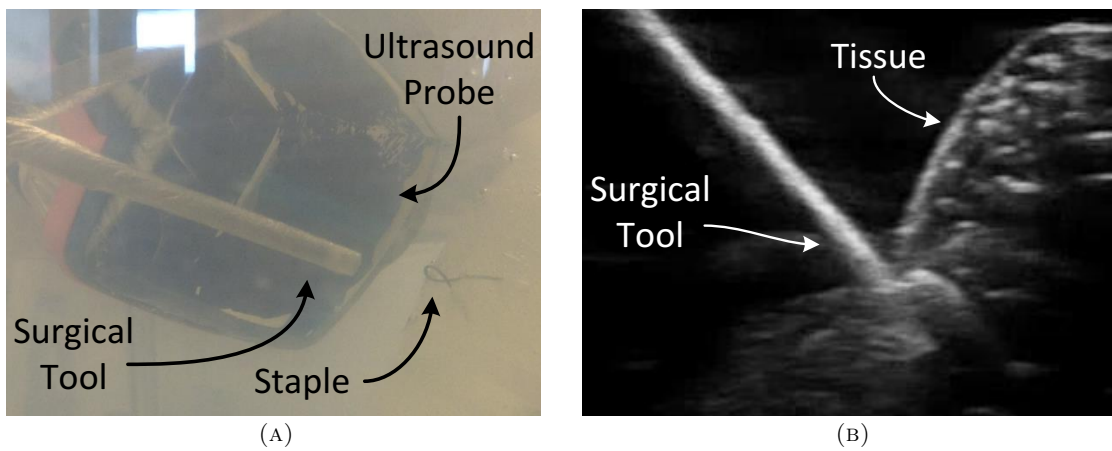


FIGURE 9.5: (a) A successfully deployed staple. (b) An example of using excessive force when deploying a staple.

The surgical task presented here simulates deploying a staple to secure an annuloplasty ring onto the mitral valve. This procedure is explained in more detail in Sec. 3.1.2. If securing this annuloplasty ring could be performed while the heart is still beating, the effectiveness of the newly reshaped valve could be evaluated immediately. This user study was approved by the University of Alberta's Research Ethics Office #Pro00055825.

In this user study, each participant deploys the staple into moving heart tissue. The participant sets the desired position of the surgical tool through teleoperation by moving the stylus of a PHANTOM Omni user interface (Geomagic, Cary, NC, USA). The heart tissue is represented by a piece of soft plastic visible under ultrasound and is mounted on the mechanical cam, which is the simulated beating heart. The participant views the scene on the ultrasound screen. The participant uses a button that deploys the staple using his or her other hand. A successfully deployed staple is shown in Fig. 9.5a.

This task is completed with and without motion compensation. For these trials, the heart motion was divided into two halves: the upper half where the heart tissue was closest to the surgical tool and the lower half where it was furthest away – this was where the participant was told to deploy the staple. This prevented the participant from simply waiting until the heart came towards the surgical tool to deploy the staple as this would have made the task too easy and not representative of real surgical maneuvers. Each participant was also instructed not to press the tool into the tissue when deploying the staple.

Each participant's pre-trial training included successfully deploying the staple three times with motion compensation. They then practiced with no compensation until they felt comfortable with the system. Each participant completed 10 trials: 5 with motion compensation and 5 without. The trials alternated between the two control conditions beginning with motion compensation. If the surgical tool left an indent in the phantom tissue when the staple was deployed or if the staple was deployed in the upper half of the heart beat when the surgical tool was closest to the surgical tool (see Fig. 9.5b), the trial was counted as a failure.

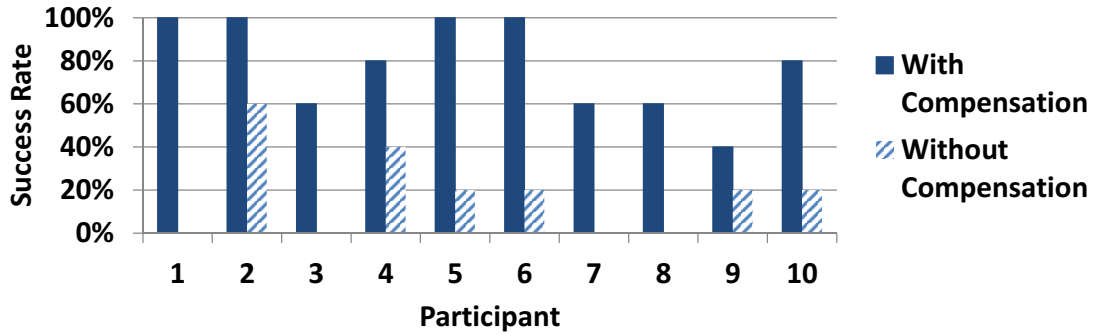


FIGURE 9.6: The rate of successful deployment of the staple for each participant.

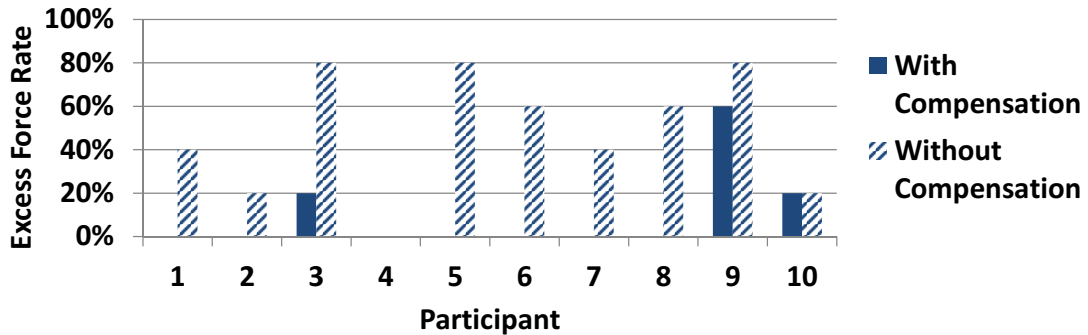


FIGURE 9.7: The rate of the use of excessive force for each participant.

The trials included 10 participants who were not surgeons (2 females and 8 males). The following are the results. Without motion compensation, the staple was successfully deployed in 18% of the trials and excessive force was used in 48% of the trials. With motion compensation, the success rate was 78% and the use of excessive force was reduced to 10% of the trials. The success rate of each participant is given in Fig. 9.6 and the rate of the use of excessive force is given in Fig. 9.7.

To compare the success rates, we used a two-tailed *t-test* and obtained the probability of the null hypothesis  $\mu_1 = \mu_2$  for the 10 trials [72]. The probability of the results assuming the null hypothesis for the success of the staple deployment with and without

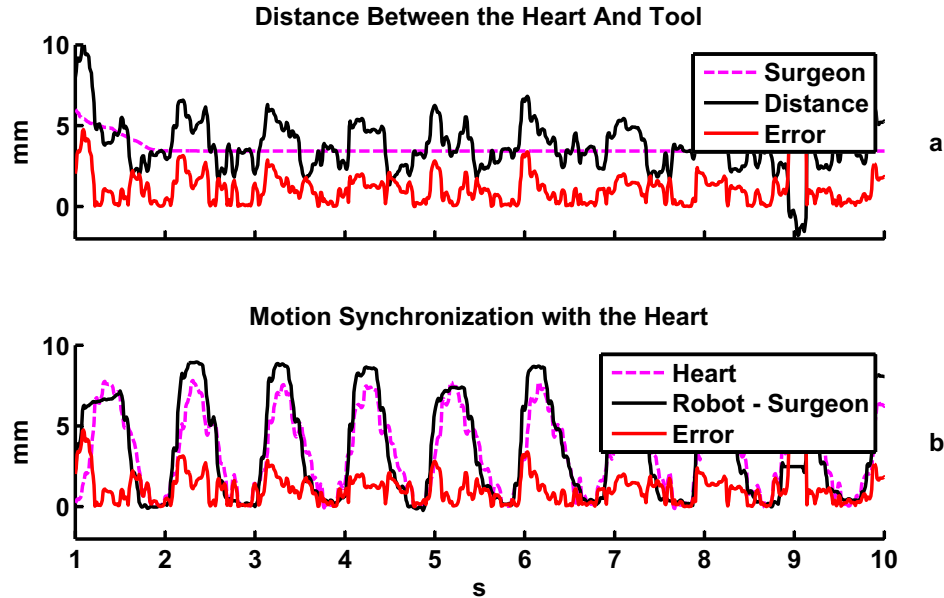


FIGURE 9.8: The result when motion compensation is provided. In case (a), the dashed pink line is the user’s motion, the solid black line is the distance between the surgical tool tip and the heart tissue, and the red line is the error between these two. Case (b) shows the motion synchronization. Here, the surgeon’s motions have been subtracted from the surgical tool tip’s motion leaving the POI following portion of the surgical tool tip’s motion – the solid black line. The heart’s motion is the dotted pink line and the error between the two is the red line.

compensation was  $2 \times 10^{-5}$  and for the use of excess force with and without compensation was 0.002. Since these figures are less than 0.05, these results indicate that there was a significant difference between providing and not providing motion compensation with respect to both the successful deployment of the staple and the use of excessive force.

When motion compensation was provided, it was easier for the user to move the surgical tool towards the moving heart tissue. The user’s motions for this case creates the pink line in Fig. 9.8a. The user’s motion simply moves the surgical tool tip towards the heart tissue. The solid black line in this figure is the resulting distance between the surgical tool tip and the POI and the solid red line is the error. Part (b) of Fig. 9.8 shows the result of the motion compensation. Here, the surgeon’s motion has been subtracted from the surgical tool tip’s motion to remove the offset between the surgical tool tip

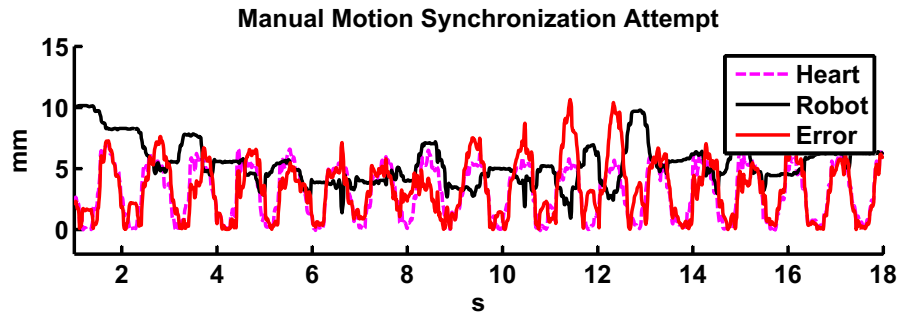


FIGURE 9.9: The result when no motion compensation is provided. Here the user tries to manually compensate for the heart’s motion. The surgical tool tip’s motion is the solid black line, the heart’s motion is the dotted pink line and the error between the two is the red line.

and the heart tissue – the solid black line. The POI’s motion is given by the dashed pink line and the error is given by the solid red line. The MAE tracking error when motion compensation is provided is 1.27 mm, the ISE tracking error is  $3.17 \text{ mm}^2$ , and the absolute value of the peak tracking error is 7.18 mm. It is much harder for the user to follow the POI’s motion when no motion compensation is provided. Fig. 9.9 shows the surgeon’s motion – the solid black line and the POI’s motion – the dashed pink line. It is quite obvious that the errors are quite large – the solid red line. The MAE tracking error when motion compensation is not provided is 3.03 mm, the ISE tracking error is  $15.59 \text{ mm}^2$ , and the absolute value of the peak tracking error is 10.16 mm.

The average tracking error reported in this work, 1.27 mm, is similar to those reported in the literature. Sub-millimetre errors were reported when a 500 Hz camera measured the position of the POI and the time delay was limited to one sample time in [24]. The use of pre-recorded data resulted in average errors as low as 0.669 mm and peak errors as large as 4.3 mm in [36]. However, this method is not viable in real-time. The use of motion compensation after the heart is stabilized by a mechanical stabilizer resulted in small errors of 0.4 and 0.8 mm in the  $x$  and  $y$  directions and a peak error of 2 mm in the  $y$ -direction in [5]. However, this method does not let the heart beat freely. Finally, an average and peak error of 0.97 mm and 3.26 mm respectively was reported in [30] where

Motion Compensation	MAE (mm)	ISE (mm <sup>2</sup> )	Peak Error (mm)
Yes	1.27	3.17	7.18
No	3.03	15.59	10.16

TABLE 9.1: A summary of the experimental results.

the POI motion was measured from ultrasound images. A similar user task performed with a hand-held motion compensating surgical tool reported a success rate of 74% when motion compensation was provided and only 32% when motion compensation was not provided [31].

## 9.6 Concluding Remarks

This chapter presents an image processing and GPC-based control system for ultrasound-guided robot-assisted beating-heart surgery for procedures such as mitral valve annuloplasty. As the position of the heart is measured from ultrasound images that are collected at a slow sampling rate, the position trajectory of the POI is first upsampled to 100 Hz. To overcome the time delay caused by ultrasound image acquisition and processing, the POI motion trajectory is predicted ahead to the current time using an EKF. To show the efficacy of this system, user trials simulating deploying a staple for mitral valve annuloplasty were conducted. The results indicate that the improvement in the success rate and use of excessive force when motion compensation is provided is statistically significant.

## Chapter 10

# Conclusions and Future Work

This thesis develops control methods for ultrasound-guided robot-assisted beating-heart surgery. The control systems developed may also compensate for physiological motion affecting procedures such as radiation therapy. The main challenges in developing such a system are: the slow sampling rate of the POI's motion collected from ultrasound images, the image acquisition and processing delay, and the heart's fast beating motion. The control methods presented in this thesis can be divided into two categories: predictive feedback control and prediction-based control. In the first, the delay is compensated for within the predictive feedback controller, whereas in the second, the delay is first compensated for by prediction and then added to the setpoint of a feedback controller.

The first controller presented in Chapter 4 is a modified Smith predictor that compensates for the time delay within the feedback control loop and is classified as a predictive feedback controller. The experimental portion of this chapter was performed in the Harvard Biorobotics Lab at Harvard University under the supervision of Dr. Howe. Ultrasound imaging was used to determine the location of the tool tip and the POI. Hence, both measurements were delayed. In this case, the distance between the POI and the surgical tool tip,  $D_{RH}$ , was controlled to follow the surgeon's motion that was collected in real-time without a delay from the surgeon's console. The distance was upsampled using cubic interpolation and a zero-order-hold. The POI's motion was predicted ahead

to the current time based on the POI motion from the previous heart beat cycle, based on an EKF, or by temporally adjusting the period of the motion from the previous heart beat cycle based on the heart beat frequency estimated by the EKF. The best tracking was obtained with cubic interpolation and temporally aligning the POI's motion from the previous heart beat cycle based on the frequency estimated by the EKF.

The Smith predictor design was improved in Chapter 5 by subtracting the estimated POI motion inside the inner feedback loop. Previously, the POI's motion was treated as a disturbance and was not included in the estimate of the current output (the inner feedback loop). Whereas in this Smith predictor configuration, the predicted POI's motion was included in the estimate of the current output. The experimental portion of this chapter was performed using a Micron Tracker, which has an image acquisition and processing delay similar to that of an ultrasound scanner. The system was tested using both a zero-order-hold and cubic interpolation to increase the sampling rate of the slowly sampled data collected from the ultrasound images. It is shown that the use of cubic interpolation reduces the tracking errors but increases the delay.

The two previous Smith predictor designs as well as a proportional controller are compared in Chapter 6. In this case, the proportional controller does not compensate for the time delay within the feedback loop. Instead, the POI motion is predicted before being added to the setpoint and thus this controller is considered a prediction-based controller. Another difficulty explored in this chapter is whether the transformation matrix between the imaging and the robot's frame of reference is available. The proportional controller assumes the transformation matrix between the image frame and robot frame is available such that the POI's position measurements can be transformed into the robot frame. In this case, the POI's position measurements are upsampled and predicted ahead to overcome the delay. Then, a proportional controller is used to ensure that the distance between the robot and the POI follows the physician's motion. When the transformation is not available, however, the distance between the POI and the robot is measured. In this case, the POI's motion is calculated from the robot's position and the upsampled distance measurements. Later, a Smith predictor is used as the feedback control loop.

Two different configurations are proposed; the first adds the predicted POI motion to the surgeon's motion to form a new setpoint (as in Chapter 4) and the second adds the predicted POI motion into the inner feedback loop to reflect where the POI's actual motion is added into the system (as in Chapter 5). As expected, the second method, which adds the predicted POI motion to the inner feedback loop, performs better than the first. When the image to robot frame transformation is available, the proportional controller performs better than the second Smith predictor.

In Chapter 7, the experimental setup is further tested by asking human participants to perform a task using the surgeon's console. This task simulated the deployment of a staple for mitral valve annuloplasty. The participants were asked to complete the task with and without motion compensation. As proportional control performed better in the previous chapter, it was also used in this chapter. The task was performed under ultrasound guidance. The participants successfully deployed the staple 64% of the time with motion compensation and only 28% of the time without motion compensation. The results of the trials indicate that the improvement in the success rate when motion compensation is provided to participants is statistically significant. The success rate when motion compensation was not provided was aided by the fact that the participant did not strictly need to follow the heart's motion to successfully deploy the staple. Rather, the participant could simply move the surgical tool to the furthest point in the heart's trajectory so the two came into contact once every beat. They then deployed the staple at the correct moment. This method was successful in this case; however, this method would not be successful for more complicated surgical procedures where the surgical tool must remain in contact with the heart for any length of time.

The controllers presented up to this point have been based on the error between the setpoint and the output from the previous sample time. Another method is to consider the current error and estimated future errors as well. This is possible if the future setpoint values are known or can be estimated. GPC considers the current and estimated future errors when calculating the control signal. In Chapter 8, two configurations of GPC are presented. The first controls the distance between the surgical tool tip and

the POI,  $D_{RH}$ , to follow the surgeon's motion. The second controls the surgical tool tip to follow the combination of the surgeon's and the estimated POI motion. In order to predict the future errors, the model of the surgical tool was identified. The second method performed better as the POI motion was treated as a disturbance in the first method.

The generalized predictive control scheme was then furthered in Chapter 9. As controlling the surgical tool to follow the combination of the POI's and the surgeon's motion performed better than treating the POI motion as a disturbance, only this second configuration was tested. The improvements included in this chapter are: measuring the surgical tool's real-time position from the robot's encoders instead of measuring the surgical tool's delayed position from the image data, and upsampling the POI's motion so that the controller could run at 100 Hz instead of 20 Hz. The POI's motion was also measured from ultrasound images in this chapter as compared to being measured with a Micron Tracker in the previous chapter. This negated the need for external markers. A user study similar to that of Chapter 7 was performed. However, the participants were told to deploy the staple in the lower half of the POI's motion. This no longer allowed the participant to simply wait for the POI to come to the surgical tool and deploy the staple successfully without motion compensation as was previously possible. The result was that the success rate improved to 78% with motion compensation and decreased to 18% without motion compensation as compared to Chapter 7.

## 10.1 Future Work

The following research can be performed in the future to improve this robot-assisted beating-heart surgical system.

- Force control:
  - Force control can be used for motion compensation when the surgical tool and the heart are in contact. The delay involved in collecting force measurements

is typically shorter than the image acquisition and processing delay. Hence, it may be easier to compensate for the POI's motion using force control when the surgical tool and the heart are in contact. However, position control is necessary when the surgical tool and the heart are not in contact, e.g., the initial portion of the surgical procedure. A controller that switches between these two control schemes depending on whether or not the surgical tool is in contact with the heart may provide better motion compensation.

- To perform force control, a force sensor must be attached to the surgical tool. The development of such a sensor is not trivial, as it must be either inexpensive and disposable or able to withstand the high temperatures and pressures when being sanitized.
- The addition of ECG and other biological signals:
  - These signals provide information about the upcoming heart beat. They can improve the estimation of the heart's current position as well as predict when an irregular heart beat is about to occur.
  - The ECG is a recording the electrical activity of the heart caused by the heart muscle depolarization. It contains information about the timing of the heart beats and can help to improve prediction of the POI's motion. Parsing this signal in real-time to determine which section of the heart beat cycle the heart is currently undergoing is difficult as the height of the signal's peaks may change over time.
  - The blood pressure inside the heart can also be used to help predict the motion of the POI.
- 3D tracking:
  - Our system is currently designed for one dimensional tracking. This is sufficient for some surgical procedures, but others require three dimensional tracking. New image processing methods will need to be developed to track the POI in three dimensions. In addition, the configuration of the surgical

tool will need to be modified to allow motion in three dimensions. The control systems presented in this thesis can then be extended to control each dimension of the surgical tool's motion.

- Safety features:
  - The heart's motion is quasi-periodic and irregular heart beats may occur. The use of ECG and biological signals can predict an upcoming irregular heart beat. A safe operating mode can be incorporated into the system to move the surgical tool away from the heart tissue so that the heart tissue is not punctured if the motion compensation fails during the irregular heart beat.

# Bibliography

- [1] A. Alwan. Global status report on noncommunicable diseases 2010. *World Health Organization*, 2011.
- [2] M.F. Newman, J.L. Kirchner, B.Phillips-Bute, V. Gaver, H. Grocott, R. H. Jones, D.B. Mark, J.G. Reves, and J.A. Blumenthal. Longitudinal assessment of neurocognitive function after coronary-artery bypass surgery. *New England Journal of Medicine*, 344(6):395–402, 2001.
- [3] G.L. Reed, D.E. Singer, E.H. Picard, and R.W. DeSanctis. Stroke following coronary-artery bypass surgery. A case-control estimate of the risk from carotid bruits. *The New England Journal of Medicine*, 319:1246–1250, 1988.
- [4] M. Bowthorpe and M. Tavakoli. Advances towards beating heart surgery. In Frederick T. Hawthorne, editor, *Minimally Invasive Surgery: Evolution of Operative Techniques, Safety & Effectiveness and Long-Term Clinical Outcomes*, pages 135–158. Nova Science Publishers, 2014.
- [5] T. Ortmaier, M. Groger, D.H. Boehm, V. Falk, and G. Hirzinger. Motion estimation in beating heart surgery. *IEEE Trans. on Biomedical Engineering*, 52(10):1729–1740, 2005.
- [6] D.T. Kettler, R.D. Plowes, P.M. Novotny, N.V. Vasilyev, P.J. del Nido, and R.D. Howe. An active motion compensation instrument for beating heart mitral valve surgery. In *IEEE/RSJ Int. Conf. on Intelligent Robots and Systems*, pages 1290–1295, 2007.

- [7] S.G. Yuen, D.T. Kettler, and R.D. Howe. Robotic motion compensation for beating intracardiac surgery. In *Int. Conf. on Control, Automation, Robotics and Vision*, pages 617–622, 2008.
- [8] M. Bowthorpe, M. Tavakoli, H. Becher, and R. Howe. Smith predictor based control in teleoperated image-guided beating-heart surgery. In *IEEE Int. Conf. on Robotics and Automation*, pages 5825–5830, 2013.
- [9] A.H. Zahraee, J.K. Paik, J. Szewczyk, and G. Morel. Toward the development of a hand-held surgical robot for laparoscopy. *IEEE/ASME Trans. on Mechatronics*, 15(6):853–861, 2010.
- [10] S.G. Yuen, D.T. Kettler, P.M. Novotny, R.D. Plowes, and R.D. Howe. Robotic motion compensation for beating heart intracardiac surgery. *The Int. Journal of Robotics Research*, 28(10):1355–1372, 2009.
- [11] A.P.L. Bó P., Poignet, and C. Geny. Pathological tremor and voluntary motion modeling and online estimation for active compensation. *IEEE Trans. on Neural Systems and Rehabilitation Engineering*, 19(2):177–185, 2011.
- [12] T.M. Kowalewski, J. Rosen, L.C. Chang, M.N. Sinanan, and B. Hannaford. Optimization of a vector quantization codebook for objective evaluation of surgical skill. In *Medicine Meets Virtual Reality 12: Building a Better You: the Next Tools for Medical Education, Diagnosis, and Care*, pages 174–179. IOS Press, 2004.
- [13] R. Ginhoux, J.A. Gangloff, M.F. de Mathelin, L. Soler, J. Leroy, and J. Marescaux. Model predictive control for tracking of repetitive organ motions during teleoperated laparoscopic interventions. In *European Control Conference*, pages 2481–2486, 2003.
- [14] E.E. Tuna, T.J. Franke, Ö. Bebek, A. Shiose, K. Fukamachi, and M.C. Çavuşoğlu. Heart motion prediction based on adaptive estimation algorithms for robotic-assisted beating heart surgery. *IEEE Trans. on Robotics*, 29(1):261–276, 2013.

- [15] S.B. Kesner and R.D. Howe. Motion compensated catheter ablation of the beating heart using image guidance and force control. In *Int. Symposium on Experimental Robotics*, pages 579–590, 2012.
- [16] S.B. Kesner and R.D. Howe. Discriminating tissue stiffness with a haptic catheter: Feeling the inside of the beating heart. In *IEEE World Haptics Conf.*, pages 13–18, 2011.
- [17] S.B. Kesner, S.G. Yuen, and R.D. Howe. Ultrasound servoing of catheters for beating heart valve repair. In N. Navab and P. Jannin, editors, *Information Processing in Computer-Assisted Interventions*, volume 6135 of *Lecture Notes in Computer Science*, pages 168–178. Springer Berlin Heidelberg, 2010.
- [18] P.M. Loschak, L.J. Brattain, and R.D. Howe. Automated pointing of cardiac imaging catheters. In *IEEE Int. Conf. on Robotics and Automation*, pages 5794–5799, 2013.
- [19] S.G. Yuen, D.P. Perrin, N.V. Vasilyev, P.J. del Nido, and R.D. Howe. Force tracking with feed-forward motion estimation for beating heart surgery. *IEEE Trans. on Robotics*, 26(5):888–896, 2010.
- [20] B. Cagneau, N. Zemiti, D. Bellot, and G. Morel. Physiological motion compensation in robotized surgery using force feedback control. In *IEEE Int. Conf. on Robotics and Automation*, pages 1881–1886, 2007.
- [21] M. Dominici, P. Poignet, and E. Dombre. Compensation of physiological motion using linear predictive force control. In *IEEE/RSJ Int. Conf. on Intelligent Robots and Systems*, pages 1173–1178, 2008.
- [22] M. Dominici and R. Cortesao. Model predictive control architectures with force feedback for robotic-assisted beating heart surgery. In *IEEE Int. Conf. on Robotics and Automation*, pages 2276–2282, 2014.
- [23] Ö. Bebek and M.C. Çavuşoğlu. Whisker-like position sensor for measuring physiological motion. *IEEE/ASME Trans. on Mechatronics*, 13(5):538–547, 2008.

- [24] R. Ginhoux, J. Gangloff, M. de Mathelin, L. Soler, M.M. A. Sanchez, and J. Marescaux. Active filtering of physiological motion in robotized surgery using predictive control. *IEEE Trans. on Robotics*, 21(1):67–79, 2005.
- [25] Y. Nakamura, K. Kishi, and H. Kawakami. Heartbeat synchronization for robotic cardiac surgery. In *IEEE Int. Conf. on Robotics and Automation*, volume 2, pages 2014–2019, 2001.
- [26] A. Krupa, J. Gangloff, M. de Mathelin, C. Doignon, G. Morel, L. Soler, J. Leroy, and J. Marescaux. Autonomous retrieval and positioning of surgical instruments in robotized laparoscopic surgery using visual servoing and laser pointers. In *IEEE Int. Conf. on Robotics and Automation*, volume 4, pages 3769–3774, 2002.
- [27] E. Bogatyrenko, U.D. Hanebeck, and G. Szabo. Heart surface motion estimation framework for robotic surgery employing meshless methods. In *IEEE/RSJ Int. Conf. on Intelligent Robots and Systems*, pages 67–74, 2009.
- [28] D. Stoyanov and G.-Z. Yang. Stabilization of image motion for robotic assisted beating heart surgery. In Ni. Ayache, S. Ourselin, and A. Maeder, editors, *Medical Image Computing and Computer-Assisted Intervention*, volume 4791 of *Lecture Notes in Computer Science*, pages 417–424. Springer Berlin Heidelberg, 2007.
- [29] S. Chandra, I.S. Salgo, L. Sugeng, L. Weinert, W. Tsang, M. Takeuchi, K.T. Spencer, A. O’Connor, M. Cardinale, S. Settlemier, V. Mor-Avi, and R.M. Lang. Characterization of degenerative mitral valve disease using morphologic analysis of real-time three-dimensional echocardiographic images. *Circulation: Cardiovascular Imaging*, 4(1):24–32, 2011.
- [30] S.G. Yuen, P.M. Novotny, and R.D. Howe. Quasiperiodic predictive filtering for robot-assisted beating heart surgery. In *IEEE Int. Conf. on Robotics and Automation*, pages 3875–3880, 2008.
- [31] S. Yuen, S. Kesner, N. Vasilyev, P. Del Nido, and R. Howe. 3D ultrasound-guided motion compensation system for beating heart mitral valve repair. In *Medical Image*

- Computing and Computer-Assisted Intervention*, volume 5241 of *Lecture Notes in Computer Science*, pages 711–719. Springer Berlin / Heidelberg, 2008.
- [32] P.M. Novotny, J.A. Stoll, P.E. Dupont, and R.D. Howe. Real-time visual servoing of a robot using three-dimensional ultrasound. In *IEEE Int. Conf. on Robotics and Automation*, pages 2655–2660, 2007.
- [33] L.J. Brattain, P.M. Loschak, C.M. Tschabrunn, E. Anter, and R.D. Howe. Robotic steering of cardiac ultrasound imaging catheters. In *Proceedings of the 6th Hamlyn Symposium on Medical Robotics*, 2013.
- [34] M. Joinie-Maurin, B. Bayle, and J. Gangloff. Force feedback teleoperation with periodical disturbance compensation. In *IEEE Int. Conf. on Robotics and Automation*, pages 4828–4833, 2011.
- [35] A. Thakral, J. Wallace, D. Tomlin, N. Seth, and N.V. Thakor. Surgical motion adaptive robotic technology (s.m.a.r.t): Taking the motion out of physiological motion. In W.J. Niessen and M.A. Viergever, editors, *Medical Image Computing and Computer-Assisted Intervention*, volume 2208 of *Lecture Notes in Computer Science*, pages 317–325. Springer Berlin Heidelberg, 2001.
- [36] Ö. Bebek and M. C. Çavuşoğlu. Intelligent control algorithms for robotic-assisted beating heart surgery. *IEEE Trans. on Robotics*, 23(3):468–480, 2007.
- [37] T. Horiuchi, E.E. Tuna, K. Masamune, and M.C. Çavuşoğlu. Heart motion measurement with three dimensional sonomicrometry and acceleration sensing. In *IEEE/RSJ Int. Conf. on Intelligent Robots and Systems*, pages 4143–4149, 2012.
- [38] J. Rotella. Predictive tracking of quasi periodic signals for active relative motion cancellation in robotic assisted coronary artery bypass graft surgery. Master’s thesis, Case Western Reserve University, 2005.
- [39] T.J. Franke, Ö. Bebek, and M. C. Çavuşoğlu. Improved prediction of heart motion using an adaptive filter for robot assisted beating heart surgery. In *IEEE/RSJ Int. Conf. on Intelligent Robots and Systems*, pages 509–515, 2007.

- [40] E.E. Tuna, J.H. Karimov, T. Liu, Ö Bebek, K. Fukamachi, and M.C. Çavuşoğlu. Towards active tracking of beating heart motion in the presence of arrhythmia for robotic assisted beating heart surgery. *PLoS ONE*, 9(7):e102877, 2014.
- [41] M. Osranek, F. Bursi, P. W. O’Leary, C.J. Bruce, L.J. Sinak, K. Chandrasekaran, and J.B. Seward. Hand-carried ultrasound-guided pericardiocentesis and thoracentesis. *Journal of the American Society of Echocardiography*, 16(5):480–484, 2003.
- [42] *Miller-Keane Encyclopedia and Dictionary of Medicine, Nursing, and Allied Health, Seventh Edition*. Saunders, 2003.
- [43] <http://health.msn.com/popup.aspx?cp-documentid=100162864>.
- [44] L. Cuvillon, J. Gangloff, M. de Mathelin, and A. Forgione. Toward robotized beating heart tecabg: Assessment of the heart dynamics using high-speed vision. In J.S. Duncan and G. Gerig, editors, *Medical Image Computing and Computer-Assisted Intervention*, volume 3750 of *Lecture Notes in Computer Science*, pages 551–558. Springer Berlin Heidelberg, 2005.
- [45] W. Bachtá, Pierre Renaud, L. Cuvillon, E. Laroche, A. Forgione, and J. Gangloff. Motion prediction for computer-assisted beating heart surgery. *IEEE Trans. on Biomedical Engineering*, 56(11):2551–2563, 2009.
- [46] M. Bowthorpe, M. Tavakoli, H. Becher, and R. Howe. Smith predictor-based robot control for ultrasound-guided teleoperated beating-heart surgery. *IEEE Journal of Biomedical and Health Informatics*, 18(1):157–166, 2014.
- [47] M. Bowthorpe, V. Castonguay-Siu, and M. Tavakoli. Development of a robotic system to enable beating-heart surgery. *Journal of the Robotics Society of Japan, invited paper*, 32(4):339–346, 2014.
- [48] M. Dominici and R. Cortesao. Model predictive control architectures with force feedback for robotic-assisted beating heart surgery. In *IEEE Int. Conf. on Robotics and Automation (ICRA)*, pages 2276–2282, 2014.

- [49] J. Schwaab, M. Prall, C. Sarti, R. Kaderka, C. Bert, C. Kurz, K. Parodi, M. Günther, and J. Jenne. Ultrasound tracking for intra-fractional motion compensation in radiation therapy. *Physica Medica*, 30(5):578–582, 2014. Particle Radiosurgery Conference.
- [50] M. Bowthorpe, A. Álvarez García, and M. Tavakoli. GPC-based teleoperation for delay compensation and disturbance rejection in image-guided beating-heart surgery. In *IEEE Int. Conf. on Robotics and Automation*, pages 4875–4880, 2014.
- [51] B.D. Hoit. Pericarditis, 2006. URL [http://www.merckmanuals.com/professional/cardiovascular\\_disorders/pericarditis/pericarditis.html](http://www.merckmanuals.com/professional/cardiovascular_disorders/pericarditis/pericarditis.html).
- [52] O.J.M. Smith. Closer control of loops with dead time. *Chemical Engineering Progress*, 53:217–219, 1957.
- [53] A.L. Goldberger, L.A.N. Amaral, L. Glass, J.M. Hausdorff, P.Ch. Ivanov, R.G. Mark, J.E. Mietus, G.B. Moody, C.-K. Peng, and H. E. Stanley. PhysioBank, PhysioToolkit, and PhysioNet: Components of a new research resource for complex physiologic signals. *Circulation*, 101(23):e215–e220, 2000 (June 13).
- [54] M.C. Çavuşoğlu, D. Feygin, and F. Tendick. A critical study of the mechanical and electrical properties of the phantom haptic interface and improvements for high-performance control. *Presence: Teleoperators and Virtual Environments*, 11(6): 555–568, 2002.
- [55] V. Falk. Manual control and tracking - a human factor analysis relevant for beating heart surgery. *The Annals of Thoracic Surgery*, 74(2):624–628, 2002.
- [56] P. Novotny. Real-time processing of three dimensional ultrasound for intracardiac surgery. *Ph.D. dissertation, Harvard University*, 2007.
- [57] CivcoMedicalSolutions. Infinity™ needle guidance system. <http://www.civco.com>, 2011.

- [58] F. Casamassima, C. Cavedon, P. Francescon, J. Stancanello, M. Avanzo, S. Cora, and P. Scalchi. Use of motion tracking in stereotactic body radiotherapy: Evaluation of uncertainty in off-target dose distribution and optimization strategies. *Acta Oncologica*, 45(7):943–947, 2006.
- [59] H. Shirato, S. Shimizu, T. Kunieda, K. Kitamura, M. van Herk, K. Kagei, T. Nishioka, S. Hashimoto, K. Fujita, H. Aoyama, K. Tsuchiya, K. Kudo, and K. Miyasaka. Physical aspects of a real-time tumor-tracking system for gated radiotherapy. *Int. Journal of Radiation Oncology Biology Physics*, 48(4):1187–1195, 2000.
- [60] A. Bel, O. Petrascu, I. Van de Vondel, L. Coppens, N. Linthout, D. Verellen, and G. Storme. A computerized remote table control for fast on-line patient repositioning: Implementation and clinical feasibility. *Medical Physics*, 27(2):354–358, 2000.
- [61] P.J. Keall, V.R. Kini, S.S. Vedam, and R. Mohan. Motion adaptive X-ray therapy: a feasibility study. *Physics in Medicine and Biology*, 46(1):1–10, 2001.
- [62] T. Neicu, H. Shirato, Y. Seppenwoolde, and S.B. Jiang. Synchronized moving aperture radiation therapy (SMART): average tumour trajectory for lung patients. *Physics in Medicine and Biology*, 48(5):587–598, 2003.
- [63] M.J. Murphy. Tracking moving organs in real time. *Seminars in Radiation Oncology*, 14(1):91–100, 2004.
- [64] J.R. Adler, S.D. Chang, M.J. Murphy, J. Doty, P. Geis, and S.L. Hancock. The Cyberknife: A frameless robotic system for radiosurgery. *Stereotactic and Functional Neurosurgery*, 69:124–128, 1997.
- [65] D. Fu, R. Kahn, B. Wang, H. Wang, Z. Mu, J. Park, G. Kuduvalli, and C. Maurer. Xsight lung tracking system: A fiducial-less method for respiratory motion tracking. In H. Urschel, J. Kresl, J. Luketich, L. Papiiez, R. Timmerman, and R. Schulz, editors, *Treating Tumors that Move with Respiration*, pages 265–282. Springer Berlin Heidelberg, 2007.

- [66] M.F. Kruis, J.B. van de Kamer, A.C. Houweling, J. Sonke, J.S.A. Belderbos, and M. van Herk. PET motion compensation for radiation therapy using a CT-based mid-position motion model: Methodology and clinical evaluation. *Int. Journal of Radiation Oncology Biology Physics*, 87(2):394–400, 2013.
- [67] S. Xu, G. Fichtinger, R.H. Taylor, and K.R. Cleary. 3D motion tracking of pulmonary lesions using ct fluoroscopy images for robotically assisted lung biopsy. *Proc. SPIE*, 5367:394–402, 2004.
- [68] P.J. Parker and B.D.O. Anderson. Frequency tracking of nonsinusoidal periodic signals in noise. *Signal Processing*, 20(2):127–152, 1990.
- [69] J. Li, M. Tavakoli, V. Mendez, and Q. Huang. Passivity and absolute stability analyses of trilateral haptic collaborative systems. *Journal of Intelligent and Robotic Systems*, 78(1):3–20, 2015.
- [70] L. Santos and R. Cortesao. A dynamically consistent hierarchical control architecture for robotic-assisted tele-echography with motion and contact dynamics driven by a 3D time-of-flight camera and a force sensor. In *IEEE Int. Conf. on Robotics and Automation*, pages 2931–2937, 2015.
- [71] M.K. Rausch, W. Bothe, J.P.E. Kvitting, J.C. Swanson, D.C. Miller, and E. Kuhl. Mitral valve annuloplasty. *Annals of Biomedical Engineering*, 40(3):750–761, 2012.
- [72] G.E. Snedecor and W.G. Cochran. The two-tailed t-test. In *Statistical Methods*, pages 59–60. The Iowa State University Press Ames, 1967.
- [73] R. Rayman, S. Primak, R. Patel, M. Moallem, R. Morady, M. Tavakoli, V. Subotic, N. Galbraith, A. van Wynsberghe, and K. Croome. *Effects of Latency on Telesurgery: An Experimental Study*, volume 3750 of *Medical Image Computing and Computer-Assisted Intervention*, pages 57–64. Springer Berlin/Heidelberg, 2005.
- [74] D.W. Clarke, C. Mohtadi, and P.S. Tuffs. Generalized predictive control part i. the basic algorithm. *Automatica*, 23(2):137–148, 1987.

- [75] E.F. Camacho and C. Bordons. *Model Predictive Control*. Springer, 1999.
- [76] R. Oboe, F. Marcassa, and G. Maiocchi. Hard disk drive with voltage-driven voice coil motor and model-based control. *IEEE Trans. on Magnetics*, 41(2):784–790, 2005.
- [77] Opencv library: <http://opencv.org>.